Nottingham University, 2012

Andrew Britton

Charge Transfer Dynamics of Adsorbate Molecules on Metal and Semiconductor Surfaces Relating to Fundamental Processes in Dye-Sensitized Solar Cells

Acknowledgements

I would like to thank my supervisor, James O'Shea, and my colleagues, Matt Weston and Karsten Handrup, as well as everyone in the Nanoscience Group at the University of Nottingham. I would also like to thank all the technical support at MAXlab, particulary the I511 beamline manager, Annette Pietzsch, and the I311 beamline manager, Karina Schulte. I am grateful for financial support by the UK Engineering and Physical Sciences Research Council (EPSRC), and the European Community Research Infrastructure Action.

Most importantly, I would like to thank my wife, Simone, whose love, patience and support were essential to my success. I would also like to thank all my family, especially my late father, John, whose enthusiasm for science inspired my own scientific journey.

List of Related Publications

1. *Charge Transfer between the Au(111) Surface and Adsorbed C_{60}: Resonant Photoemission and new Core-hole Decay Channels*, A. J. Britton, A. Rienzo, James N. O'Shea and K. Schulte, Journal of Chemical Physics, **133**, page 094705 (2010)

2. *Charge Transfer Interactions of a Ru(II) Dye Complex and Related Ligand Molecules Adsorbed on Au(111)*, A. J. Britton, M. Weston, J. B. Taylor, A. Rienzo, L. C. Mayor and J. N. O'Shea, Journal of Chemical Physics, **135**, page 164702 (2011)

3. *Charge Transfer from an Aromatic Adsorbate to a Semiconductor TiO2 Surface Probed on the Femtosecond Time Scale with Resonant Inelastic X-Ray Scattering*, A. J. Britton, M. Weston, J. N. O'Shea, Physical Review Letters, **109**, page 017401 (2012)

Contents

Chapter 1

Introduction to Dye-Sensitized Solar Cells

The search for a clean renewable energy supply which is both cheap and reliable is one of the world's most pressing problems. With demand for energy increasing in the developing world as it becomes more prosperous, and as the supply of easily accessible oil and gas is likely to run out within the next hundred years, the cost of energy will rise and the search for alternatives becomes more intense. Combined also with the need to keep carbon dioxide emissions from rising at current rates in order to mitigate at least some of the worst scenarios of climate change, the need for cleaner energy sources has never been greater.

There are several alternatives to the use of fossil fuels, such as: nuclear energy, hydroelectricity, geothermal, tidal power, wave energy, wind turbines, solar thermal and solar photovoltaic energy. Unfortunately, most of these alternatives have severe limitations either in lack of usable locations (such as hydroelectricity, geothermal or tidal), in its being highly controversial (such as nuclear energy) or in its being much more costly than fossil fuel power stations, often needing significant public subsidies to make them attractive for outside investment.

Photovoltaic solar cells are one of the most feasible ways of dealing with this problem. The Earth receives 174 PW (1.74×10^{17}W) of radiation from the Sun. This is several thousand times the amount of power currently required by our civilization (at about 15 TW).[1] Although the vast majority of the electricity we use does come indirectly from the sun (through fossil fuels and wind power), very little is currently produced directly from photovoltaic devices (only 0.06 percent in 2010). This is due

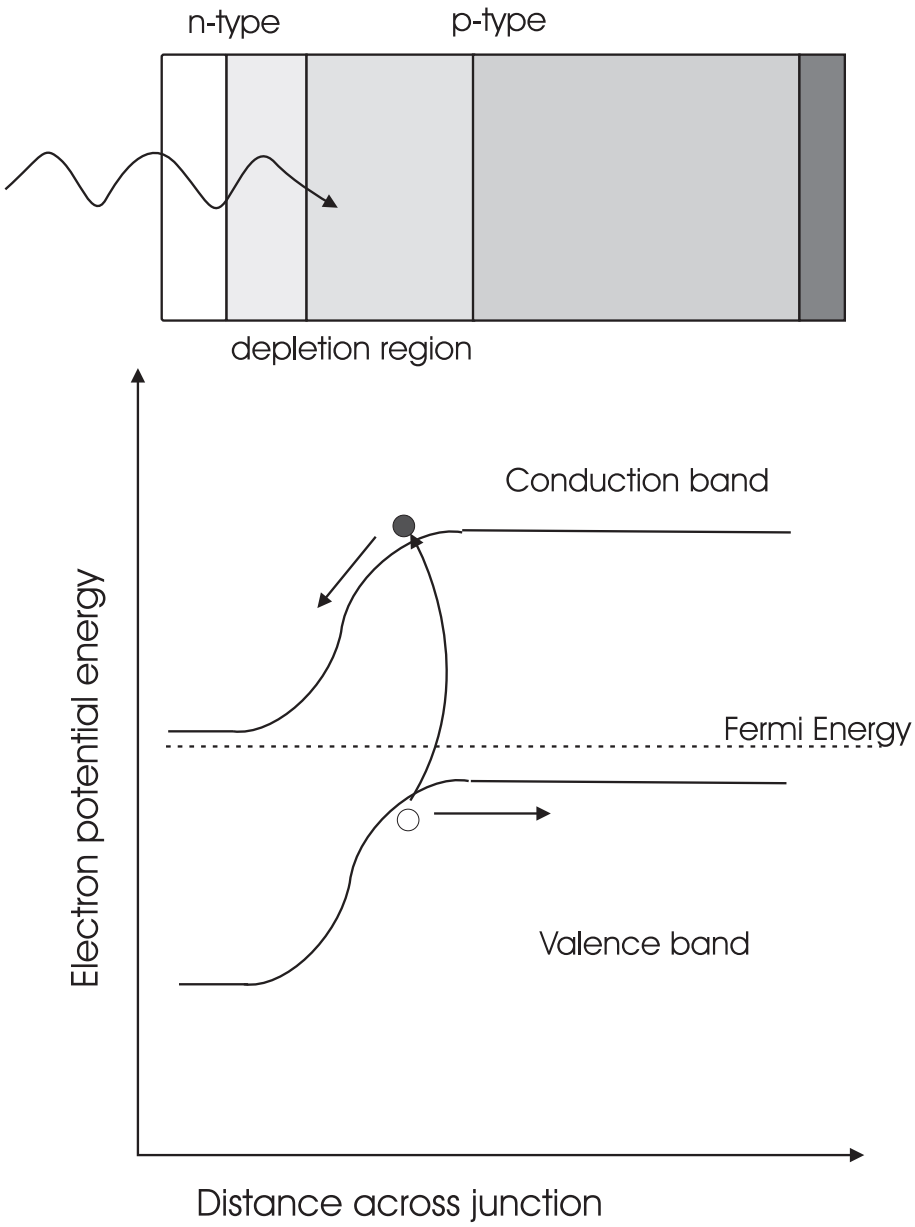

FIGURE 1.1: Diagram of the physical structure and corresponding band diagram of a conventional homojunction solar cell.

to both the low efficiency and the high cost of production for conventional solid state photovoltaic solar cells; crystalline silicon solar cells require a relatively thick layer of doped silicon in order to have reasonable photon capture rates, and crystalline silicon processing is expensive.[1] This makes it economically unfeasible to supply the world's

current energy demands. Thin film solar cells offer a solution to this by decreasing, or in some cases eliminating, the need for large amounts of crystalline silicon processing which has a high cost.

Amorphous silicon solar cells are used in many low power applications which need a low cost of production, such as calculators. Deposition of the silicon can be done cheaply at low temperatures using plasma enhanced chemical vapour deposition instead of growing silicon wafers as crystalline silicon solar cells.[1] The small width of the silicon layer leads to very low photon-capture rates. This can be improved by stacking them in layers, achieving efficiencies of 13.7 percent compared with 24.7 percent for crystalline silicon wafers[2] (all efficiencies for AM (Air Mass) 1.5 (1000W/m^2), which is the universal standard for terrestrial solar panels and represents the yearly average radiation at sea level for temperate latitudes). The cheaper production costs offset the lower efficiencies. There are various combinations of crystalline and amorphous silicon solar cells. Nevertheless, eliminating the need for silicon altogether and using other semiconductors for solar cells, such as cadmium telluride or copper indium gallium selenide has become common. Unfortunately, these materials are considered toxic and have a very low natural abundance.[1, 2] Very high efficiency solar cells that use multiple heterojunctions and quantum wells have also been produced. These are very expensive to manufacture, though, and are used primarily for applications where a high power production to weight ratio is important, such as satellites.[3] Other semiconductors, such as titanium dioxide, would be effective if it were not for the problem that its band gap is too large for visible light (single titanium dioxide crystals with no defects are transparent). This can be overcome be using a sensitizer dye on the surface. This leads to dye-sensitized solar cells (DSSCs) which provide an alternative approach to the conventional solar cell which could be more economically feasible and shall, thus, be focused upon more closely here.

All photovoltaic devices are based on the concept of charge separation at the interface between two materials with different methods of charge conduction caused by incident visible light. In conventional solar cells, as seen in figure 1.1, the charge separation occurs due to the interface between two differently doped regions of a semiconductor (in most cases, silicon). One of the regions (n-type region) is doped

with atoms called donors which, at room temperature, supply electrons to the conduction band of the silicon. The other region (p-type region) is doped with acceptor atoms which, at room temperature, supply holes to the valence band of the silicon. Bringing these two materials together leads to the diffusion of the carriers across the interface. The diffused electrons combine with the acceptor dopants and the diffused holes combine with the donor atoms. This leads to a buildup of electric charge on each side which creates an electric field across the p-n junction. An incoming photon, when absorbed, promotes an electron into the conduction band and creates a hole in the valence band. If this electron-hole pair is created at the junction, the electric field across the junction drives the electron to the n-type region and the hole to the p-type region. This creates an electric current if the two regions are connected in a circuit.

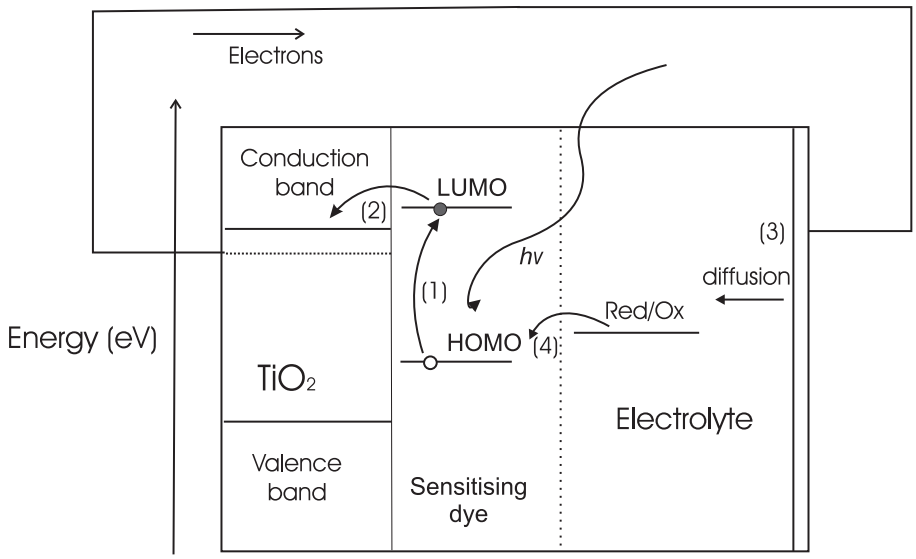

FIGURE 1.2: Operating principles of a dye sensitized solar cell (DSSC). An incoming photon excites an electron from the highest occupied molecular orbital (HOMO) to the lowest unoccupied molecular orbital (LUMO) of the dye molecule(1). The excited electron then tunnels into the conduction band of the TiO_2 substrate (2). The cathode of the DSSC supplies electrons to the electrolyte (usually iodide/iodine) and the electrolyte diffuses to the dye(3). The electrolyte resupplies the dye molecule LUMO via a redox reaction (4).

The concept behind dye-sensitized solar cells is a departure from the classic solid-

state junction device. In a dye-sensitized solar cell, a monolayer of a dye molecule is adsorbed onto the surface of nanoparticles of a wide band-gap semiconductor, the material of choice being usually titanium dioxide (although zinc oxide is a common alternative). These nanoparticles are all connected in a porous network (this increases the area available onto which the molecule can be adsorbed).[4, 5] The nanoparticles are immersed in an electrolyte (usually iodide/triodide) held in place between the transparent cathode and TiO_2 anode. The dye molecule, the most common one, due to it's high efficiency, being a ruthenium (II) dye complex called N3 (cis- bis(isothiocyanato)bis(2,2'-bipyridyl-4 ,4'-dicarboxylato)-ruthenium(II), absorbs incoming photons and electrons are promoted from the highest occupied molecular orbitals (HOMO) to the lowest unoccupied molecular orbitals (LUMO) of the molecule.[4, 5] The electron in the LUMO tunnels into the TiO_2 substrate and, consequently, moves towards the anode, creating an electric current if the anode and cathode are connected in a circuit. The hole in the HOMO of the dye molecule is filled via a reduction reaction with the electrolyte which is replaced via the cathode. A diagram of the operating principles of a dye sensitized solar cell is shown in Figure 1.2. Efficiencies as high as 11 percent have been achieved using a ruthenium based dye on titanium dioxide nanoparticles for AM 1.5 (sunlight at 1000W/m^2).[2, 4] The binding and charge transfer properties of N3, and its constituent ligands, on TiO_2 have been been studied by our research group using synchrotron-based radiation.[6, 7]

Studying the charge transfer properties of bi-isonicotinic acid on TiO_2 is important because previous studies, which used photoemission spectroscopy, have shown that N3 bonds to a TiO_2 surface via deprotonation of the carboxylic acid groups in the bi-isonicotinic acid ligands forming a 2-M bidentate bond, where the molecular oxygen atoms in the carboxylic group bind to adjacent titanium atoms in the surface.[6, 8] This chemical coupling allows for the charge transfer to occur between the N3 molecule and the TiO_2 surface in the nanoparticles. A previous experiment by Schnadt *et al* [9] used a combination of resonant photoemission spectroscopy (RPES) and x-ray absorption spectroscopy (XAS), both using synchrotron radiation, of bi-isonicotinic acid on rutile TiO_2 to find a charge transfer time of under 3 femtoseconds. In Chapter 7 of this thesis, I show the results of another study of the charge transfer properties of

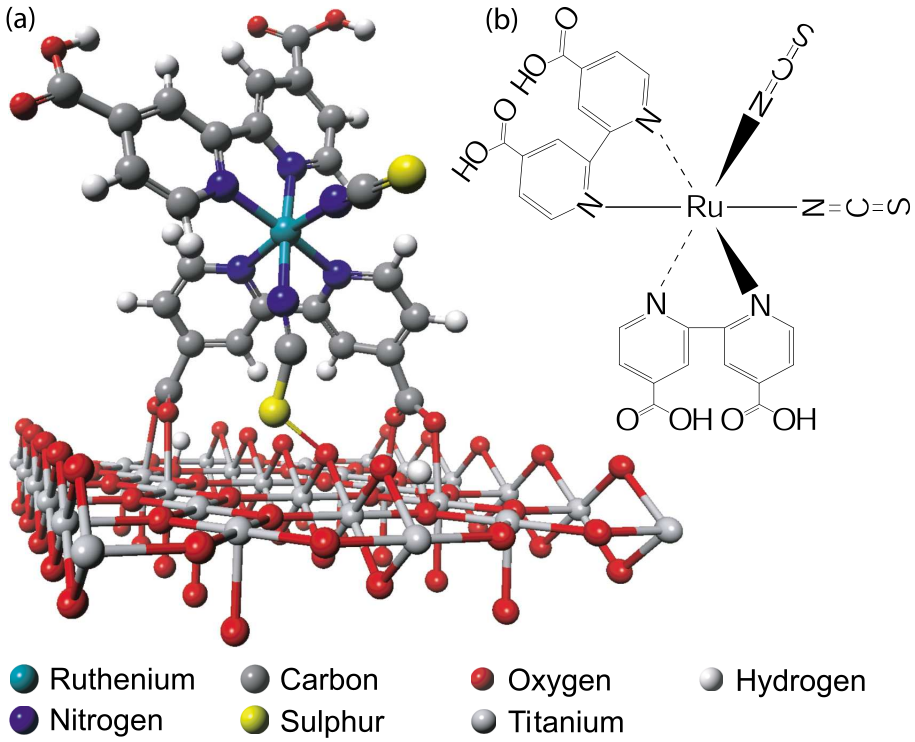

FIGURE 1.3: (a) shows a diagram, created using DFT calculations, of an N3 dye molecule bonded to a TiO_2 surface. The molecules are bonded via the bi-isonicotinic acid ligands. (b) chemical structure of N3. Taken with permission from reference [6]

bi-isonicotinic acid on TiO_2. However, we used a different technique called resonant inelastic x-ray scattering to study the molecule on the surface, which probes the x-rays emitted from the surface, instead of observing the electrons emitted in the photoemission case when the sample is irradiated x-rays. We adapted a technique previously only used in resonant photoemission spectroscopy, called the core-hole clock technique, to determine the charge transfer from the molecule to the surface. Further discussion of the Methods used can be found in the methods section and discussion of the results of the experiment is in Chapter 7.

1.0.1 Introduction to Solid State Dye Sensitized Solar Cells

There are two main problems with using a liquid electrolyte in dye-sensitized solar cells. The first is that the electrolyte absorbs some of the photons, reducing the

efficiency. The second is that the stability of the device is also affected by the liquid electrolyte as the liquid can evaporate if the device is improperly sealed.[10, 11] Thermal stability of the electrolyte is also a possible issue: at very cold or very hot temperatures, problems can occur with expansion of the liquid.[10, 11] These problems cause this type of solar cell to be quite difficult to manufacture and maintain due to the liquid electrolyte needing to be properly sealed. Finding another way to supply electrons to the dye molecule is important in creating a better solar cell.

The solid state dye-sensitized solar cell provides another way. There are a number of different types of solid state DSSCs, but they all rely on a similar principle of using a solid or semi-solid hole conductor to supply electrons from the conductor to the HOMO of the sensitizer dye with the dye sandwiched between the TiO_2 and the hole conductor.[10] Some DSSCs utilize p-type semiconductors as hole conductors.[12] These semiconductors are doped with acceptor atoms which supply holes to the valence band of the semiconductor.[12, 13] These conduct holes away from the dye. Many normal inorganic p-type semiconductors can not be used because the high temperature of the deposition can damage the dye, reducing it's effectiveness.[14] Copper compounds, such as copper iodide, are commonly used but the resulting solid state DSSCs have a very low efficiency compared to standard DSSCs with a best efficiency of 2.4 percent.[15] This is due in part to their low hole conductivity. Organic p-type semiconductors have achieved better results with a maximum of 3.2 percent using an organic hole transport molecule (HTM), OMeTAD (2,20,7,70-tetrakis (N,N-di-p-methoxyphenyl-amine)9,90-spirobifluorene), with the dopants 4-tert-butylpyridine (tBP) and $Li(CF_3SO_2)_2)N$.[16] The conversion efficiencies of DSSCs using organic p-type semiconductors are poor. This is because of many reasons, such as: the low intrinsic conductivities of the hole conducting molecules (HTMs),[10] the high level of charge recombination from the TiO_2 to the HTMs[10] and, most importantly, the poor electronic contact between the dye molecules and the HTMs caused by the lack of penetration of the large HTMs into the pores between the TiO_2 nanoparticles.[17]

Room temperature ionic liquids (RTILs) have good thermal and chemical stability.[18] They also have the advantages of having a negligible vapor pressure, nonflammability and high ionic conductivity.[18] When used in dye sensitized solar cells, they

can work as both the solvent and a source of iodide which can resupply electrons. RTILs solve some of the stability issues that occur with iodide electrolyte found in DSSCs.[10] The viscosity of the RTILs are a significant limiting factor as they slow the movement of ions in the electrolyte. Low viscosity RTILS, such as EMISeCN (1-ethyl-3-methylimidazolium selenocyanate), have achieved efficiencies of 7.5 percent which are nearly as good as standard DSSCs.[19] Yet, they still have some of the problems found in standard DSSCs, such as a high cost of manufacturing due to the liquid electrolyte.[10]

Polymers have been used as electrolytes because they can conduct ions easily along them and also because they can solidify in a gel allowing for a better contact between the solid electrolytes and the TiO_2 nanoparticles.[10] During the manufacture of polymer solid state DSSCs, the gel electrolyte, which contains the polymer electrolytes, gelating agents and an iodide solvent, is injected in liquid form into the gap between the glass front and the nanoparticles.[20] The gel is then heated until it solidifies. The polymer electrolyte can get into the pores in the TiO_2 nanoparticles and increase the amount of contact between the dyes and the electrolyte.[20] Dye sensitized cells which use polymer gels are more properly considered as quasi-solid state DSSCs.[10] The polymers in the liquid undergo polymerization to form networks in which iodide ions can move along. Efficiencies as high as 8.1 percent have been achieved with DSSCs which use polymer gels.[21]

A different approach to the dye-sensitized cell has the electrons resupplied to the dye by an ultrathin (< 50nm) layer of gold instead of an electrolyte solution. The dye is adsorbed onto the gold layer which lies on the TiO_2 substrate.[22] As is shown in figure 1.4, the dye molecule absorbs incoming photons and electrons are promoted from the HOMO to the LUMO of the molecule. It is suggested that the promoted electrons travel ballistically across the gold layer and tunnel into the TiO_2 substrate and then through to the titanium metal anode. The lost electrons are then replaced from the gold layer which is connected to the cathode. This approach was put forward by McFarland and Tang in 2003.[22] Their cell used a fluorescein photoreceptor known as merbromin which, like all dye sensitizers, had the LUMO above the bandgap of the TiO_2, and this, consequently, should allow for charge transfer to the conduction

band. The cells had an extremely low efficiency (less than 1 percent), but the fact that it worked at all was surprising, as it means that a significant number of the electrons can ballistically travel through the gold layer which, given the amount of scattering that the gold atoms would cause, seems highly unlikely. This makes it an area for further investigation. There has been a suggestion that no tunneling actually occurs from the dye molecule to the titanium dioxide layer but instead electrons are excited in the gold layer and then transferred into the TiO_2 layer.[23]

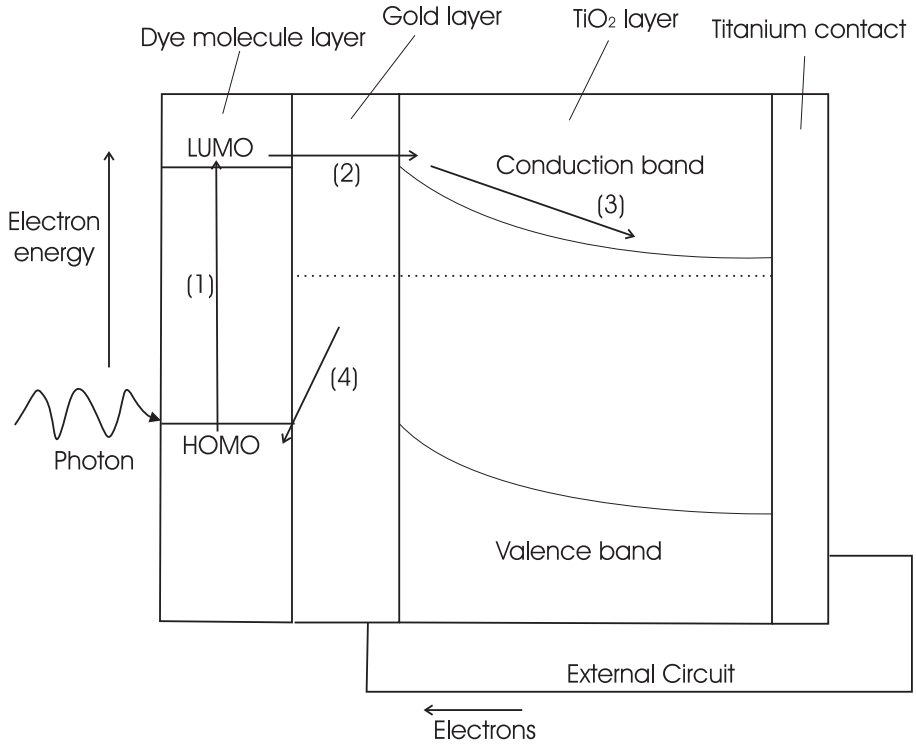

FIGURE 1.4: The structure of a McFarland and Tang solar cell and the processes they believe to be involved in the conversion process. Incoming photons cause electrons to be excited from the HOMO to the LUMO of the dye molecule (1). The electrons move ballistically across the gold layer and over the Schottky barrier into the TiO_2 substrate (2). The electrons move through the TiO_2 substrate and through the external circuit (3). The electrons are resupplied to the LUMO of the dye molecule from the gold layer (4).

The supply of electrons to the dye molecule is one of the key limiting steps for dye-sensitized solar cells. Studying the physical processes behind the transfer of charge between certain molecules and surfaces allows for a better understanding of solid

state DSSCs such as that produced by McFarland and Tang. Previous experiments by Ben Taylor *et al*, a former member of our research group, looked at bi-isonicotinic acid adsorbed onto a gold surface with synchroton radiation.[24] A technique called resonant photoemission spectroscopy (RPES) was used in which the valence band photoemission spectra are measured for a range of photon energies covering the N 1s absorption edge. This produces 2D datasets for the monolayer and multilayer of bi-isonicotinic acid on gold. A strange new feature was observed for the monolayer spectra: a diagonal Auger-like feature, which was then described tentatively as *superspectator* decay. This *superspectator* decay phenomenon was considered to be a consequence of an Auger decay after ultra-fast charge transfer, in the core-excited state, from the gold to the molecule.

The phenomenon of *superspectator* decay or, as we later called it, charge transfer Auger is investigated in this thesis in chapters three and four. In Chapter four, we investigate charge transfer of buckminsterfullerene (C_{60}) adsorbed onto gold. Even though there has been extensive use of C_{60} in conjunction with porphyrins and other molecules in the operation of solar cells,[25, 26] it does not seem to be an obvious choice to study in regard to understanding N3 dye sensitized solar cells. Nonetheless, the *superspectator* features were very distinctive. They provided a much clearer picture of the electronic structure and allowed us to determine the exact nature of the decay channel. This provides us with vital insight into the previous research of bi-isonicotinic acid on gold.

Chapter 5 describes an investigation of the charge transfer processes of the N3 dye molecule adsorbed onto gold, comparing it with both the previous experiment of bi-isonicotinic acid adsorbed onto gold by Taylor *et al*[24] and with our studies of isonicotinic acid adsorbed onto gold. This experiment was studied because the setup provides insight into the dye sensitized solid-state solar cell produced by McFarland and Tang. [22] This is followed by our investigation, in Chapter 6, of nicotinic and picolinic acid, both similar to isonicotinic acid, adsorbed onto gold.

In summary, Chapter 2 deals with the charge transfer theory, both intermolecular and surface-molecule charge transfer. Chapter 3 explains the methods and apparatus used in our experiments. Chapter 4 shows the results and analysis of our investi-

gation on the charge transfer of C_{60} adsorbed onto gold. In Chapter 5, there is a similar study of the dye molecule, N3, and its constituent ligands adsorbed onto gold which is followed in Chapter 6 with a study of nicotinic and picolinic acid on gold. Chapter 7 describes and provides experimental proof for a novel technique for studying charge transfer using an adaptation of the 'core-hole clock' technique to RIXS. Finally, Chapter 8 provides a summary and conclusion for the thesis.

Chapter 2

Charge Transfer Theory

To understand the charge transfer process between dye molecules and surfaces in dye sensitized solar cells (DSSCs), it is important to explore the theory of charge transfer between adsorbates and surfaces. Before we discuss the charge transfer between adsorbates and surfaces, we need to look at the case of charge transfer between two molecules in the gas phase and under no outside forces. Specifically, what is examined is the exchange of electrons between two discrete molecular states. To help understand the concepts of electron transfer at surfaces, it is useful to investigate the two-state situation and then to expand it to include the extra electronic states that need to be taken into account because of the surface.

Electron transfer between two molecular states can be approximated as electron tunneling between two identical square-well potentials which correspond to the molecular states. Time-independent solutions for this problem are simple. The two individual eigenstates of each well are mixed together to construct two new eigenstates for the coupled system as a whole.[27] This situation is shown in figure 2.1. The difference in energy between the two new eigenstates is twice the electronic coupling, which is the amount of overlap in the wave functions within the well (this is called the tunneling matrix element, V).[28] This situation can be described by an eigenfunction of the associated Hamiltonian.

The time-independent solution is, of course, not realistic. It requires that the molecules be stationary and that there be no change in the system. In reality, the thermal motions of a system mean that the intermolecular distances change all the

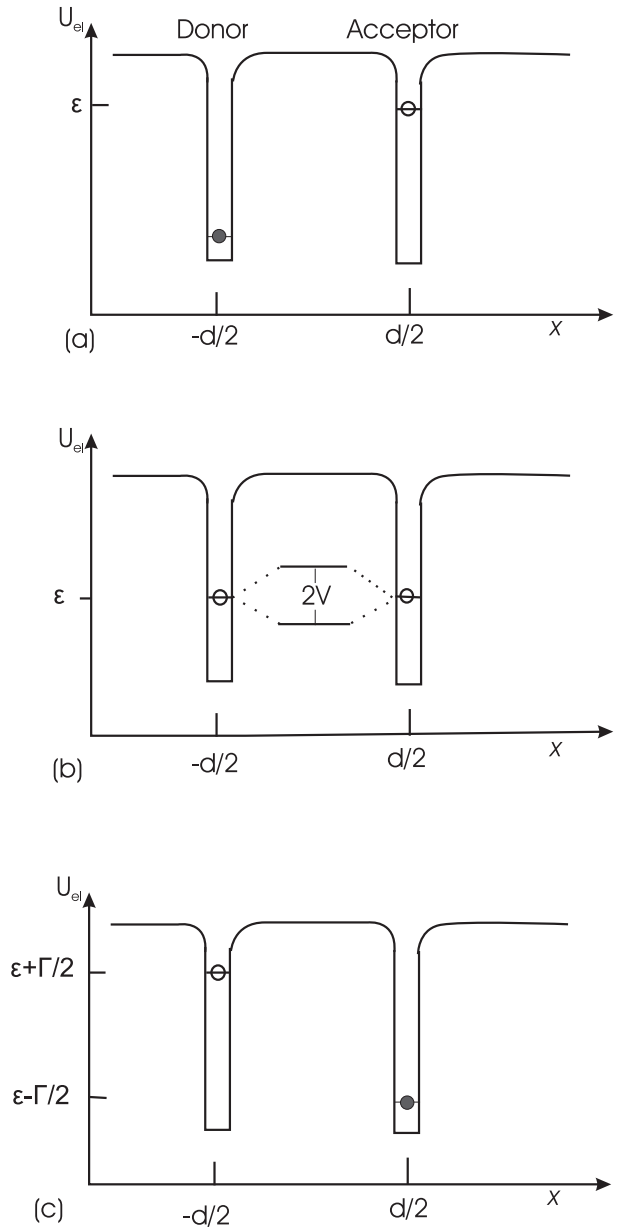

FIGURE 2.1: Square-well model representing the mechanics of charge transfer between two molecules through the mixing of discrete electronic states between the molecules. The displacement of the energy levels from resonance is caused by the motions of the nuclei in the molecules. ϵ is the site energy of the acceptor and Γ is the difference between the two energy levels. In the top diagram, (a), the electron is localized on the donor molecule. In diagram (b) the two energy levels are at resonance, producing a mixed electronic state and allowing charge distribution between the two molecules. In the bottom diagram, (c), the levels have become out of resonance and the electron has become localized on the acceptor.

time and, hence, they change the forces between the molecules which causes changes in the energy levels within the wells.[27] This means there is only a short period of time when the states are in resonance and when tunneling can occur. To consider the actual rate of charge transfer, we have to use the time-dependent Schrödinger equation[29]

$$\imath\hbar\frac{\partial\Psi}{\partial t} = \hat{H}\Psi. \tag{2.1}$$

For a single non-relativistic particle moving in an electric field in one dimension, the equation above can be expanded as:

$$\imath\hbar\frac{\partial\Psi(x,t)}{\partial t} = -\frac{\hbar^2}{2m}\frac{\partial^2\Psi(x,t)}{\partial x^2} + V\Psi(x,t). \tag{2.2}$$

The solution for this is the wavefunction

$$\Psi(x,t) = \sum_{n=0}^{\infty} a_n\Psi(x)e^{-\frac{iE_nt}{\hbar}} \tag{2.3}$$

where a_n is the coefficient which describes the probability of finding the system in state n with an energy of E_n. By taking the boundary conditions at t=0, when the electron is fully localized in the donor well, it is possible to obtain a time dependent probability distribution for the two square well problem when the energy levels are the same in each well, as seen in figure 2.1b.

$$\Psi(x,t) = e^{-\imath\epsilon t/\hbar}(\cos(\frac{Vt}{\hbar})\phi(x+d/2) - \imath\sin(\frac{Vt}{\hbar})\phi(x-d/2)), \tag{2.4}$$

where ϵ is the site energy of the acceptor and d is the distance between the two quantum wells.[27, 30] The tunneling matrix element, V, is a function of d. Only a single state is considered for each well, defined as $\phi(x,t)$. The electron distribution oscillates between the two wells with a period of $\hbar/V$. This would go on until the motions of the atomic nuclei in the molecules drove the electronic levels out of resonance and the electronic coupling is decreased. In the case of a change in the energy levels, the equation can be given as:[27, 30]

$$\Psi(x,t) = e^{-\imath\epsilon t/\hbar}(\cos(\frac{\Delta t}{2\hbar} + \frac{\imath\Gamma}{\Delta}\sin(\frac{\Delta t}{2\hbar})\phi(x+d/2) - \frac{2\imath\Gamma}{\Delta}\sin(\frac{\Delta t}{2\hbar})\phi(x-d/2)) \quad (2.5)$$

where Γ is the difference in energy between the two energy levels and

$$\Delta^2 = (\Gamma^2 + 4V^2)^{1/2}. \quad (2.6)$$

What this shows is that the coupling between the molecules is decreased by a mismatch in the energy levels. As time increases, the electron is increasingly more likely to be found at the lowest energy site.[27] When the energy difference caused by nuclear fluctuations is much greater than the electronic coupling, the electron becomes localized at the lower energy site. The acceptor site ends up being lower in energy due to the movement of the electron. The electron distribution at the initial site is negligible and the electron can be said to have transferred from the donor site to the acceptor site.

The important point to remember is that the energy gap that occurs due to thermal motion of the nuclei in the molecules leads to the decoupling of the molecules and the re-localization of the electron onto the acceptor molecule. The rate of charge transfer is dependent on the competing processes of electron tunneling and thermal nuclear motion. The electron tunneling is dependent on the amount of coupling between the two molecules which in turn is dependent on the size of the potential barrier and the amount of separation between the molecules. In the case of weak coupling, the motions of the nuclei disrupt the resonance between the two molecules before the electron has had time to tunnel between them. The electron very rarely transfers to the acceptor molecule. The electron transfer-time is determined by the probability of the system maintaining resonance between the molecules. This is called the nonadiabatic limit for charge transfer.[27, 31] In the other case, in which the electronic coupling is strong, the electron tunneling usually occurs before the nuclear motions destroy the resonance. The delocalized charge actually causes the surrounding medium to polarize with the resultant nuclear motion creating an energy gap between the two states that disrupts the resonance.[31] The nuclear relaxation is the upper limit for electron transfer and this is called the adiabatic limit.[31]

The potential energy diagram for the charge transfer between two molecules is shown in figure 2.2 with the potential energy measured for a variety of nuclear reaction co-ordinates. The real potential energy surface for the atoms is very complex, but figure 2.2 is a reasonable approximation to a single pair. The position at A in the diagram represents the nuclear configuration where the system is at the lowest potential energy, with the electron on the donor. The position at C is the configuration at the lowest energy when the electron is on the acceptor. In between, lies position B which is the situation when the two molecules' electronic levels are in resonance, allowing for a mixed electronic state and for the redistribution of charge.

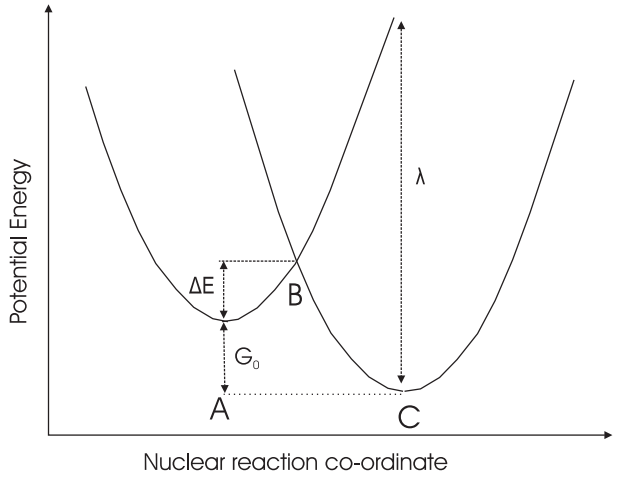

FIGURE 2.2: Potential energy diagram for movement along the electron transfer reaction co-ordinate. Positions A and C are the lowest potential energy points for the electron being on the acceptor and donor, respectively. At the intersection of the two potential energy parabolas, lies position B where the electronic states are in resonance and where electron transfer can take place. λ is the reorganization energy required to transfer the electron, G_0 is the difference in energy between the acceptor and donor sites, and ΔE is the energy of charge transfer site at B.

An important contribution to the field of electron transfer between two molecules is the theory set forth by Rudolph A. Marcus in 1956.[32] It was derived in response to the failure of Eyring's transition state theory to predict electron transfer in the situation where there is no structural change in the molecules. Marcus's theory specifically deals with the one electron redox reaction;[32]

$D + A \rightleftharpoons D - A \rightleftharpoons D^+ - A^- \rightarrow D^+ + A^-$.

The classic example used by Marcus for this was iron in solution[32, 33, 31] but electron transfer reactions involving two molecules are also very common in biological systems.[34]

$Fe_a^{3+} + Fe_b^{2+} \rightarrow Fe_a^{2+} + Fe_b^{3+}$.

So, in figure 2.2, the energy difference between point A and point B represents the activation energy in the classical potential energy picture put forward by transition-state theory used for elementary chemical reactions. This difference in energy represents the amount of energy required to arrange the atoms to bring the acceptor and donor into resonance. The probability for attaining this condition can be found using Boltzmann statistics.[35] The movement into position C is influenced by the explicit exothermicity of the charge transfer.[35] If the electron being on the acceptor has a lower potential energy than when it is on the donor, then charge transfer to the acceptor is much more likely. This difference in potential energy is mainly due to the difference in the relative energy positions of the highest unoccupied molecular orbital (HOMO) of the donor and the lowest unoccupied molecular orbital (LUMO) of the acceptor.[27] The Arrhenius equation gives us the expression for the charge transfer rate, k_{ET}, as:[35]

$$k_{ET} = Ae^{-\Delta E/k_b T}, \tag{2.7}$$

where ΔE is the activation energy shown in figure 2.2, k_b is Boltzmanns's constant, T is the temperature and A is some undetermined pre-exponential factor. It is possible to determine the activation energy from the thermodynamics of the system.[35] Marcus's breakthrough was to consider the two molecules classically as two polarized spheres of charge in a solution.[33] In this model, any amount of charge can pass between the two molecules. The Gibbs free energy, G, required to change the nuclear configuration to move a specific amount of charge, Δe, was found to be:[33]

$$G = (1/r_1 - 1/r_2 - 1/R)(1/\epsilon_{op} - 1/\epsilon_s)(\Delta e)^2 \tag{2.8}$$

where r_1 and r_2 are the radii of the two spheres, R is the separation between the two spheres, with ϵ_s and ϵ_{op} being the static and high frequency dielectric constants of

the medium respectively. This shows that, for a set distance between the molecules a simple harmonic approximation is an appropriate model.[33] In reality, Δe represents the probability of electron transfer, not the actual amount. This model has been shown to be, both using computer simulations[36] and experimentally[37], a very accurate picture.

Using the simple harmonic model, the nuclear potentials can be considered as two intersecting parabolas.[31] Assuming the bottom of the acceptor parabola in figure 2.2, at position A, has the co-ordinates (0,0), and that the donor parabola at position C in figure 2.2, has the co-ordinates (a,b); the equations of the two parabola are $y = x^2$ and $y = (x-a)^2 - b$. The y value at the intersection of the two parabolas is ΔE, which is the activation energy. To find the intersection, we must combine the equations to give:

$$x^2 = x^2 - 2ax + a^2 - b. \tag{2.9}$$

This can be simplified and rearranged to:

$$x = \frac{a^2 - b}{2a}. \tag{2.10}$$

From the original $y = x^2$, we get:

$$y = \frac{(a^2 - b)^2}{4a^2}. \tag{2.11}$$

The co-ordinate b is $-\Delta G_0$, which is the potential energy difference between the electron being at the acceptor site or the donor site, and a^2 is λ, the amount of energy in the medium it would take to reorganize the nuclear configuration to allow for charge transfer to occur in the previous charge distribution.[31] This gives us an equation for the activation energy, ΔE of:

$$\Delta E = \frac{(\lambda + \Delta G_0)^2}{4\lambda}. \tag{2.12}$$

The pre-exponential factor in equation 2.7, A, is given by the equation:[27]

$$A = \nu_{eff} e^{-\beta(d_0 - d)}, \tag{2.13}$$

where ν_{eff} is the effective frequency of sampling coupled to that reaction co-ordinate which is the rate at which the electron would move between the molecules if there was no energy barrier between them. The constant, β, is the damping of the electronic wave function in the barrier region separating the two molecules. There is an optimum position for charge transfer, d_0, although this is usually considered to be the distance of closest approach or the direct contact distance.[27] The likelihood of charge transfer decreases with increased distance, d, between the molecules. Bringing all these factors together, results in an equation for the charge transfer rate, k_{ET} as;[37, 27]

$$k_{ET} = \nu_{eff} e^{-\beta(d_0 - d)} e^{\frac{(\lambda + \Delta G_0)^2}{\frac{4\lambda}{k_b T}}}. \tag{2.14}$$

The experimental evidence for the above reaction rate equation is strong.[37] In the adiabatic limit, the damping constituent of equation 2.14, $e^{-\beta(d_0-d)}$, becomes close to 1 and ν_{eff}, the frequency of sampling determines the rate. This leads to the charge transfer rate becoming dominated by the dielectric relaxation time of the medium. In the non-adiabatic case, the size of the damping constituent is much smaller than 1 and, in such cases, the size of the barrier determines the charge transfer rate. For two molecules in a solution, most electron transfer reactions occur in the non-adiabatic limit where the coupling is weaker.[27, 28] This is due in large part to the fact that stronger coupling often results in structural and chemical changes in the molecules where the use of Marcus's theory would be inappropriate. The large range of possible barrier heights for charge transfer means that, for two molecules in solution, the average charge transfer time can vary significantly from picoseconds to hours.[27]

2.1 Incorporating surfaces

Having looked at the charge transfer between two molecules, we can use it to discuss charge transfer between a molecule and a solid-state surface. The previous section deals with the situation of charge transfer between two discrete states which are strongly localized. At a solid state surface, the electronic states are more delocalized

and the states are characterized by their electron or hole momentum ($\mathbf{k}$).[29] The simplest quantum mechanical approach to electrons in a crystalline solid is to consider a free electron wave moving through the solid and being subjected to a periodic potential that has the same periodicity as the crystal lattice. This periodic potential is due to the interaction with the atoms in the potential. The one-electron wave functions are called Bloch functions and have the form of a plane wave with propagation vector $\mathbf{k}$ modulated by a periodic potential.[29]

$$\Psi_{\mathbf{k}}(r) = e^{i\mathbf{k}\cdot\mathbf{r}} U_{\mathbf{k}}(r) \tag{2.15}$$

$\Psi_{\mathbf{k}}(r)$ is the Bloch function, $U_{\mathbf{k}}(r)$ is the periodic function of the crystal lattice, and $\mathbf{r}$ is the position vector of the atoms in the lattice. The propagation vector $\mathbf{k}$ characterizes the translational symmetry of the periodic potential with $\hbar\mathbf{k}$ as the crystal momentum.[29] Solving Schrödinger's equation using the Bloch function leads to a solution in which there are a range of energies that are allowed and a range of energies that are disallowed.[29] This depends on whether $\mathbf{k}$ is real (when the energies are allowed) or whether $\mathbf{k}$ is complex (and the energies are disallowed). This means that there are forbidden energy ranges between the allowed regions which are called energy gaps. This approach is called the nearly-free electron model. It works best when the individual atoms interact very strongly and the potential energy of an electron is relatively small compared to its total energy.[27] This leads to smaller energy gaps and works well for metals with fewer electrons and semiconductors with small band gaps.

A different approach is the tight binding approximation, which assumes that the wave function for the crystal is related closely to the atomic wave functions.[29] At large interatomic distances, the energy levels of the solid are similar to the discrete energy levels of the atom. As they are brought together, the overlap between the atomic orbitals causes the discrete energy levels to split into a new set of energy levels. For molecules, this results in the molecular orbitals forming. For extremely large numbers of atoms, such as in a bulk solid, the energy levels form a continuum with forbidden energy gaps that are related to the original atomic levels of the atoms

in the crystal. This approach works better for transition metals and insulators where the allowed bands are smaller and have large energy gaps.[29, 27]

Both the tight-binding approximation and the nearly-free electron give a similar end result. There are energy gaps that electrons cannot be transferred into. Whether a material is a metal or a semiconductor is dependent on where the Fermi energy lies. The Pauli exclusion principle limits the number of electrons in each orbital, meaning that the electrons fill the energy levels up to a certain energy called the Fermi energy.[29] If the Fermi energy lies within an allowed band, the electrons near the Fermi energy need only minimal thermal energy to become free to move around the material. If the Fermi energy lies within an energy gap, the electrons are not free to move around and need external energy to promote electrons into a conduction band above the energy gap within which they can move. For insulators, this gap is very large and generally very few electrons would have the energy (at normal room temperature) to reach the conduction band.

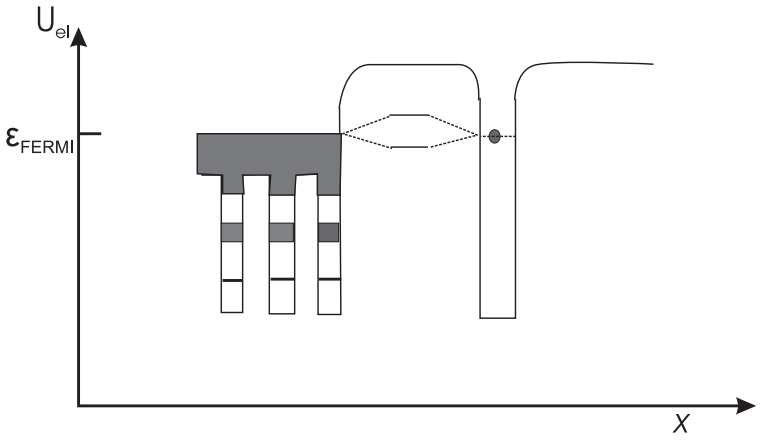

FIGURE 2.3: Quantum well diagram similar to figure 2.1 for interfacial electron transfer. It shows the mixing of the molecular discrete state with the valence band orbitals of the solid state surface.

Models of charge transfer between molecules and surfaces must take account of these very different systems. The electron transfer co-ordinate has to be considered in relation to the presence of the solid state electronic structure with the wide bands. It is instructive to consider the problem as extending the number of atoms that are

interacting with the molecule as shown in figure 2.3. A large number of atoms are brought together to form a cystal. The filled valence orbitals merge into a band of electronic states. The discrete molecular orbitals have some wave function overlap with the electronic sates of the solid.[38] The amount of electronic coupling and consequent mixing of states is dependent on the distance of the molecule from the surface. This drops off exponentially, similar to the two-molecule situation. The amount of electronic coupling between the molecule and the surface would be significantly larger than in the two molecule case as the molecule can overlap with many more atomic orbitals. It is also possible to consider this problem by defining the atomic basis set in terms of Bloch-wave functions characterized by their propagation vector, $\mathbf{k}$. The electronic overlap is summed over all the $\mathbf{k}$ states of the lattice.[38] A diagram of the potential energy surface and the electronic degeneracy at the adiabatic crossing point is represented in figure 2.4. The enhanced coupling sometimes results in chemical reactions in the strong coupling limit.

The charge transfer rate when the charge is transferred from the surface to the molecule, for example between C_{60} and gold,[39] is dependent on the amount of coupling and on whether the charge transfer is adiabatic or non-adiabatic.[38] In the weak coupling limit, the situation is very similar to the two-molecule charge transfer and can be treated the same. In the strong coupling limit, the charge transfer rate is almost completely dependent on ν_{eff}, the sampling frequency. The timescale of the sampling is on a similar timescale to the nuclear relaxation of the molecule in a solution.[38] The lower limit for charge transfer time is determined by the nuclear relaxation on the acceptor molecule and is on the order of 100 femtoseconds. This would only occur in the most adiabatic limit and, under these circumstances, represents the best possible rate.

For the injection of the electron from the molecule into the surface, such as occurs in DSSCs, the limit for charge transfer can be much lower than 100 femtoseconds and many experiments have shown that it can occur in the lifetime of a core-hole excitation.[9, 6] The nuclear relaxation of the crystal is much faster than for the molecule due to the very large number of electronic states. The movement of charge from a discrete molecular species to such a large continuum of states is very entropi-

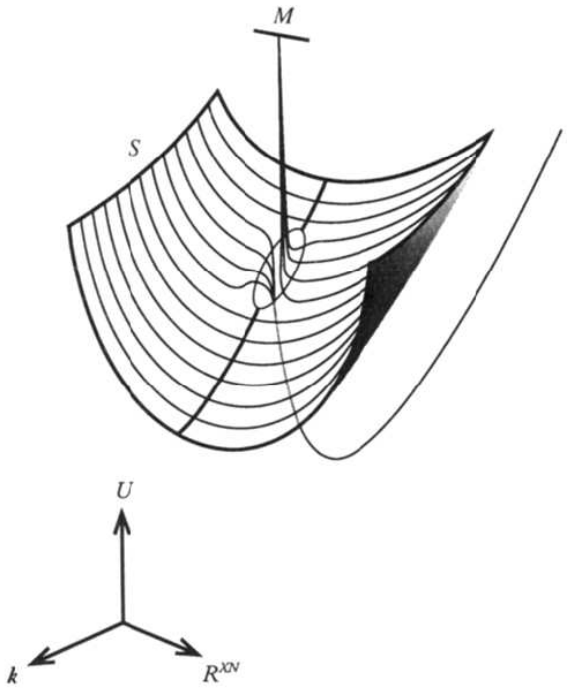

FIGURE 2.4: Potential energy diagram similar to figure 2.2 except that it shows the transfer of charge between a solid-state semiconductor and a molecular orbital. S refers to the semiconductor state and M to the molecular state. R_{XN} is the reaction co-ordinate and represents a cross-section of the multidimensional nuclear potential energy surface. The diagram shows how the large manifold of **k**-states affects the transition probability at the crossing point. Reproduced from reference[38].

cally favourable. The large number of states means that during the mixing resonance, the electron is far more likely to found in the substrate than in the molecule. This means that the molecular relaxation has little effect on the charge transfer time. The charge transfer rate is dependent only on the electronic coupling and on the electronic density of states of the crystal.[38] Ultra-fast charge transfer on timescales smaller than the core-hole decay times (< 6 fs) are theoretically possible and have been verified experimentally.[9, 6]

Chapter 3

Experimental Techniques and Apparatus

For all our experiments, the chamber was kept under ultra-high vacuum (UHV) conditions with a pressure below at least 10^{-9}mbar. This is a density of less than a trillionth of normal air density. There are several reasons why we go to the trouble of doing experiments at these pressures. The main reason is to maintain a clean surface so only the molecules that are deposited are observed on the surface. If there are too many air molecules and other miscellaneous molecules, these would interfere with the signal we observe from the molecules under analysis. The presence of too many molecules can even interfere with the interaction of the molecule with the surface, meaning that it is impossible to get an accurate idea of the bonding and electron dynamics of the molecule-surface coupling. In the case of photoemission, too many air molecules would interfere with the electrons emitted from the sample, making observations practically impossible.

Using UHV conditions, a model description of the electron dynamic processes can be obtained. In so doing, it is implicitly understand that this is not a realistic description for the transfer and bonding in an actual DSSC because exposure to an electrolyte solution or to air would change both the bonding arrangements and the electron dynamics due to the polarization of the surrounding medium. Also, real surfaces have a much larger number of defects and would not be a single crystal. Nonetheless, by looking only at the molecules adsorbed onto the surface in isolation, it is possible to gain insight into the fundamental processes that occur in DSSCs.

In order to produce an atomically clean surface, samples placed within a UHV en-

vironment need to be cleaned *in situ*. They cannot be cleaned and then placed within the chamber without contamination from the air which, in the normal environment, is filled with contaminants. Also, in many cases oxygen molecules have adsorbed onto the surface and this layer needs to be removed. In order to clean the surface, the sample is sputtered with 1 kV argon ions. The ions are made by introducing argon gas into the chamber, then an ion gun ionizes the argon atoms and accelerates them towards the sample. The ions ablate the top layers of the sample off, exposing the underlying clean layers in the bulk. This leaves a very deformed surface, full of defects, which needs to be reformed. Heating the sample allows the surface to reform into its original crystal orientation. After cleaning, the surface is checked using X-ray photoemission spectroscopy to check the carbon 1s peaks and to see whether they disappear. Most contaminants in the environment are organic in nature and contain carbon. Obviously, for surfaces containing carbon such as silicon carbide, this is not effective. Potassium and sulphur 2p peaks can also be checked as they are additional common contaminants. For the inelastic scattering beamline, fluorescence yield x-ray absorption spectra is used to check the sample. For all our samples, the sputtering and the annealing were repeated until the carbon peak disappeared.

3.1 Deposition methods

3.1.1 Thermal evaporation

In order to deposit molecules onto a clean surface, the deposition needs to take place in ultrahigh vacuum conditions. Two different methods were used in our group to deposit the molecules. A Knudsen cell (also known as a K-cell) evaporator was used to deposit thermally stable molecules, such as bi-isonicotinic acid and C_{60}. This is by far the most common method for depositing molecules onto surfaces in UHV surface science mainly due to its ease of use[40]. K-cells are commonly used in molecular beam epitaxy[41]. The K-cells have a crucible secured inside a UHV tube connected to electrodes at the other end. This crucible is made from an element with a very high melting temperature such as tantalum. The molecule to be deposited is placed

in a powder form into the clean crucible of the K-cell before the K-cell is fitted to the vacuum chamber and evacuated. Once under vacuum, with a direct path from the crucible to the sample, the molecule can be deposited onto the surface by heating the crucible to the sublimation temperature of the molecule. Those molecules can then adsorb onto the surface. Depending on the molecule, it is sometimes possible to make sure there is a monolayer by keeping the surface heated. This relies on the bonding between the surface and the molecule being stronger than the inter-molecular bonds. Thermal evaporation using K-cells is the most common method of molecule deposition for in the work in this thesis. It was used to deposit C_{60} onto gold,[39] as presented in Chapter 4, bi-isonicotinic and isonicotinic acid[42] onto gold, as shown in Chapter 5, nicotinic and picolinic acid onto gold, as described in Chapter 6 and bi-isonicotinic acid onto TiO_2[43], as expanded on in Chapter 7.

K-cells are only useful for thermally stable molecules. Some large organic molecules decompose upon heating, resulting in only fragments of the molecule being deposited. In order to obtain an understanding of DSSCs, though, we need to be able to deposit large dye molecules, such as N3, which are thermally labile. To study these molecules adsorbed onto surfaces, it was necessary in the past to deposit on the surface *ex situ*, i.e. outside the vacuum chamber. This, however, was far from ideal, as it meant that the molecules could not be deposited onto a clean surface. The need to deposit these large organic molecules *in situ* was the main motivation behind the successful development of the UHV electrospray deposition system used by our research group at Nottingham. The Nottingham Nanoscience Group has successfully deposited many large molecules such as carbon nanotubes,[44] C_{60},[45, 46] porphyrins,[47] single-molecule magnets,[48] giant porphyrin nano-rings,[49] porphyrin polymer chains,[50] the dye molecule N3[51, 6, 42] and several related dye molecules.[52, 53]

3.1.2 Ultra-high Vacuum Electrospray Deposition

Ultra-high vacuum electrospray depostion (UHV-ESD) allows us to take molecules in a solution or suspension outside the vacuum chamber and deposit them onto the surface inside the chamber. The solution used to dissolve or suspend the molecule de-

pends on the molecule and on what is known, from previous experience, gives the best possible spray. For the N3 molecule, for instance, this is usually a 3(methanol):1(water) mixture but other mixtures involving toluene and methanol are used for molecules such as $N@C_{60}$, Zn-protoporphyrin and single-molecule magnets. Care has to be taken with toluene as it dissolves certain plastics with ease.

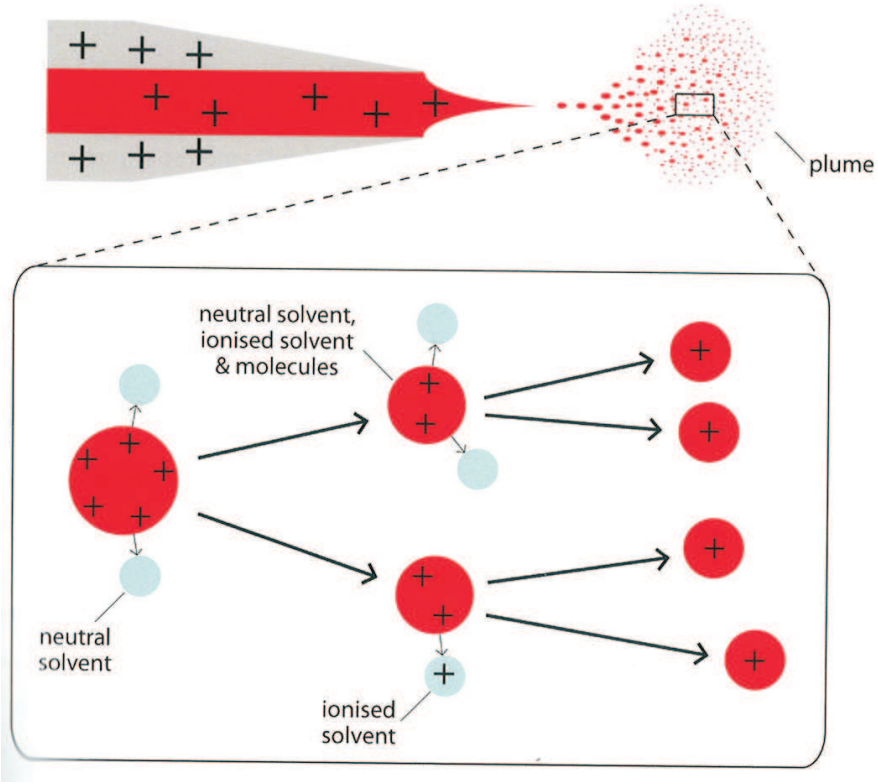

FIGURE 3.1: Schematic diagram of the Taylor cone and the processes which form the plume of droplets. Reproduced with permission from reference [54].

In order to form the molecular ions, the solution containing them is pushed through a narrow hollow stainless steel capillary which is charged at a high voltage(2kV). The stainless-steel capillary is called the *emitter*. Eventually, at the end of the emitter, the ionized liquid forms a tapered shape called a Taylor cone, as shown in figure 3.1. This cone is produced to minimize both the coulomb repulsion and surface tension from the liquid.[55] At a certain threshold voltage, the coulomb repulsion overcomes the surface tension of the liquid and the solvent is emitted in a jet of small

droplets from the end of the Taylor cone. This jet is propelled forwards by the emitter's electric field. As these droplets fly through the air, solvent molecules evaporate from the charged droplets. This causes the volume of the droplets to decrease and, hence, increases the charge density of the droplets. When this charge density gets to certain limit, called the Rayleigh Limit, the droplets break up in what is called a *Coulomb explosion*. The Rayleigh Limit is defined as a function of the charge and diameter of the droplet by the equation:

$$\frac{q^2}{d^3} = 8\pi^2\epsilon_0\gamma, \tag{3.1}$$

where q is the total charge of the droplet, d is the droplet diameter, ϵ_0 is the permittivity of air and γ is the surface tension of the droplet. The smaller resultant droplets lose solvent molecules and break apart again. This repeated splitting results, under optimal conditions, in a fine plume of very small droplets, some of which contain only a single molecule. In order to reach the sample from the air outside the chamber, the droplets pass through an entrance capillary and through a series of differentially pumped chambers until they impinge upon the sample held in the vacuum chamber.

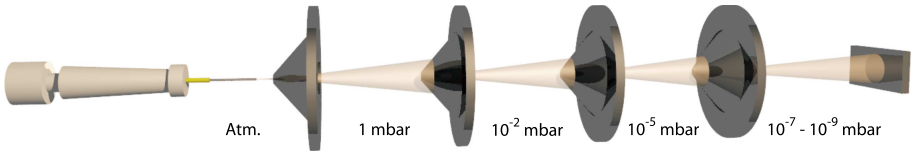

FIGURE 3.2: Schematic of the electrospray system showing the molecular beam traveling as it leaves the high voltage emitter, passes via apertures through differentially pumped chambers and is incident on the sample. Reproduced with permission from reference [6]

To ensure that the molecules can travel to the surface, the alignment is checked beforehand by shining a light through the electrospray chambers and into the main vacuum chamber and trying to observe the reflection of the light on the sample. The molecular coverage is controlled by the deposition time. In practice, the molecular flux is not always constant. The molecular flux can be indicated by either the change in pressure in the chamber or by the electronic current on the sample. The molecular

coverage can be verified by studying the photoemission spectra. This technique was used to deposit the N3 dye molecule onto Au (111) as descibed in Chapter 5.

3.2 Synchrotron radiation

Synchrotron radiation is extremely intense light produced via the radial acceleration of electrons at relativistic velocities. This provides a very wide range of electromagnetic radiation from microwaves to hard X-rays. A by-product of particle physics research, synchrotron radiation was first discovered in 1947 at the General Electric Research Laboratory in Schenectady, New York.[56] Originally considered a nuisance, it was soon realized that it could be very useful for spectroscopic studies. These first synchrotron spectroscopic studies faced great difficulties as they were tacked onto the back of particle physics experiments.[57] This encouraged the development of second generation synchrotrons, such as the 240MeV Tantalus at the Synchrotron Radiation Center in Wisconsin, which, although not originally designed for it, was dedicated solely to the production of radiation.[56] The first synchrotron built purely for radiation production was the 2 GeV Synchrotron Radiation Source (SRS) at Daresbury, England and experiments started there in 1981. As research demands increased, new third generation synchrotrons were developed, designed specifically to improve the brightness and polarization of the light.[56] Currently fourth generation synchrotrons are under development; these are based mainly on the use of free electron lasers.[56]

At synchrotron facilities, electrons are accelerated by the synchrotron and then injected into a storage ring where they circulate in a closed loop. The electrons are maintained in their orbits by bending magnets. The electrons emit radiation as they change direction and this light is projected at a tangent from the ring where it is collected by beamlines. In third generation synchrotrons, insertion devices are placed in the path of the electrons to increase the amount of light produced. Insertion devices consist of a set of magnets whose magnetic fields point alternatively up and down. The electron beam travels between these magnets and is forced into an oscillatory path. The change in direction of the electrons creates cones of radiation which travel down into the beamline. These many small oscillations create very large amounts of

radiation. There are two types of insertion device, *wigglers* and *undulators*, which differ primarily in the amount they force the electron beam to deviate from the straight path. Wigglers cause the electrons to change direction the most and, consequently, have radiation cones which do not overlap with each other. Undulators have much gentler changes in direction, with the radiation cones from each oscillation overlapping with other ones and interfering with each other. These waves then add up to form coherent light. All the work in this thesis was performed on beamlines which used undulators, the undulator spacings being adjustable to improve the intensity for any particular range of x-ray energies.

The synchrotron radiation is funneled via sets of mirrors down a beamline. A particular energy is chosen from the range of energies using a monochromator. It is this ability to select specific x-ray energies that makes synchrotron radiation such an invaluable tool for spectroscopy. Normal x-ray photoelectron spectroscopy (XPS) can only give one or two (in the case of dual anodes) x-ray energies. The x-rays are produced via electron bombardment of a metal which causes core-hole decay, giving very specific discrete energies. Working with synchrotrons allows for the use of techniques which require you to sweep across a range of photon energies, such as x-ray absorption spectroscopy (XAS) and resonant photoemission spectroscopy (RPES), as well as inelastic x-ray scattering. It is even relevant for XPS when studying surfaces. In order to maximise surface sensitivity, it is important to have a low mean-free path of electrons. This guarantees that electrons from the surface dominate the spectra. The mean-free path is dependent on the kinetic energy of the electrons. Electrons with very high kinetic energies can travel quickly through the substance and are, therefore, less likely to interact with atoms. Electrons with very low kinetic energies do not have enough energy to excite electrons in atoms and, so, do not lose energy, resulting in them moving easily through the bulk. Optimal surface sensitivity occurs for electrons with kinetic energy of around 100 eV,[58] as seen in the universal curve diagram in figure 3.3. Using a synchrotron allows us to put the x-ray energy at 100 eV above the binding energy peak we wish to observe so we can gain the maximum surface sensitivity.

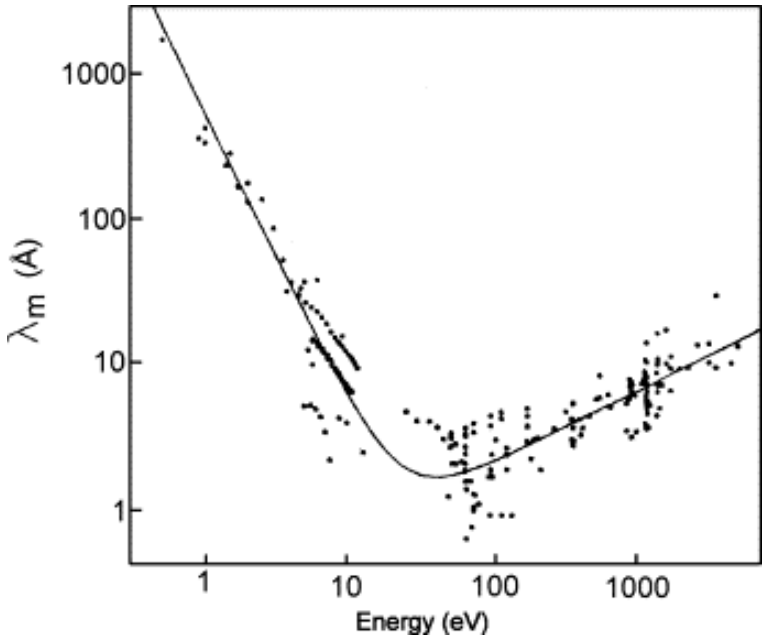

FIGURE 3.3: Diagram showing the mean free path of electrons to escape from a surface for an array of different solid materials depending on the kinetic energy of the escaping electrons. The black line about which the measurements are scattered is called the universal curve. This figure is taken from Ref. [59].

3.3 Photoemission spectroscopy

Photoemisssion spectroscopy (PES) measures the energy of electrons emitted from a sample due to irradiation by electromagnetic radiation. This technique utilises the photoelectric effect, which makes it possible to determine the binding energy of electrons in the atom from the kinetic energy of the electrons emitted and the incoming photon energy. This is achieved using the equation for the photoelectric effect created by Einstein in 1905:[29]

$$E_B^v = h\nu - E_k \tag{3.2}$$

E_B^v is the experimental binding energy with respect to the vacuum level, E_k is the kinetic energy of the emitted electron and hν is the photon energy. The experimental binding energy is dependent mainly on the orbital energy of the emitted electron. In the simplest approach, the measured binding energy is directly related to the orbital

energy. This is known as Koopmans' Theorem, and it assumes that the orbitals remain unchanged by the excitation. This allows us to deduce the approximate electronic structure of the sample. The binding energy can be found with respect to the Fermi level, E_B^F and is related to the experimental binding energy by the addition of a work function, Φ_0, of the sample, which is the energy it takes to remove an electron from the Fermi level to the vacuum level.

$$E_B^v = E_B^F + \Phi_0 \tag{3.3}$$

It is often easier, experimentally, to reference the binding energy to the Fermi level than to the vacuum level. Referencing to the vacuum level requires a decent knowledge of the work functions in the experimental system. On the other hand, the Fermi level acts as a reference point in the XPS spectrum because, at least for metals, it is the highest occupied energy state seen in the spectrum. It is more straightforward to reference the apparent binding energies to this.

The kinetic energy of the electrons is determined using a hemispherical electron energy analyser, as shown in figure 3.4. The electrons emitted from the sample are attracted towards the analyser entrance. A set of electrostatic lenses work to accelerate or retard the motion of the electron, changing the kinetic energy of electrons with a specific kinetic energy to the pass energy of the spectrometer. Using an electrostatic field, the electrons are accelerated around a curve. Only those electrons close to the pass energy of the spectrometer will be able to get round the curve to the detector. The incoming kinetic energy of the electron determines the flight path of the electron and the final impact position, on the multi-channel plate detector at the other end, represents the kinetic energy. From this, a spectrum can be obtained for the kinetic energy of the electron for a specific photon energy. The analyser has two modes of detection: swept mode and fixed mode. Swept mode alters the retardation voltages to change the specific kinetic energy required for the electron to be at the pass energy of the spectrometer. The detector measures the total amount of electrons that hit it for each different kinetic energy. This is useful for measuring a broad range of binding energies. Fixed mode keeps the retardation voltage the same but measures

where the electron hits the detector, as that would determine its kinetic energy. This is useful in situations which look at a very narrow energy window and requires high energy resolution.

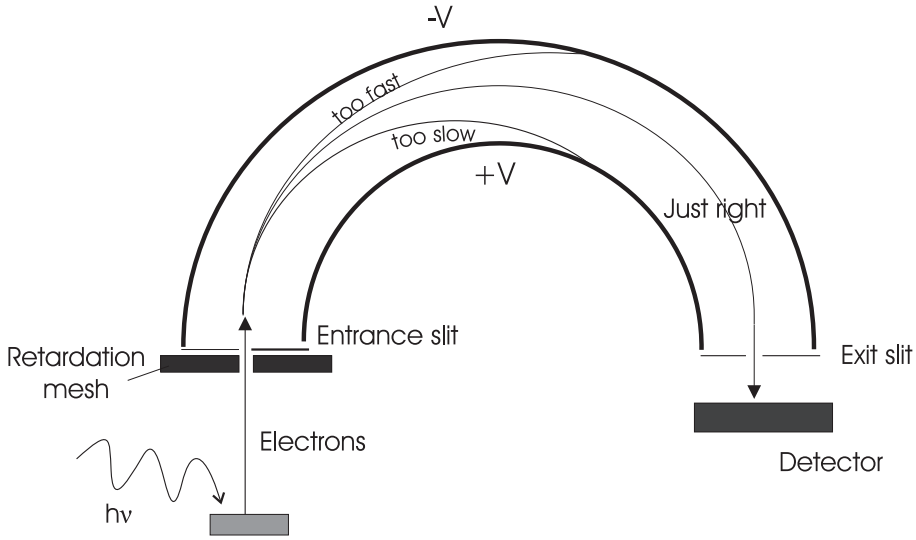

FIGURE 3.4: A schematic diagram of a hemispherical electron analyser.

There are two main types of photoemission spectroscopy, x-ray photoemission spectroscopy (XPS), which uses x-rays to look at core-level excitations, and ultraviolet photoemission spectroscopy (UPS), which is used mainly for studying valence bands close to the Fermi energy. Historically, the distinction is based on the light source used.[60] Ultra-violet photoemission uses noble gas lasers or helium lamps to generate ultraviolet wavelengths. X-ray photoemission uses electron bombardment of metals such as tungsten, aluminium or magnesium to produce x-rays specific to core-hole decay. Using synchrotron radiation blurs the boundary due to the wide range of photon energies it can produce. We used mainly core-level XPS in our experiments.

Superficially, we would expect that the photoelectron kinetic energy spectrum should be representative of the density of states of the occupied electronic states in the surface. There are a couple of issues with this description. One of these issues is that the cross section of the interaction between the incoming photon and electrons in the surface is not the same for all states. The probability of an electronic transition, $P_{i\to f}$, between an initial state, $|i>$, and a final state, $|f>$, is determined using

Fermi's Golden rule:[29, 61]

$$P_{i\to f} = \frac{2\pi}{\hbar}(< i|H|f >)^2\rho(\epsilon), \tag{3.4}$$

where H is the Hamiltonian of the interaction between the photon and the electron and $\rho(\epsilon)$ is the density of states for the final state for the defined energy range. The initial and final states include all the electrons in the molecule or atom as all the electrons are affected by the perturbation caused by the photon. The perturbation can be derived by considering the interaction of the electromagnetic plane wave with a vector potential, $\mathbf{A}$, wavevector ($\mathbf{k}$) and a direction of polarisation ($\hat{\mathbf{E}}$) with the electrons in the atomic orbitals. This then provides, to a first approximation, the equation:[61]

$$H = \frac{e}{mc}\mathbf{A}\cdot\mathbf{p}, \tag{3.5}$$

where e is the electronic charge, m is the electron mass, c is the speed of light and $\mathbf{p}$ is the sum of all the individual electron linear momentum operators. The magnitude of the vector potential, A_0, is related to the magnitude of the electric field vector, E_0, via the equation:

$$E_0 = A_0\omega/c \tag{3.6}$$

ω is the frequency of the light. By using a plane wave, the perturbation can then be derived as:[61]

$$H = \frac{eA_0}{2mc}e^{i\mathbf{k}\cdot\mathbf{r}}\hat{\mathbf{E}}\cdot\mathbf{p}. \tag{3.7}$$

When the wavelength of the light is significantly larger than the atomic radius, when $r \ll \lambda/2\pi$, then $\mathbf{k}\cdot\mathbf{r} \ll 1$ and hence $e^{i\mathbf{k}\cdot\mathbf{r}} \simeq 1$. This is called the dipole approximation and allows the perturbation to be simplified to $H = (eA_0/2mc)\hat{\mathbf{E}}\cdot\mathbf{p}$. The probability of transition can then be written in terms of the electric field as:[61]

$$P_{i\to f} = \frac{e^2E_0^2\pi}{2\hbar m^2\omega^2}(< i|\hat{\mathbf{E}}\cdot\mathbf{p}|f >)^2\rho(\epsilon). \tag{3.8}$$

To obtain the x-ray absorption cross section (σ_{xray}), the transition probability has to be divided by the number of photons that travel through the unit area per unit time. The cross section is then:[61]

$$\sigma_{xray} = \frac{4\pi^2 e^2}{m^2 c\omega}(< i|\hat{\mathbf{E}} \cdot \mathbf{p}|f >)^2 \rho(\epsilon). \tag{3.9}$$

The linear momentum operator, $\mathbf{p}$, can be written in a variety of equivalent forms:[60]

$$\mathbf{p} = \frac{im\omega}{\hbar}\mathbf{r} = \frac{i\hbar}{\omega}\nabla V. \tag{3.10}$$

$\mathbf{r}$ is the sum of the electron positions, ∇ is the sum of the gradient operators and V is the potential energy from the electron-nucleus attraction and electron-electron repulsion in the Hamiltonian of the atom or molecule. As the polarization direction is not a function of the final and initial states, this shows that:

$$\sigma_{xray} \propto |\hat{\mathbf{E}}\langle f \mid \mathbf{r} \mid i\rangle|^2, \tag{3.11}$$

where $\langle f \mid \mathbf{r} \mid i\rangle$ is the dipole matrix element. This term restricts the change in orbital angular momentum (OAM) quantum number (Δl) to ± 1. This makes sense as, in terms of conservation of angular momentum, the photon has an intrinsic angular momentum of $\pm\hbar$ and so limits the possible change in orbital angular momentum.

These selection rules for orbital transitions are only truly valid in the dipole approximation. In reality, forbidden transitions do occur (albeit at lower intensities) due to higher order terms in the interaction. The validity of the dipole approximation depends on the size of the atoms and the wavelength. In the case of nitrogen and carbon, where we used a photon energy of 400 eV and 284 eV respectively, the wavelength of light ($\sim$ 30 Å) is much larger than the diameter of the atom ($\sim$ 0.15 Å). So the dipole approximation is valid in this situation.

Equation 3.9 can be further simplified by considering a single electron model where the excitation of the promoted electron atom is rapid and the inactive electrons do not relax before the excitation is completed. This is known as *the sudden approximation*. The total final and initial states can be separated into the single promoted electron

part (ϕ) and the inactive multiple electron part (Φ). The dipole matrix element can be expanded and simplified to:[60]

$$\langle\phi_f|\mathbf{p}|\phi_i\rangle\langle\Phi_f|\Phi_i\rangle, \tag{3.12}$$

where the momentum operator is specific to the active electron. Higher order terms represent multi-electron excitations. In Koopmans' Theorem, these are ignored and the resultant cross section can be described in a more readily interpretable fashion as:

$$\sigma_{xray} \propto |\hat{\mathbf{E}} \cdot \langle\phi_f|\mathbf{r}|\phi_i\rangle|^2. \tag{3.13}$$

This shows that the intensity of a transition is not just dependent on the density of states and number of molecules. Certain transitions are far less likely to occur and can affect the total absorption cross section due to dipole selection rules. Also, as can seen from equation 3.13, the direction of polarization of the incoming radiation is very important. If the molecules are not randomly orientated, then the cross section can change when the sample orientation to the incoming radiation is changed.

As well as the intensity changing, the binding energy of the peaks can also shift and does not represent the actual electronic structure completely accurately. The assumption that the basic photoelectric effect in equation 3.2 is correct assumes Koopmans' Theorem. The binding energy observed from this equation is called Koopmans' energy. In reality, this energy is never actually observed. The removal of an electron causes the other electrons in the atom to shift to lower energies in order to screen the atomic nucleus more effectively. This means that the outgoing electron would have less kinetic energy than before as it would have more binding energy. The difference in energy between the real binding energy and Koopmans' energy can be represented by a relaxation energy (E_a). So equation 3.2 can be modified to:[60]

$$E_b = h\nu - E_k + E_a \tag{3.14}$$

This is only true if the photoemission process was a slow process because the electron relaxation takes some time to reach a stable equilibrium. In reality, the pho-

toemission process is far more rapid and the sudden approximation used by Koopmans is more valid. The final state may either be one where the electron has been excited to a bound state or where it has been excited into the continuum. There is consequently less kinetic energy available for the emitted electron. These lead to either shake-up features (when electron is excited to a bound state) or shake-off features (in the case of direct ionisation).

These final state effects cause the effective binding energy to shift and have to be considered when analysing the results. There are also other effects which cause a shift in the energy of the emitted electrons, but these shifts can actually provide important information. The surrounding environment can cause the energy levels within the atom to shift. This is called a *chemical shift*. This allows us to identify functional groups in a compound and determine the bonding arrangements between molecules and surfaces. X-ray photoemission spectroscopy is very useful for identifying elements present in wide energy scans and for determining the chemical environments of the specific elements using narrow energy scans.

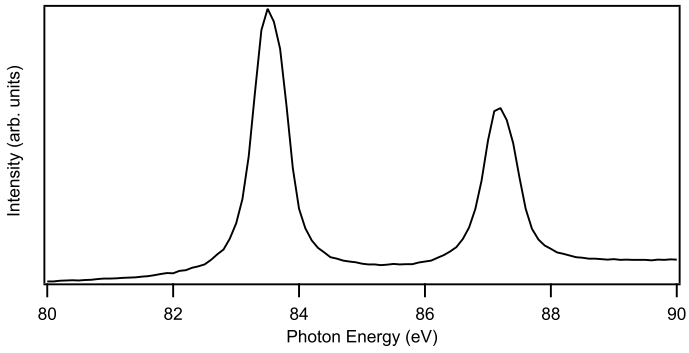

FIGURE 3.5: Au $4f$ peaks at a photon energy of 140 eV.

As well as these chemical shifts, splitting of core-level peaks can also occur, such as for the Au $4f$ peaks (particulary pertinent to the work in this thesis), which is due to an effect called spin-orbit coupling. This involves the coupling between the spin of an unpaired core electron with its orbital angular momentum. The paired electrons' spin (S) cancel each other out to have no overall spin, but the unpaired spins can be either parallel or anti-parallel to the direction of its orbital angular momentum (L).

Where there is one unpaired electron, this leads to two discrete states, with the total momentum: $J = L \pm \frac{1}{2}$. In the case of Au 4 f shown in figure 3.5, $L = 3$ which splits the peak into two discrete peaks, corresponding to Au $4f\frac{5}{2}$ and Au $4f\frac{7}{2}$. The intensity ratio of these peaks is given by $2J + 1$ so resulting in a Au $4f\frac{5}{2}$: Au $4f\frac{7}{2}$ intensity ratio of 6:8. The separation in energy of peaks is proportional to the orbital angular momentum.

3.3.1 Near Edge X-ray Absorption Fine Structure

Near edge X-ray absorption fine structure spectroscopy (NEXAFS), also known as X-ray absorption near edge structure (XANES), is a form of X-ray absorption spectroscopy (XAS) which is used to study the unoccupied bound states in an atom or molecule. (For the purpose of this thesis, the terms NEXAFS and XAS are used interchangeably but when other forms of XAS are used (such as fluorescence yield XAS), they will be mentioned explicitly.) Whilst irradiating the sample, the photon energy is scanned for a range of values below the ionisation threshold for a particular core energy level of an atom in the system. For certain photon energies, the electron is promoted into bound unoccupied orbitals of the system, leaving a core-hole behind. This is a highly unstable arrangement, consequently the electrons rearrange themselves so that the core-hole is filled. This rapid process is called core-hole decay and, due to the conservation of energy, results in either the emission of a photon, which will be discussed further in the x-ray emission spectroscopy section, or the emission of an electron. Electrons emitted due to core-hole decay are called auger electrons. The auger electron has a kinetic energy which is independent of the original photon energy and is a function of the binding energy of the core level, E_{Core}, the original energy level of the electron which dropped into the core hole, E_X, and the energy level the auger electron was emitted from, E_Y. This results in the equation:

$$E_{Auger} = E_{Core} - E_X - E_Y \tag{3.15}$$

Auger decay can be observed in wide energy scans in XPS and is identified because the electron binding energy position seems to shift depending on the photon

energy. For atoms with low atomic numbers, such as carbon or nitrogen, core hole relaxation often results in the emission of an auger electron.[61, 62] During NEXAFS, the number of Auger electrons emitted is directly proportional to the amount of x-ray absorption and consequent excitation.[61] The total number of electrons emitted from the sample is detected at each photon energy via a NEXAFS detector. From this, we can determine the density of states in the unoccupied orbitals in the *core-excited state*. An important point to remember is that we cannot study the unoccupied states in the ground state directly, but we can infer them from what we observe in the core-excited state. The ground state can be considered to be almost the same as the core-excited state, but shifted in binding energy due to the presence of a core-hole.[61, 62] Also, as mentioned before, the absorption cross-section is not only dependent on the density of states, but also on the momentum of the final and initial states and on the direction of polarization.

The term 'NEXAFS' is used instead of 'XANES' mostly in the context of surface science and is often used to probe the unoccupied orbitals of molecules adsorbed onto surfaces.[61] Perhaps surprisingly, the presence of the surface can make it easier to measure the bound states, when the molecule is adsorbed to a surface, than when the molecule is free. Only highly localized molecular orbitals are visible in the NEXAFS spectra due to the large interaction of the unlocalized orbitals with the surface orbitals.[63]

NEXAFS is highly useful in many situations. One of the most common uses is in determining molecular orientation of molecules adsorbed onto a surface, the technique being particularly helpful for small molecules composed of atoms with low atomic number. Molecular orbitals in all molecules result from the mixing of atomic orbitals. The molecular orbitals from molecules composed of low atomic number atoms are very symmetrical and correlate very well with the spatial arrangement of atoms in the molecule.[61, 63] Two types commonly seen in the unoccupied states are the σ^* orbitals, which are the result of mixing of two $2p_z$ atomic orbitals, and the π^* orbitals, which occur due to the mixing of $2p_x$ or $2p_y$ orbitals.[61] Both these molecular orbitals have a nodal character, i.e. the electrons are more likely to be found in certain directions. In the case of two bonded atoms, the π^* orbitals occur

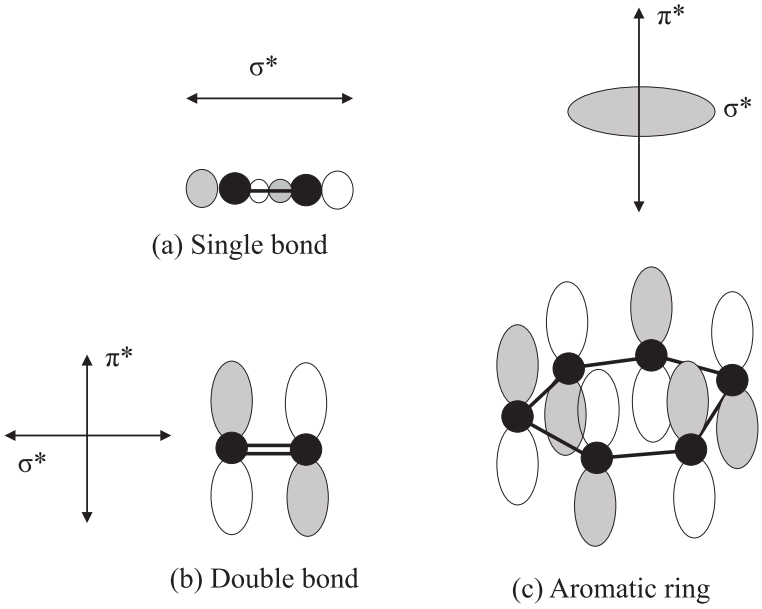

FIGURE 3.6: Schematic illustration of spatial orientation of π^* and σ^* orbitals in three important bonding arrangements. Molecules can be classified depending on whether the π^* or σ^* orbitals point in a specific direction or whether they span a plane.

above and below the bond, whereas the σ^* orbitals lie mainly along and directly opposite the bond,[63] as can be seen in figure 3.6. These two unoccupied molecular orbitals can be observed using NEXAFS. The orientation vector of the orbital, $\hat{\mathbf{O}}$, is aligned with the maximum amplitude of the final state orbital for the excited atom. From equation 3.13, the cross section for the excitation varies as:[63]

$$\sigma \propto | \hat{\mathbf{E}} \cdot \hat{\mathbf{O}} |^2 \tag{3.16}$$

The polarization of the incoming light determines the size of the absorption cross section for each set of orbitals. Synchrotron radiation is unfortunately not completely linearly polarized, being elliptically polarized as well. This makes the relationship between the absorption cross section, the polarization of the light, and the spatial arrangement of the orbitals, not straightforward[61]. This elliptical polarisation can be represented as the superposition of an electric field vector, $\mathbf{E}_{\parallel}$, with another which is perpendicular and 90 degrees out of phase with it, $\mathbf{E}_{\perp}$. The cross section is,

consequently:

$$\sigma \propto \mid \mathbf{E}_{\parallel} \cdot \hat{\mathbf{O}} \mid^2 + \mid \mathbf{E}_{\perp} \cdot \hat{\mathbf{O}} \mid^2 . \tag{3.17}$$

The amount of linear polarisation can be defined as:

$$P = \frac{\mid \mathbf{E}_{\parallel} \mid^2}{\mid \mathbf{E}_{\parallel} \mid^2 + \mid \mathbf{E}_{\perp} \mid^2}. \tag{3.18}$$

$\mathbf{E}_{\parallel}$ is the dominant component. Equation 3.17 can be given as;

$$\sigma \propto P \mid \hat{\mathbf{E}}_{\parallel} \cdot \hat{\mathbf{O}} \mid^2 + (1 - P) \mid \hat{\mathbf{E}}_{\perp} \cdot \hat{\mathbf{O}} \mid^2 . \tag{3.19}$$

Figure 3.7 shows the co-ordinate system of the molecule on the surface being irradiated by an incident x-ray and defines the angles between them. Given this frame of reference, we can obtain the cross section and, consequently, the NEXAFS signal intensity (I), as a function of the polar angle of the x-ray to the surface (θ), the angle of orientation of the molecule to the normal of the surface (α) and the azimuthal angle (ϕ).

$$I \propto P \mid \sin\alpha \cos\phi \sin\theta \mid^2 + (1 - P) \mid \sin\alpha \sin\theta \mid^2 \tag{3.20}$$

This equation can be simplified in the situation where the substrate is highly symmetrical. Furthermore, the azimuthal variations can be averaged out meaning that that intensity may be considered purely as a function of the polar angle.

$$I \propto P[\cos^2\theta \cos^2\alpha + \frac{1}{2}\sin^2\theta \sin^2\alpha] + (1 - P)[\frac{1}{2}\sin^2\alpha] \tag{3.21}$$

Fortunately, all the beamlines at MAXlab used to produce the work in this thesis are at least 95 percent linearly polarized.[64, 65] We can then simplify equation 3.21 so that the intensity is then defined as:

$$I \propto \cos^2\theta \cos^2\alpha + \frac{1}{2}\sin^2\theta \sin^2\alpha \tag{3.22}$$

By determining the ratios between the π^* and σ^* intensities, we can use equation 3.22 to produce a best fit for the different intensities for the polar angles (called

a Stöhr fit) and can, hence, determine α, the angle between the molecule and the surface. This is particularly useful in the case for molecular structures where the atoms are all bonded in the same plane, such as pyridine rings,[61] as can be seen in chapters 5 and 6, where this procedure is performed for isonicotinic, nicotinic and picolinic acid adsorbed on Au(111).

3.3.2 Resonant Photoemission Spectroscopy

Another form of photoemission spectroscopy is resonant photoemission spectroscopy (RPES) where, like NEXAFS, electrons are excited from the core-hole to unoccupied bound states of the system. Nonetheless, RPES differs from NEXAFS by determining the kinetic energy (and, hence, the binding energy) of the electrons emitted via Auger decay at the different photon energies. This allows us to study the decay mechanisms and gain further information about the system. The RPES spectra are obtained by performing valence band spectra for a variety of photon energies above the lowest unoccupied molecular orbital. This produces 2-D datasets where the de-excitation channels can be observed clearly. Identifying these channels allows us to determine the amount of ultra-fast charge transfer that occurs from an adsorbate molecule to a semiconductor surface.[62, 9, 66] This charge transfer time, as is mentioned in Chapter 2, is dependent purely on the amount of electronic coupling between the molecule and the surface.

For determining charge transfer processes in DSSCs, RPES is a highly relevant technique. The core-excited bound states, into which the electrons are promoted using RPES, are very similar to those that occur due to optical excitation. Charge transfer that occurs from either core-hole excited or valence-hole excited states can be considered to be very similar.[67]

In the absence of charge transfer processes, the core-hole can decay via two distinct channels, shown in figure 3.8 (b) and (c). These are participator decay and spectator decay. They are collectively known as autoionisation processes. They both emit an Auger electron, resulting in an overall charge increase of the final state of +1. In participator decay, as seen in figure 3.9, the originally excited electron is emitted as

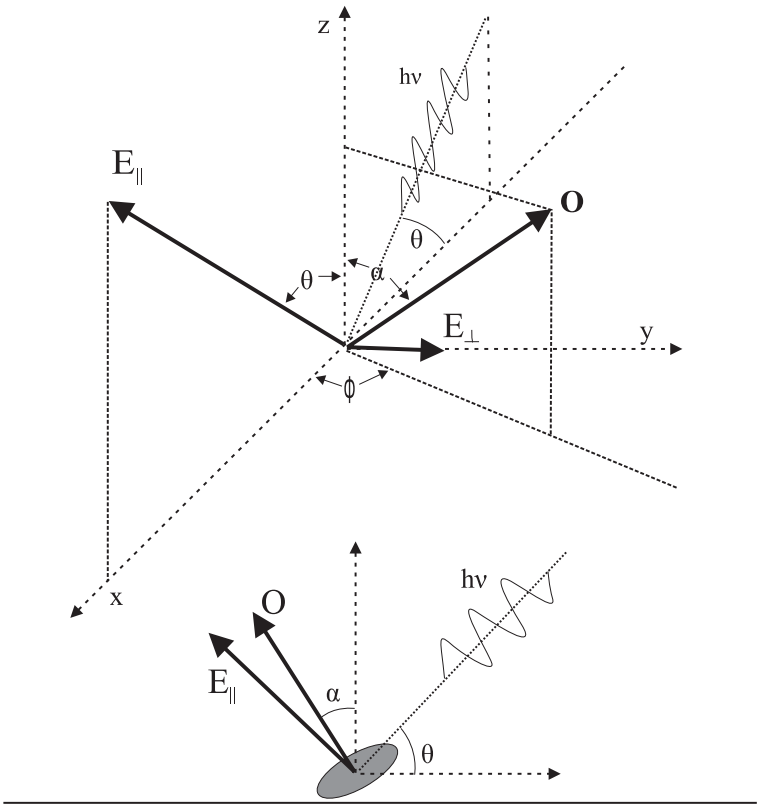

FIGURE 3.7: Diagram defining the angles used to determine the molecular adsorption geometry, with θ being the polar angle of the x-ray with surface and α being the angle between the molecule and the surface normal which is to be determined. On highly symmetrical surfaces (such as Au (111)), the dependence on the azimuthal angle (ϕ) is averaged out. The bottom figure shows a 2D view, along the y-direction, with the shaded area representing an aromatic ring structure.

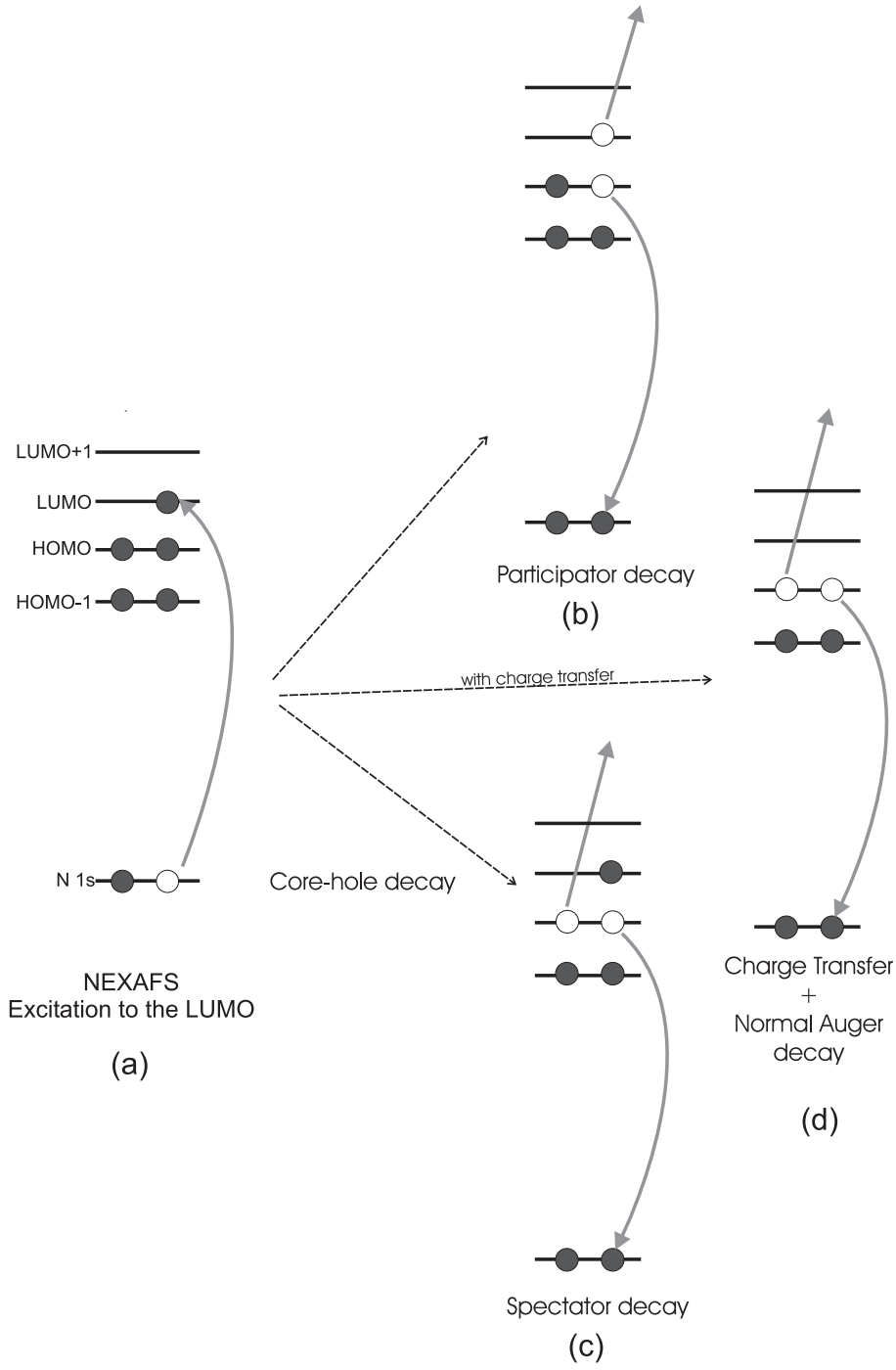

FIGURE 3.8: Diagram showing possible decay channels from a core-excitation seen in (a). Participator decay is shown in (b), where the originally excited electron is emitted as an Auger electron. Spectator decay is shown in (c), where the originally excited electron 'spectates' the Auger decay of another electron from the occupied levels. In the presence of charge transfer to the surface, normal auger decay can occur, as seen in part (d).

an Auger electron. This can be observed in the RPES as a point of high intensity with very low binding energy, as seen in the diagram of a typical RPES Spectrum in figure 3.9. Several points of high intensity can be observed depending on the electronic structure of the occupied valance band, although they may be indistinguishable from a large amount of spectator decay.

Spectator decay, as seen in figure 3.8(c), occurs when it is not the originally excited electron that is being emitted as an Auger electron but rather an electron from the occupied molecular orbitals. The binding energy of the Auger electron emitted in spectator decay is only dependent on the valence-band electrons. This is represented in the RPES spectra by features with a higher binding energy than the participator decay at each resonance, as shown in figure 3.9. The cross section for the spectator decay is much larger than for the participator decay mainly due to the greater number of electrons in the occupied valence band when compared to those in the core-excited bound states, although certain matrix element effects also lower the cross section.[67, 62]

In the presence of transfer of the originally excited electron from the molecule to the surface, we are left with another type of decay, which presents itself as a normal Auger decay, as shown in figure 3.8(d). In practice, this type of decay is not possible to observe directly as it cannot be distinguished from the spectator decay. Nevertheless, it is possible to determine the amount of charge transfer by looking at the reduction in the amount of participator decay relative to the total amount of core-hole decay. This is observed for the situation where the possible charge transfer is maximised, i.e. where there is just a monolayer of the molecule adsorbed onto the surface. This situation is compared with that in which the molecule is isolated from the surface, such as in the case for a thick multilayer of molecules, and no charge transfer can occur consequently. As the charge transfer has to occur in the core-excited state, before the core-hole decays, the core-hole lifetime can be considered as a ‘clock’ counting down in which the charge transfer must occur, limiting the amount of charge transfer that is possible.[62] This allows us to use the technique called the ‘core-hole clock’ technique to provide an upper time limit for ultra-fast charge transfer.

By looking at the RPES spectra in the case of charge transfer, it is possible to

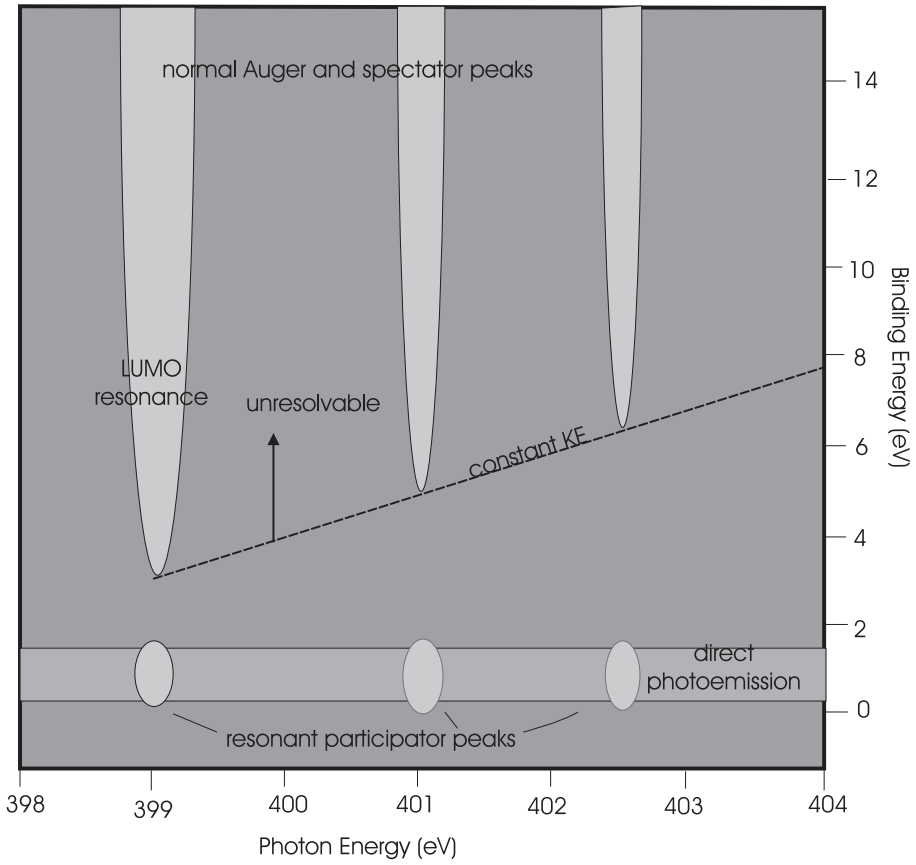

FIGURE 3.9: Schematic diagram of a typical 2-D RPES spectrum. The lighter areas represent areas of higher intensity. As the originally excited electron is emitted from a higher energy level, during participator decay, its respective participator peaks have a much lower binding energy than the spectator peaks and normal Auger peaks found at the higher binding energy range. The spectator and normal Auger peaks cannot be resolved from each other.

make a qualitative observation that the participator peaks have been reduced. This means that the charge transfer must occur on at least a similar time scale to the core-hole lifetime. However, by integrating the RPES spectra over the binding energy of the participator peaks, we can obtain a plot of the intensity of the participator decay at each photon energy (although we have to take into account some direct photoemission intensity at such low binding energies). This allows us to make a quantitative analysis of the charge transfer. In order to make this analysis, we need to make a few reasonable assumptions. Firstly, the core-hole decay and the charge transfer must be independent of each other.[62] Whether the charge transfer occurs or not has no effect on the lifetime of the core-hole decay. Secondly, there is the assumption that both the probability of charge transfer and the probability of core-hole decay are exponential as a function of the time.[62] Both events can be represented as an exponential function of time, t, by the equation:

$$N(t) = N_0 e^{-\frac{t}{\tau}} \tag{3.23}$$

N(t) is the number of molecules remaining unchanged after time t, N_0 is the number of molecules in the excited state before any other event can occur, and τ is the characteristic lifetime for either the charge transfer or core-hole decay. If we represent the occurrence time of a single event, such as core-hole decay, as the variable x, then the probability density, p, of the event occurring at time t is $p(x = t)dt = |dN(t)|/N_0$. The total probability of an event $P(x \leq T)$ occurring before time T is, therefore, $P(x \leq T) = \int_0^T p(x = t)dt$. The probability, then, of core-hole decay occurring before time T is:

$$P_{chd}(T) = \int_0^T \frac{1}{\tau_{chd}} e^{-t/\tau_{chd}} dt, \tag{3.24}$$

where τ_{chd} is the average time for core-hole decay. The probability of *no* charge transfer occurring before time T is:

$$P_{noCT}(T) = 1 - \int_0^T \frac{1}{\tau_{CT}} e^{-t/\tau_{CT}} dt, \tag{3.25}$$

where τ_{CT} is the average time for charge transfer. Assuming that the two events are independent, the probabilities can then be combined to find the probability of core-hole decay without charge transfer. This is given by the equation:

$$P_{chdnoCT}(T) = \int_0^T p_{chd}(t) P_{noCT}(t) dt. \tag{3.26}$$

Substituting equations 3.24 and 3.25 into equation 3.26 gives us:

$$P_{chdnoCT}(T) = \int_0^T \frac{1}{\tau_{chd}} e^{-t/\tau_{chd}} (1 - \int_0^t \frac{1}{\tau_{CT}} e^{-t'/\tau_{CT}} dt') dt \tag{3.27}$$

$$P_{chdnoCT}(T) = \frac{\tau_{CT}}{\tau_{chd} + \tau_{CT}} (1 - e^{-(T/\tau_{chd} + T/\tau_{CT})}). \tag{3.28}$$

Spectra are always measured after the core-excited state has decayed, in the limit $T \to \infty$. The equation then becomes:

$$P_{chdnoCT}(\infty) = \frac{\tau_{CT}}{\tau_{chd} + \tau_{CT}} \tag{3.29}$$

The probability of core-hole decay with no charge transfer is reflected in the ratio between the intensity from the resonant channel (combined spectator and participator decay) and the total combined intensity from resonant and non-resonant decay. This includes the normal Auger decay that occurs in the presence of charge transfer to the surface. So the probability of de-excitation with no charge transfer is:

$$P_{chdnoCT}(\infty) = \frac{I_{resonant}}{I_{resonant} + I_{normalAuger}} \tag{3.30}$$

Equating equations 3.29 and 3.30 gives:

$$\frac{I_{resonant}}{I_{resonant} + I_{normalAuger}} = \frac{\tau_{CT}}{\tau_{chd} + \tau_{CT}} \tag{3.31}$$

Spectator decay and normal Auger decay cannot be resolved in RPES spectra. The participator peaks are separated in binding energy from the spectator and normal Auger peaks because the emitted electron comes from the unoccupied bound states.

This leaves us only with the participator intensity to find the charge transfer. Charge transfer is only possible for molecules coupled to the surface, i.e. a monolayer, and not when it is isolated, i.e. a multilayer. If charge transfer occurs, this would lead to a reduction in the participator intensity ($I^{participator}_{multilayer} - I^{participator}_{monolayer}$). The probability of charge transfer can, then, be considered as the fraction by which the intensity of the participator peak that has been reduced.

$$P_{chdCT}(\infty) = \frac{I^{participator}_{multilayer} - I^{participator}_{monolayer}}{I^{participator}_{multilayer}} \tag{3.32}$$

Core-hole decay always occurs eventually, wheras charge transfer can either happen or not happen. So, in the limit that $T \to \infty$, the sum of the probabilities is 1:

$$P_{chdCT}(\infty) + P_{chdnoCT}(\infty) = 1. \tag{3.33}$$

Substituting and rearranging equation 3.29 gives us:

$$P_{chdCT}(\infty) = \frac{\tau_{chd}}{\tau_{chd} + \tau_{CT}} \tag{3.34}$$

Equating this equation with equation 3.32 gives us:

$$\frac{I^{participator}_{multilayer} - I^{participator}_{monolayer}}{I^{participator}_{multilayer}} = \frac{\tau_{chd}}{\tau_{chd} + \tau_{CT}}. \tag{3.35}$$

This can be simplified to give an expression for the average charge transfer time:

$$\tau_{CT} = \tau_{chd} \frac{I^{participator}_{monolayer}}{I^{participator}_{multilayer} - I^{participator}_{monolayer}} \tag{3.36}$$

This means that the charge transfer time can be obtained from the intensities of the participator peaks for the monolayer and the multilayer. These intensities are normalised by the total cross-sections provided by NEXAFS.

$$\tau_{CT} = \tau_{chd} \frac{\frac{I^{RPES}_{monolayer}}{I^{NEXAFS}_{monolayer}}}{\frac{I^{RPES}_{multilayer}}{I^{NEXAFS}_{multilayer}} - \frac{I^{RPES}_{monolayer}}{I^{NEXAFS}_{monolayer}}} \tag{3.37}$$

The lowest unoccupied molecular orbital (LUMO) should have an energy below the conduction-band edge of the band gap of the semiconductor in the core-excited state. This allows the integrated RPES spectra of the participator peaks to be normalised to the LUMO peak as we know that charge transfer is not possible from the LUMO to the substrate.

As yet we have not considered the opposite situation of charge transfer from the surface to the molecule. In semiconductors, this is negligible, as the chances of an electron localizing on the molecule are low. However, charge transfer to the molecule is more likely when the molecule is adsorbed onto a metallic surface instead. This can produce distinctive features in RPES spectra which are discussed in further detail in Chapters 4 and 5.

3.4 Resonant Inelastic X-ray Scattering

Core-hole decay does not always result in the emission of an Auger electron. Sometimes the core-hole decay emits a photon instead. These emitted photons can be detected and can have their energies (and momenta, depending on the equipment and purpose of the experiment) determined. This is called x-ray emission spectroscopy (XES). A version of XES, called resonant inelastic x-ray scattering (RIXS), can be used to study the bound states of a system near the absorption edge by exciting an electron to the unoccupied bound states below the vacuum level. It provides an atom-specific valence-band structure. RIXS is also called resonant Raman spectroscopy and resonant x-ray emission spectroscopy. Although it is not unheard of for RIXS to be used to study organic monolayers,[68] it is more usually used for bulk studies of materials. This is due to both the low x-ray emission probability (compared to Auger decay) for low atomic number atoms (such as carbon and nitrogen) and for the large escape depth of the emitted x-rays, which decrease the surface sensitivity.[58] That

is why photoemission spectroscopy (PES) is the more widely used tool in surface science.

RIXS has some advantages over PES, though. First, the final state in PES is an ionised state, whereas the final state in RIXS is a neutral state. In the case of the elastic peak (corresponding to the participator decay in PES), the final and initial states are identical. This means that in the case of PES, the electron's apparent binding energy is shifted and does not represent the actual energy positions of the orbitals in the ground state. In RIXS, the energy shift is negligible (there is a very small shift due to a valence-band hole and the presence of an electron in the unoccupied states).[69] So RIXS does give a more accurate picture of the electronic structure. Second, another, arguably more important, reason is that RIXS can be used to look at the valence band structure that is local to a specific element. This atomic specificity can give us a partial density of states for the particular atom in a molecule.[70]

This element specificity is possible because the valence electrons can only decay to fill the core-hole if the orbitals of the core-hole (which is highly localised on the atom) spatially overlap with the valence band orbitals. This situation can be contrasted with the one in PES, where the Auger electron is emitted from anywhere in the molecule and from which we can obtain a complete density of states for the occupied valence band. An additional constraint on the decay is that only certain transitions are allowed. In order to conserve angular momentum and spin during the decay and subsequent emission of a photon, $\Delta l = \pm 1$ and $\Delta S = 0$. This means that not only must the transition not change the spin, but also that an electron can make a transition such as $p \rightarrow s$ or $d \rightarrow p$ but not $s \rightarrow s$ or $d \rightarrow s$. For organic molecules which contain nitrogen, carbon and oxygen, and consist of atomic orbitals of $1s$, $2s$ or $2p$, this implies that the $1s$ core-hole must be filled by electrons from molecular orbitals which contain some admixture of $2p$ orbitals. This means that, from a N $1s$ resonance RIXS spectrum, we can observe the local π^* and σ^* orbitals of the atom.

Despite the difficulties of using RIXS for organic monolayers, it can provide us with useful information. Theoretically, it has long been considered that it should be possible to determine the charge transfer dynamics between molecules and semiconductor surfaces using a RIXS adaptation of the core-hole clock technique, as described

in the previous section. This can be done by comparing the reduction in the size of the elastic peaks for different photon energies (corresponding with bound state resonances) for a monolayer with the reduction for the multilayer. When an electron is transferred into the substrate, as shown in figure 3.10, then the elastic peak should be reduced. This is similar to checking the reduction of the participator peak. The intensity of the participator decay can be found in RIXS by considering the proportion of the decay that occurs due to elastic scattering instead of inelastic scattering. Considering the normalised areas of the elastic peaks, similar to the intensity of the participator decay, we can then get a version of equation 3.36 for RIXS;

$$\tau_{CT} = \tau_{chd} \frac{A^{elastic}_{monolayer}}{A^{elastic}_{multilayer} - A^{elastic}_{monolayer}} \tag{3.38}$$

The presence of the surface can lead to the distortion of the spectra resulting in changes in the relative sizes of the peaks which are not due to purely charge transfer mechanisms. We already know that charge transfer cannot occur from the LUMO, but can do so from the LUMO+1. So we can use the LUMO spectra as a benchmark for the scenario where there is no charge transfer. Any difference between the reduction in the elastic peak for the LUMO and LUMO+1 must be due to charge transfer from the LUMO+1 to the surface. By normalising the areas for the LUMO+1 in equation 3.38 to their respective LUMO peaks, we can then obtain the equation:

$$\tau_{CT} = \tau_{chd} \frac{A^{mono}_{LUMO+1}/A^{mono}_{LUMO}}{A^{multi}_{LUMO+1}/A^{multi}_{LUMO} - A^{mono}_{LUMO+1}/A^{mono}_{LUMO}} \tag{3.39}$$

In chapter 7, we use this adaptation of the core-hole clock technique for bi-isonicotinic acid on TIO_2 to determine the validity of this approach.

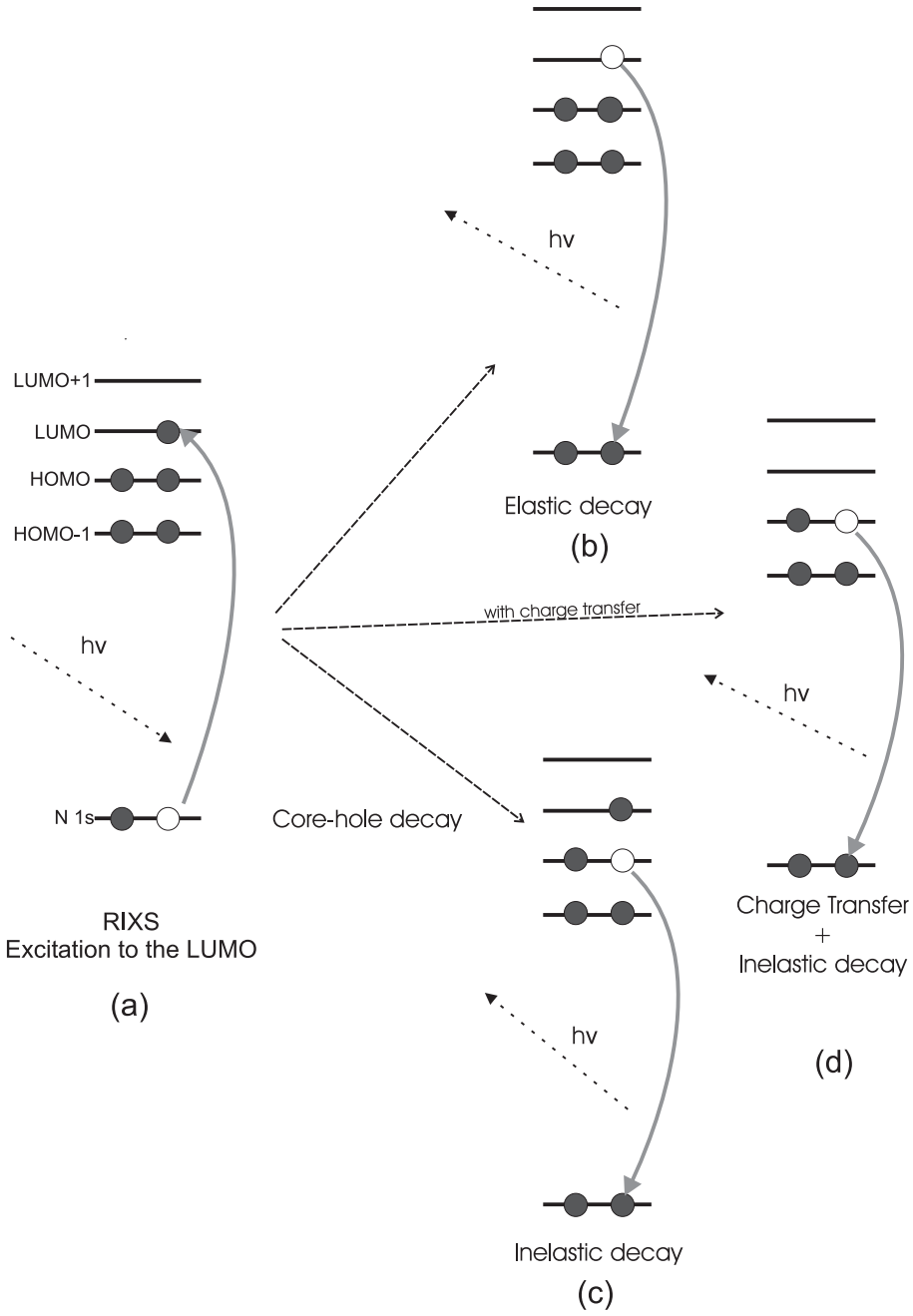

FIGURE 3.10: Diagram showing possible decay channels from a core-excitation seen in (a). Elastic and inelastic decay are shown in (b) and (c) respectively. In the presence of charge transfer to the surface, we observe inelastic decay as seen in part (d).

Chapter 4

Charge transfer between C_{60} on a Au(111) Surface

4.1 Introduction

C_{60} is a fascinating molecule from a nanoscience and molecular-electronics perspective. Since electrons can easily be donated to the fullerene cage from other molecules, atoms and surfaces, C_{60} is an ideal building block for molecular devices. The ease with which electrons can be added to the cage is illustrated by the the electronic properties of the alkali metal (A) fullerides A_nC_{60} that range from insulating to metallic[71] and even high-temperature superconductivity.[72] As was mentioned in Chapter 1, the charge transfer properties of fullerenes and their ability to act as electron acceptors have led to a number of applications in molecular photovoltaics when coupled with electron donors such as porphyrins.[73] C_{60} is known from scanning tunnelling microscopy, among other techniques, to be strongly bound to gold surfaces.[74] This indicates chemisorption and, therefore, the possibility of charge transfer from the surface to the molecule. Indeed, in this experiment, C_{60} monolayers were produced by annealing a thick film of C_{60} to desorb the physisorbed multilayer and leave the more strongly bound monolayer chemisorbed to the surface. In the case of chemical bonding to the surface, we might expect the fullerene LUMO to be partially filled by electrons from the surface. This has been shown to be the case for a C_{60} monolayer on Au(111), where a weak feature around 0.1 eV below the Fermi level, observed in angle resolved

valence band photoemission of this surface, was proposed to be the result of an estimated 0.8 electrons transferred to the fullerene cage.[75] The weak LUMO-derived peak was not observed in earlier angle integrated valence-band studies, although core-level XPS has provided strong evidence of the formation of a chemisorption bond to the surface by modification of the occupied fullerene orbitals.[76]

In this chapter, we look at charge transfer in both directions: from the lowest unoccupied molecular orbitals into the conduction band of the gold substrate, and from states near the Fermi level of the surface into the molecule. The former can be probed using the core-hole clock[62] implementation of resonant photoemission (RPES) which has, in earlier work, led to the quantification of charge-transfer dynamics from adsorbed molecules to both semiconductor[9, 6] and metal surfaces.[24, 7] In the case of metallic surfaces, where there is the possibility for the core-excited LUMO to lie below the Fermi edge of the substrate, our previous RPES data have shown possible evidence for ultra-fast back donation into a small chemisorbed aromatic molecule (bi-isonicotinic acid) on the timescale of the core-hole lifetime.[7, 24] The spectral features associated with this process are constant kinetic energy Auger-like electrons. Their energies are shifted higher than that normally accessible by the molecule with its usual complement of electrons, by an amount corresponding to the difference between the highest occupied and the lowest unoccupied molecular orbitals (HOMO-LUMO). In this chapter, I describe the results obtained for C_{60} adsorbed on the Au(111) surface that show unambiguously that this process involves the charge transfer of electrons from the surface into the LUMO of the molecule, contributing new core-hole decay channels. Yet, the question concerning this and previous work still remains: does this happen in the ground state or in the core-excited state?

4.2 Method

Experiments were carried out at beamline I311 of the Swedish synchrotron facility MAX-lab in Lund. The beamline has a photon energy range of 30-1500 eV and is equipped with a Scienta SES200 hemispherical electron analyzer.[64] The radiation has a high degree of elliptical polarization and may be considered as linearly polarized

for the purposes of this study. The base pressure, in the analysis chamber, was in the mid 10^{-11} mbar range and, in the preparation chamber, it was in the low 10^{-10} mbar range.

The substrate was a single crystal of dimensions 10 mm diameter $\times$ 2.5 mm. It was mounted onto a loop of tungsten wire (0.5 mm) that passed tightly through the body of the crystal, ensuring a good electrical and thermal contact. A thermocouple was attached within the body of the crystal in order to accurately monitor the temperature. The crystal was cleaned along the lines of Barth *et al.*[77] by cycles of sputtering using 1 kV Ar ions and then annealing at 900 K by passing a current through the tungsten wire mount. Surface contamination was checked by monitoring the C 1s core level photoemission peak.

C_{60} was evaporated from a Knudsen cell type evaporator at a temperature of $\sim$ 425 °C onto the sample held at room temperature and at a distance of $\sim$ 20 cm. A multilayer of C_{60} was produced by depositing the molecules for sufficient time so as to suppress the substrate Au 4f photoemission signal and to produce the characteristic symmetric lineshape and shake-up features in the C 1s spectrum.[45] To obtain a monolayer coverage, the sample was then annealed to 300 °C to desorb the physisorbed multilayer so as to leave the chemisorbed monolayer. Again, the monolayer coverage was checked by monitoring the C 1s and Au 4f core-level peaks and the emergence of the characteristic asymmetric lineshape of the C 1s peak,[45] as well as the C 1s:Au 4f peak ratio.

The monochromator exit slits of the beamline were set to give a resolution of $\sim$ 50 meV for photons of energy $h\nu = 340$ eV. The photon energy was calibrated from the separation between the Au 4f peaks measured with 1^{st} and 2^{nd} order radiation. To measure x-ray absorption and resonant photoemission spectra, a taper (+4 mm) was applied to the undulator to reduce the intensity variation of the radiation as the photon energy was scanned. For XAS and RPES measurements, the analyzer's pass energy and entrance slits were set to give a resolution of $\sim$ 500 meV with respect to binding energy. The analyzer was also set to record spectra in fixed mode for these measurements to give the best compromise between energy resolution and the large number of counts required for 2D resonant spectra. For core level spectra, the

analyzer was set to record in swept mode, as described in chapter 3.

4.3 Results and Discussion

Two-dimensional resonant photoemission datasets were measured for the clean Au(111) surface, a multilayer of C_{60} and a C_{60} monolayer. The monolayer and multilayer datasets are shown in figure 4.1 and were obtained by measuring the valence-band photoemission spectra up to a binding energy of 16 eV for a range of photon energies covering the C 1s absorption edge in 0.1 eV steps, as is described in chapter 3. The clean surface spectrum exhibits simply an intense band due to the direct valence band photoemission of the clean Au(111), as we would expect.

The multilayer spectrum, shown in figure 4.1b, presents a number of features associated with the resonant photoemission of the molecules isolated from the surface in a thick film. The binding energy scale of the multilayer spectrum was calibrated to Fermi level of the substrate via the 2^{nd} order C 1s peak (visible in the top left hand corner of the image) to take account of steady state charging in the thick film. The faint vertical bands, in the background of the spectrum, are the direct photoemission peaks of the C_{60} valence band. Where the photon energy reaches the LUMO resonance, there is a strong resonant enhancement of the HOMO at 1.5 eV and of the HOMO-1 at 2.8 eV. This is known as *participator* decay, as is discussed in chapter 3, and is shown in figure 4.2b. Participator decay arises from the originally excited electron (in this case to the LUMO) being involved in the non-radiative decay of the C 1s core-hole, leading to a final state identical to that of direct photoemission.[62] Due to the isolation of the molecules from the surface in the multilayer, it is impossible for any electron excited to the LUMOs to transfer between the surface and the molecules during the core-hole lifetime, but such electrons can instead *participate* in an Auger-like core-hole decay process.

Since the participator final state (referred to as P_{LUMO} in figure 4.2b) is identical to that of direct photoemission of the valence orbital involved, these electrons exhibit a constant binding energy with increasing photon energy and appear as enhancements of the relevant occupied states at those photon energies corresponding to excitation to

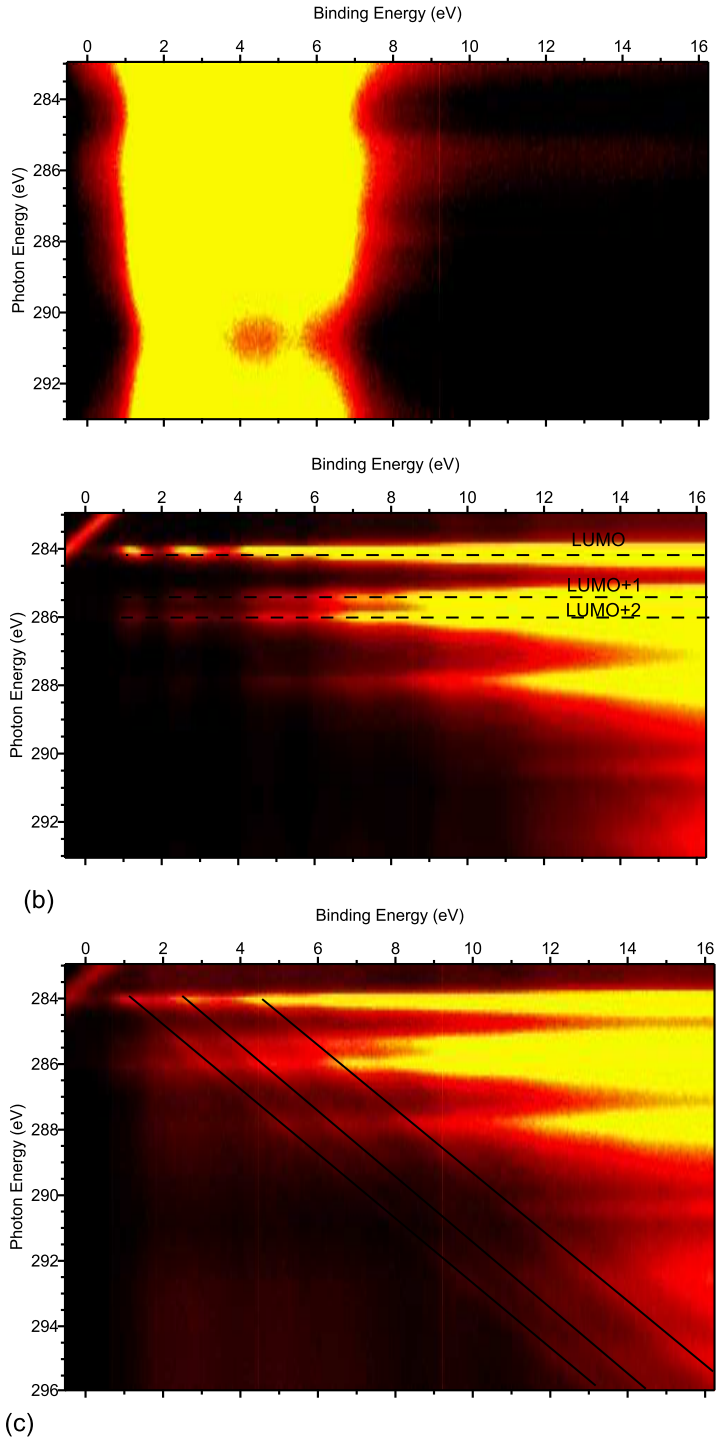

FIGURE 4.1: Resonant Photoemission spectra for (a) clean gold surface, (b) a multilayer of C_{60} and (c) a monolayer of C_{60} with three diagonal lines drawn to highlight the constant kinetic energy Auger features. The horizontal axis represents the binding energy and the vertical axis is the photon energy. The monolayer spectrum was calibrated to the Fermi level of the underlying substrate and the multilayer spectrum was calibrated to the monolayer using the 2^{nd} order C $1s$ peak visible in the top right hand corner to take account of steady state charging in the thick film.

the various LUMO states. In addition to these participator electrons, there are also features which arise from *spectator* decay of the core-hole, as described in chapter 3. In this case, the originally excited electron is not involved in the decay process, but merely spectates as an otherwise normal Auger process occurs, inducing little more than a small and upwards spectator energy shift due its presence in the unoccupied state in question. Spectator electrons, along with normal Auger electrons, account for the high intensity region observed in the RPES spectra on the right hand side – slowly drifting out of the energy window due to their constant kinetic energy. By a consideration of the electronic levels involved, as outlined in figure 4.2, it becomes clear that the highest kinetic energy Auger-like electrons that can be emitted – in the absence of charge transfer – will occur via a process in which two electrons from the HOMO are involved in the decay, spectated by an electron in a previously unoccupied molecular orbital. This is the autoionization decay process referred to as S_{LUMO} in figure 4.2c. The minimum possible energy separation between participator and spectator electrons will occur at the LUMO absorption photon energy and will be equal to the HOMO-LUMO binding energy separation of the molecule.

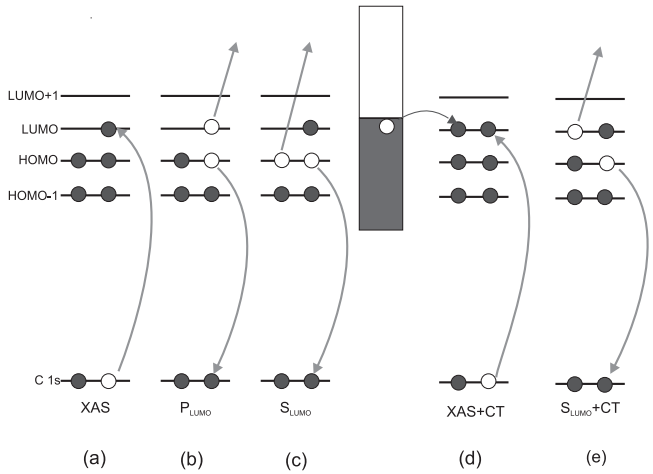

FIGURE 4.2: Electron excitation and de-excitation processes: (a) resonant core level excitation into unoccupied bound states (x-ray absorption); (b) Participator decay following x-ray absorption induced core-hole creation; (c) Spectator core-hole decay; (d) X-ray absorption in the presence of charge transfer from states near the Fermi level of the metal substrate and (e) Spectator core-hole decay in the presence of charge transfer.

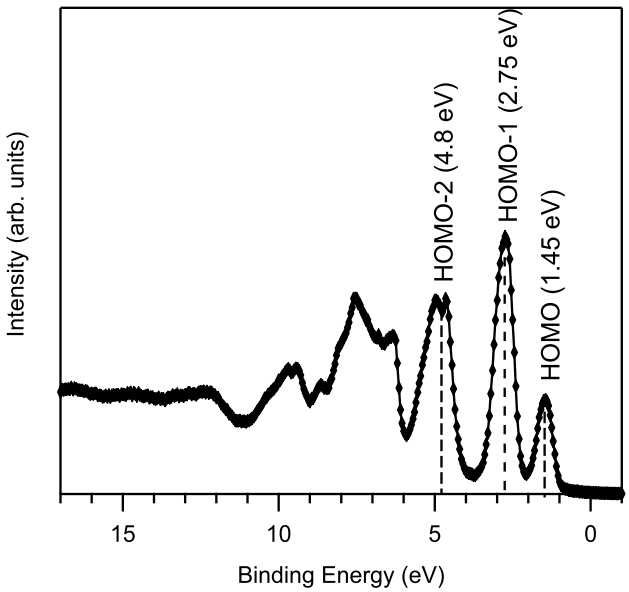

FIGURE 4.3: Valence band photoemission spectrum ($h\upsilon = 60$ eV) for a multilayer of C_{60} on Au(111). The three highest molecular orbital peaks have similar spacings to the spectator bands in the RPES spectra for the monolayer (figure 4.1c).

Turning to the RPES spectrum for the C_{60} monolayer shown in figure 4.1c, we now observe three new low binding energy (high kinetic energy) features as diagonal bands. These are found at the low binding energy side of the spectator and Auger electrons. These are absent from both the clean surface spectrum (figure 4.1a) and the multilayer spectrum (figure 4.1b). These three features track with constant kinetic energy and must, therefore, arise from a new Auger-like decay channel available only to those molecules directly coupled to the metal surface. The kinetic energies of the three lines are calculated as 282.3, 281.0 and 278.8 eV respectively ($\pm$0.2 eV), leading to relative energy positions of the three Auger lines of 0, 1.3 and 3.5 eV. The spacings and profile of the constant KE features closely match those of the peaks at the top of the valence band spectrum, as shown for the C_{60} multilayer in figure 4.3. The HOMO, HOMO-1 and HOMO-2 peaks are located at 1.45, 2.75 and 4.75 eV respectively,leading to relative energy positions of the three Auger lines of 0, 1.3 and 3.3 eV.

As a consequence, it is reasonable to assume that the origin of the three constant

kinetic energy features lies in an Auger-like core-hole decay process involving the HOMO, HOMO-1 and HOMO-2 of the fullerene molecule. Furthermore, it is clear that the resulting decay process must involve an interaction with the gold substrate since these features are absent from the multilayer or the clean Au(111) spectra. In most cases, we might expect the transition probability and, therefore, the intensity of the resulting Auger-like features to get weaker going from HOMO to HOMO-1 and HOMO-2 due to the diminishing spatial overlap with the LUMO. Here, however, the effect is suppressed due to the LUMO and HOMO levels being largely delocalized over the whole C_{60} cage.[78]

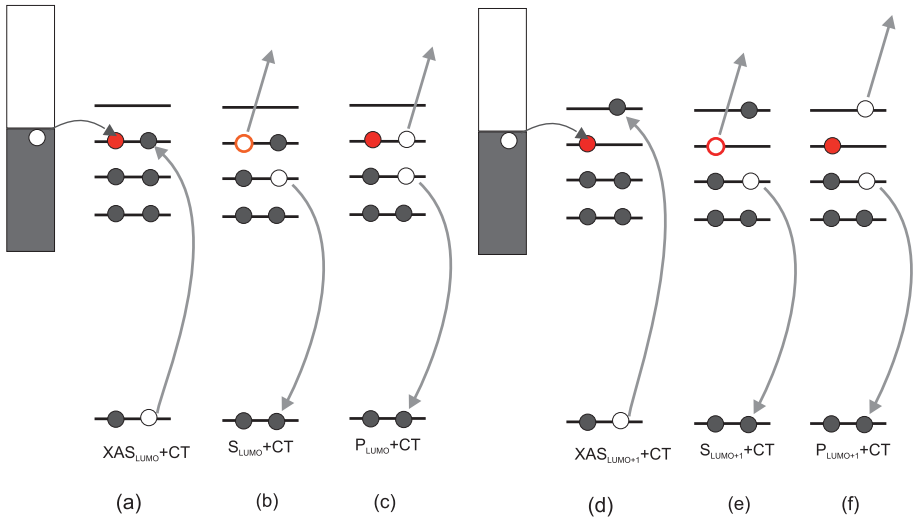

FIGURE 4.4: Electron excitation and de-excitation processes involving charge transfer. In all scenarios, the charge transferred electron is coloured in red. On the left, we have those processes involving the LUMO: (a) excitation to the LUMO in the presence of a charge transferred electron; (b) spectator decay from LUMO with charge transfer; and (c) participator decay from LUMO with charge transfer. On the right, we have those processes involving the LUMO+1: (d) excitation to the LUMO+1 with charge transfer; (e) spectator decay from LUMO+1 with charge transfer; and (f) participator decay from LUMO+1 with charge transfer.

If we focus the discussion - for the moment - on the highest kinetic energy feature, assigned to a core-hole decay channel involving an electron from the HOMO, we see that the kinetic energy is too high for it to be due to a simple spectator process. Indeed, if we extrapolate the path of this feature back to the LUMO absorption

energy, we find that it intersects with the binding energy of the HOMO itself. So, when the originally excited electron is excited to the LUMO, the resulting final state of the decay process is one that is indistinguishable from a participator decay process involving an electron from the HOMO. As illustrated schematically in figure 4.4, this can only occur if an additional electron is transferred from the gold substrate into the LUMO prior to the core-hole decay process. The process referred to in figure 4.4b as $S_{LUMO} + CT$ is a spectator decay channel involving an electron from the HOMO (or HOMO-1, HOMO-2 for the other two bands in figure 4.1c) and a charge-transfer process into the LUMO from states near the Fermi level of the Au(111) substrate. This results in a final state which is identical to direct photoemission of the adsorbed molecule following a charge-transfer event. Contrast the situation with excitation to the LUMO where the spectator and participator decay are at the same energy, shown in figure 4.4(a)-(c), with the one for the LUMO+1, shown in figure 4.4(d)-(f), where the spectator decay and participator decay have different binding energies. As such, we will use the term *superspectator* to refer to all such processes involving an electron transferred from the substrate so as to distinguish them from normal spectator decay.

In the case of probing charge transfer *from* an adsorbed molecule to the conduction band of the surface to which it is bound, monitoring the participator channel can actually elucidate the dynamics of that process.[9, 6, 62] This technique is described in detail in Chapter 3. When examining charge transfer in the other direction, however, the presence of a superspectator decay channel does not, on its own, tell us anything about *when* the electron was transferred to the molecule. Charge transfer between the molecule and the substrate in either direction depends on the energetics of the lowest unoccupied molecular orbitals with respect to the substrate density of states. If the LUMO lies beneath the Fermi level of the gold surface, then charge transfer is possible. In the core-excited state, the presence of the core-hole can lead to the LUMO state being excitonically pulled down so that it crosses the Fermi level of the gold surface.[67] We can measure the position of the core-excited LUMO with respect to the Fermi level by placing the calibrated C 1s XAS and valence band photoemission for the C_{60} monolayer on a common binding energy scale,[79] as in figure 4.5. The data show the LUMO of the molecule to lie mostly below the Fermi

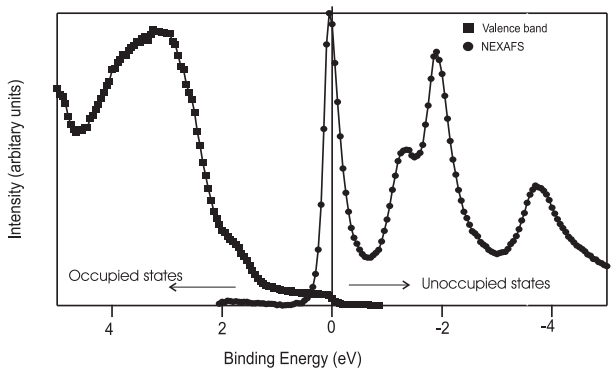

FIGURE 4.5: Energy level alignment of the substrate valence band and the unoccupied molecular orbitals of the molecule. This alignment was created by combining the photon calibrated x-ray absorption spectra and the binding energy calibrated valence band spectra for the C_{60} monolayer.

level of the Au(111) surface. This would theoretically allow the transfer of electrons from the valence band of the metal to the majority of the vibrational states of the LUMO that now lie below the Fermi level. A similar energy alignment was found for bi-isonicotinic acid on Au(111) in which a charge-transfer spectator process was first detected.[24]

While we can directly measure the energy alignment of the LUMO in the core-excited state with respect to the substrate as shown in figure 4.5, x-ray absorption cannot tell us where the LUMO is located in the ground state. Yet there are timescale consequences to this question. If the LUMO lies partially below the Fermi edge already in the ground state, then charge transfer could occur from the surface at any time. However, if the LUMO lies below the Fermi edge only in the core-excited state, then the charge transfer of electrons from the surface to the C_{60} molecule must occur during the core-hole lifetime in order for it to be involved in the core-hole decay process. This would place the charge-transfer dynamics on the the low femtosecond timescale. The key consideration in addressing this question is the extent to which the core-hole pulls down the LUMO in the core excited state[67] when compared to the ground state.

4.3.1 Charge transfer in the core excited state: to and from the molecule

While the superspectator lines are evidence for the presence of charge transfer in the *reverse* direction (from the surface into the molecule), we can get a measure of the charge transfer dynamics in the *forward* direction (from the molecule to the surface) from the participator channel in the RPES spectrum as mentioned above. In figure 4.1, participator peaks are observed for both the multilayer and monolayer, appearing as resonant enhancements of the HOMO, HOMO-1 and HOMO-2 peaks at the absorption energies corresponding to excitation to the LUMO, LUMO+1 and LUMO+2. An integration of the intensity over the HOMO peak as a function of photon energy is shown for both the multilayer and monolayer in figure 4.6, and compared to the associated x-ray absorption spectrum (normalized to the intensity of the LUMO) in both cases.

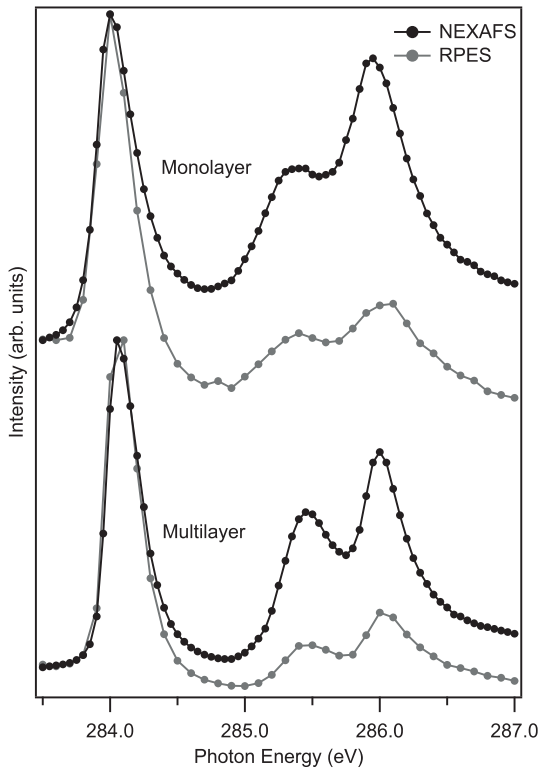

FIGURE 4.6: C 1*s* RPES and C 1*s* XAS spectra of the C_{60} multilayer and monolayer on Au(111). The RPES spectra shown here are binding energy integrations from 0 to 2 eV over for the datasets shown in figure 4.1.

In the case of the C_{60} monolayer on Au(111), an exact quantitative core-hole clock analysis is not possible since the RPES and XAS need to be normalized to the intensity of the LUMO. Because the LUMO of C_{60} in the core-excited state lies, in part, both above and below the Fermi level of the substrate, the possibility of charge transfer into and out of this state renders the normalization quantitatively unreliable. However, qualitatively, there is clearly a very strong participator intensity for the LUMO+1 and +2, indicating a very slow rate of charge transfer (far outside the timescale of the core-hole lifetime) from those states, despite overlapping energetically with the substrate conduction band.

In a general sense, it does not need to automatically follow that slow charge transfer in the forwards direction implies a similarly slow charge transfer in the reverse direction. Nevertheless, charge transfer requires two conditions to be met: there must be energetic overlap so that filled state in the molecule overlap with empty states in the substrate, and there should be sufficient chemical coupling between to provide a charge transfer pathway. The first condition is met for the LUMO+1 and +2 of C_{60} on Au(111), as shown in figure 4.5. Thus, the strong participator channel in this case suggests insufficient coupling to the substrate to facilitate charge transfer on a timescale comparable to core-hole lifetime. Added to this, we have the fact that charge transfer, from a surface to an adsorbed molecule, should in principle be an altogether slower process than the other way around. If we consider an electron passing from molecular states to Au states, this electron will delocalize, existing in a mixed state where it will coherently sample all coupled states. The enormous number of conduction band states reduces the likelihood of the electron returning to the molecular state. Coherence with the initial state is lost on a timescale of the order of 10 fs through electron relaxation processes[80, 81] so the continuum of states is sufficient to localize the electron in the substrate. In contrast, if we consider an electron tunnelling from a continuum of states into a discrete molecular state, charge localization on the molecule should require the breaking of the energy level alignment by nuclear degrees of freedom. The time this takes is of order 100 fs for most molecular species.[80, 81] These conditions may be relaxed to some extent for C_{60}. RPES of solid C_{60} has previously found strong oscillations in intensity and dispersion depending on

small changes in the photon energy at the LUMO, and x-ray emission spectroscopy studies of solid C_{60} also showed a change in the amount of inelastic scattering for different photon energies near the LUMO.[82] These both indicate that ultra-fast vibronic coupling occurs in solid C_{60} on the timescale of the core-hole decay.[82] The existence of such ultra-fast phenomena suggests that ultra-fast charge transfer is not impossible. However, the absence of charge transfer on the low femtosecond timescale in the forward direction should be a strong indicator that a similar timescale cannot be achieved in the reverse direction.

4.3.2 Charge Transfer in the Ground State: To the Molecule

A consideration of charge transfer in the core-excited state suggests that the electrons responsible for the superspectator decay channels in C_{60}/Au(111) are more likely to be transferred from states near the Fermi level of the surface into the LUMO of the molecule already in the ground state. For this to occur, the LUMO would need to lie partially below the Fermi level before the core-excitation. In figure 4.5, the peak of the LUMO state lies just 0.1 eV below the Fermi level in the core-excited state. In order for the LUMO to lie below the Fermi level in the ground state, the effect of the C 1s core-exciton on the position of the LUMO in the XAS must be negligible.

For solid C_{60}, the difference between the energy of the LUMO in the core excited state and the ground state, determined using valence photoemission and inverse photoemission respectively, is around 1.8 eV.[67] This shift is dominated by the Coulomb interaction, estimated to be around 1.5 eV.[62] A similar shift for adsorbed C_{60} would place the ground state LUMO around 1.75 eV above the Fermi level of the Au(111) surface, and no surface-to-molecule charge transfer would be possible. Nonetheless, the screening effect of the metallic surface and the pinning of the LUMO to the Fermi level by virtue of the formation of an ionic bond to the surface might negate the excitonic shift such that the XAS spectrum measured for the monolayer more closely matches the true ground state picture.

A consideration of the energy gain afforded by the image potential, due to the highly polarizable metal surface, and the distortion of the adsorbed fullerene molecule

have previously been shown to drastically lower the HOMO-LUMO gap and would, therefore, feasibly allow an overlap of the LUMO with the Fermi level of the gold surface in the ground state.[76] It is, consequently, theoretically possible for charge to be transferred from the gold surface to C_{60}. Thus, this would lead to the formation of an ionic chemisorption bond. Yet, the partial occupation of the LUMO in the ground state, in principle, should be measurable in valence-band photoemission. The valence-band spectrum ($h\upsilon = 60$ eV) for the C_{60} monolayer on the Au(111) surface, shown in figure 4.5, is insufficient to demonstrate this. However, high-resolution angle resolved valence-band photoemission, measured at lower photon energies, has indeed detected a LUMO-derived peak at a binding energy of 0.1 eV below the Fermi level of the substrate for an annealed monolayer of C_{60} on the Au(111) surface.[75] This peak matches the position of the LUMO precisely in our binding energy aligned C $1s$ XAS in figure 4.5. From the photoemission LUMO-derived intensity, the amount of charge transferred from the surface to the molecules was estimated at around 0.8e per C_{60} molecule. This supported earlier surface-enhanced Raman experiments that suggest that the bonding interaction between gold and C_{60} is largely ionic in nature, albeit less so than on other noble metal surfaces.[83] The occurrence of a lower amount of charge transfer to gold than to other metal surfaces may be due to an interface dipole layer caused by the gold's asymmetric $6sp$-band orbitals at the Au/vacuum interface.[84] So the HOMO and HOMO-1 orbitals will be shifted slightly higher in energy (~ 0.2 eV). This would cause a reduction in the energy gain due to the image potential, although it is not large enough to stop charge transfer from the gold to the C_{60}.

4.4 Conclusions

Our resonant photoemission measurements of a C_{60} monolayer on the Au(111) surface show three distinctive constant kinetic energy features. Their absence from multilayers of C_{60} and from the clean gold surface show that the features are resultant directly from the interaction between the molecule and the substrate. The kinetic energies of these features closely match the separation of the three highest occupied molec-

ular orbtials of C_{60}, indicative of a core-hole decay channel involving electrons from these three orbitals. However, the kinetic energy is higher than can be achieved by the molecule with its ground state complement of electrons, requiring an additional electron to be transferred from states near the Fermi level of the Au(111) substrate into the LUMO, which can then take part in the autoionization core-hole decay process. Moreover, the highest kinetic energy feature of the three features tracks back to the binding energy of the HOMO at the LUMO position. Hence, this results in a final state indistinguishable from both direct photoemission of the charge-transferred molecule HOMO and participator decay in resonant photoemission. The additional electron is most likely transferred from the substrate in the ground state rather than within the core-hole lifetime in the core-excited state. This assertion is based on the observation of very slow charge transfer in the forward direction from the molecule into the conduction band of the substrate, which certainly takes place outside the core-hole lifetime. This agrees with evidence from angle-resolved photoemission in which LUMO-derived intensity was found at the same energy position as we measured for the core-excited LUMO. In the context of x-ray absorption, this would suggest that core-excitonic effects do not play a significant role when the molecule is chemisorbed to a metallic surface in a bonding mechanism largely characterized by charge transfer. Chapter 5 and 6 describe a similar study of small aromatic molecules on the Au(111) surface. Since the intensity of the superspectator features in the RPES spectra of the monolayer should be directly related to the amount of charge transferred to the molecule from the surface, the next step in this investigation is the study of C_{60} monolayers on the Cu(111) surface, where the amount of charge transferred to the fullerene molecules has been estimated from photoemission to be 1.6 eV.[75]

Chapter 5

Charge transfer processes of N3 and Related Ligands on Au (111)

5.1 Introduction

The dye molecule N3 (cis-bis(isothiocyanato)bis(2,2'-bipyridyl-4 ,4'-dicarboxylato)-ruthenium(II)) is a photo-sensitive molecule used in dye-sensitized solar cells (DSSCs).[5, 4] As discussed in Chapter 1, N3 (figure 5.1), is one of the most efficient dyes found for DSSCs. N3 has been shown to bond to TiO_2 via deprotonation of the bi-isonicotinic acid ligand, forming a 2M-bidentate bond to the surface.[6] Bi-isonicotinic acid and the closely related molecule isonicotinic acid also form the same type of bond to the surface via deprotonation of the carboxylic acid group. The chemical coupling allows for the charge transfer of excited electrons from the LUMO of the molecule to the conduction band of the TiO_2. This leaves a hole in the HOMO of the molecule which, in a typical DSSC, is replenished from an electrolyte.[4] As is explained in chapter 1, the need for a liquid electrolyte causes many problems; besides, there have been multiple types of solid-state DSSCs produced without a liquid electrolyte. One type of solid state DSSC, developed by McFarland and Tang,[22] uses a metal-semiconductor Schottky diode with the dye adsorbed onto an ultrathin metal film on top of the TiO_2 layer. The metal film, which in the case of the original cell was gold, provided a source of electrons to fill the hole in the HOMO. Studying the charge transfer between photosensitive dyes - such as N3 and gold - is, therefore, important to understanding

this type of DSSC architecture.

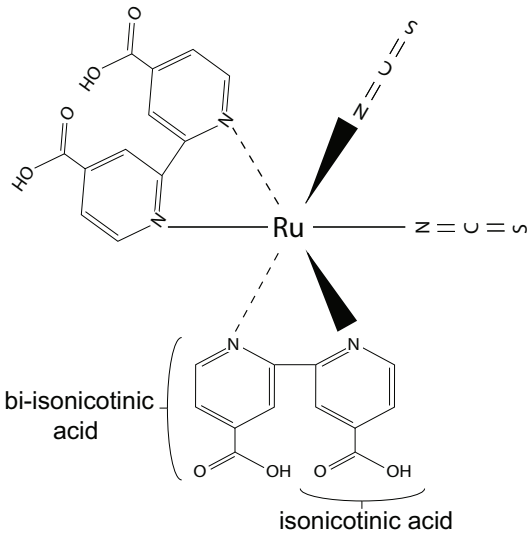

FIGURE 5.1: Schematic representation showing the relationship between the molecular structure of the N3 dye molecule (cis-bis(isothiocyanato)bis(2,2'-bipyridyl-4 ,4'-dicarboxylato)-ruthenium(II)), the ligand molecule bi-isonicotinic acid (2,2'-bipyridine-4 ,4'-dicarboxylic acid), and isonicotinic acid (pyridine-4-carboxylic acid).

Previous work by our group focussed on the adsorption of N3 on gold studied using scanning tunnelling microscopy (STM) and synchrotron-based photoemission.[51] It was found that N3 bonded to gold via a sulphur atom and that it adsorbed preferentially at the faulted regions of the Au(111) herringbone reconstruction.[51] In this chapter, the results from a resonant photoemission spectroscopy (RPES) and x-ray absorption spectroscopy (XAS) study of N3 adsorbed on the Au (111) surface are presented. These techniques allow the electronic structure and the charge transfer interactions between the gold and N3 to be determined by probing the unoccupied levels and the coupling between the surface and the molecule.

Two other molecules, bi-isonicotinic acid[24] and C_{60},[39](see Chapter 4) which have also been deposited on gold, have shown distinctive Auger features in the monolayer RPES spectra. It was shown that these features occur due to an Auger decay mechanism termed *superspectator* decay,[24] in which an electron is transferred from the gold surface to the molecule and acts as a spectator for an Auger decay. As these features are seen for the bi-isonicotinic acid ligand, the presence of *superspectator*

features in the RPES of the N3 dye molecule is studied here, along with the related molecule, isonicotinic acid , in order to probe the charge transfer interactions between the N3 dye molecule and the Au (111) surface.

5.2 Method

Experiments were carried out at beamline I311 of the Swedish synchrotron facility MAX-lab in Lund. The beamline has a photon energy range of 30-1500 eV and is equipped with a Scienta SES200 hemispherical electron analyzer.[64] The radiation has a high degree of elliptical polarization and may be considered as linearly polarized for the purposes of this study. The base pressure, in the analysis chamber, was in the mid 10^{-11} mbar range and, in the preparation chamber, it was in the low 10^{-10} mbar range.

The substrate was a single crystal of dimensions 10 mm diameter $\times$ 2.5 mm. It was mounted on a loop of tungsten wire (0.5 mm) that passed tightly through the body of the crystal, ensuring a good electrical and thermal contact. A thermocouple was attached within the body of the crystal in order to accurately monitor the temperature. The crystal was cleaned along the lines of Barth *et al.*[77] by cycles of sputtering using 1 kV Ar^+ ions and then annealing at 900 K by passing a current through the tungsten wire mount. Surface contamination was checked by ensuring that the C 1s, K 2p and S 2p core level photoemission peaks were below the detection limits of our measurements.

For the deposition of isonicotinic acid, the molecules were evaporated from a Knudsen cell type evaporator at a temperature of $\sim$ 110 °C onto the sample held at room temperature at a distance of $\sim$ 20 cm. The bi-isonicotinic acid was also deposited using a Knudsen cell type evaporator, but at a higher temperature of $\sim$ 230 °C.

The N3 molecule was deposited using an *in situ* commercial UHV electrospray deposition source (Molecularspray, UK) from a solution of $\sim$ 5 mg of N3 in 200 ml of a 3(methanol):1(water) mixture. The full description of the electrospray apparatus and the process of taking molecules from *ex situ* solution to *in situ* vacuum are

described in detail in chapter 3. With the valve open but the needle voltage turned off and thus no electrospray process occurring, the pressure in the preparation chamber was 2×10^{-8} mbar. With the voltage turned on (2 kV), the preparation chamber pressure rose to 5×10^{-7} mbar, the additional pressure being due to residual solvent molecules in the molecular stream. In all preparations, coverage was measured using the intensities of the core-level photoemission peaks and the molecular contribution to the shape of the valence-band photoemission spectra.

The monochromator exit slits of the beamline were set to give a resolution $\sim$ 50 meV for photons of energy $h\nu = 340$ eV. The photon energy was calibrated from the separation between the Au $4f$ peaks measured with 1^{st} and 2^{nd} order radiation. For measuring x-ray absorption and resonant photoemission spectra, a taper was applied to the undulator to reduce the intensity variation of the radiation as the photon energy was scanned. For XAS and RPES measurements, the analyzer pass energy and entrance slits were set to give a resolution of $\sim$ 500 meV with respect to binding energy. The analyzer was also set to record spectra in fixed mode for these measurements to give the best compromise between energy resolution and the number of counts required for 2D RPES spectra. As all three molecules suffer beam damage under irradiation by soft x-rays, RPES measurements were taken as the beam was scanned across the sample at a rate of $1.25 \mu m s^{-1}$. The final RPES spectra were summations of a series of short measurements in order to take account of any change in coverage. For core level spectra, the analyzer was set to record in swept mode with an electron resolution of $\sim$ 100 meV.

5.3 Results and Discussion

5.3.1 Charge transfer from the surface to the molecule

Resonant photoemission spectra for the monolayer and multilayer (both the autoscaled intensity and rescaled intensity versions) of the N3 ligand molecule, bisonicotinic acid, adsorbed by itself on gold are shown in figure 5.2.[24] The core-level photoemission and x-ray absorption spectroscopy have been published previously.[7,

45] The same spectrum was also measured for the clean Au(111) surface. The two dimensional RPES datasets were obtained by measuring the valence-band photoemission up to 16 eV binding energy for the range of photon energies covering the N 1s absorption edge in 0.1 eV steps. The clean surface spectrum (not shown) simply exhibits an intense band due to the direct valence band photoemission of the clean Au(111), as we would expect.

The monolayer resonant photoemission spectrum of bi-isonicotinic acid, shown in figure 5.2b, and with the intensity rescaled in figure 5.2c, has a number of features. The vertical bands, at low binding energy, are the direct photoemission peaks from the gold surface. The high intensity band, at a photon energy of 399 eV, is due to the excitation of an electron to the LUMO from the core N 1s level and the subsequent emission of electrons arising from the decay of the core-hole produced. Hidden in the gold direct photoemission peaks at low binding energy, there is *participator decay* at the LUMO resonance. A diagram of the *participator decay* is shown in figure 5.3b, where the final state is shown to be identical to direct photoemission. The *participator decay* is clearly visible as a strong enhancement at 5 eV binding energy in the multilayer spectrum, in figure 5.2a, and at 3.5 eV in the monolayer spectrum in figure 5.2b.

As well as these participator electrons, there are also constant kinetic energy features which result from *spectator decay* of the core-hole. The *spectator decay* process is shown in figure 5.3c. These spectator electrons, along with normal Auger electrons, account for the high intensity region observed in the RPES spectra on the right-hand side slowly drifting out of the energy window owing to their constant kinetic energy.

The monolayer RPES spectrum of bi-isonicotinic acid on gold shows an interesting diagonal Auger feature that is not observed in the multilayer spectrum. Such features were also observed for C_{60} on Au(111), as described in Chapter 4. The isonicotinic acid RPES spectrum looks almost identical to the bi-isonicotinic acid spectrum, as can be seen in figure 5.4. The charge transfer Auger feature can be seen in the monolayer spectrum as a diagonal line of higher intensity: from a binding energy of 9 eV and a photon energy of 403 eV to a binding energy of 15 eV and photon energy

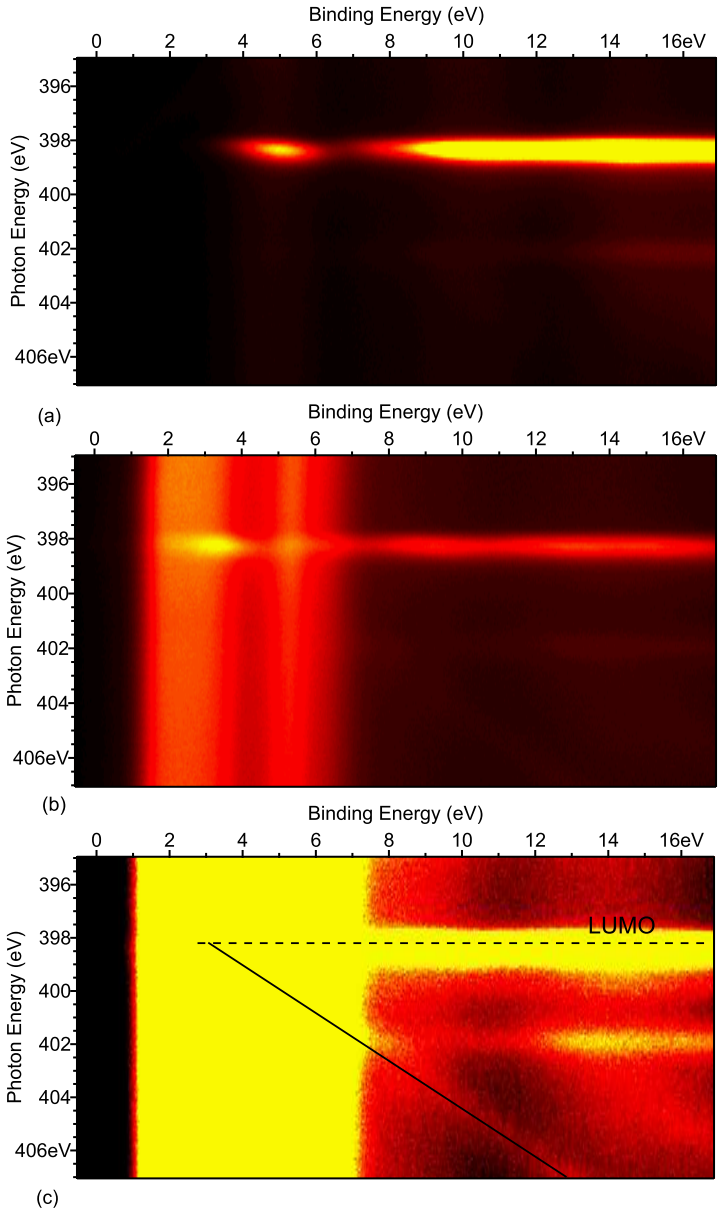

FIGURE 5.2: Resonant photoemission spectra for (a) a multilayer of bi-isonicotinic acid on gold, (b) a monolayer of bi-isonicotinic acid on gold and (c) the same monolayer spectra as shown in (b) but with the intensity rescaled to more clearly show the diagonal Auger features. The horizontal axis represents the binding energy and the vertical axis the photon energy.

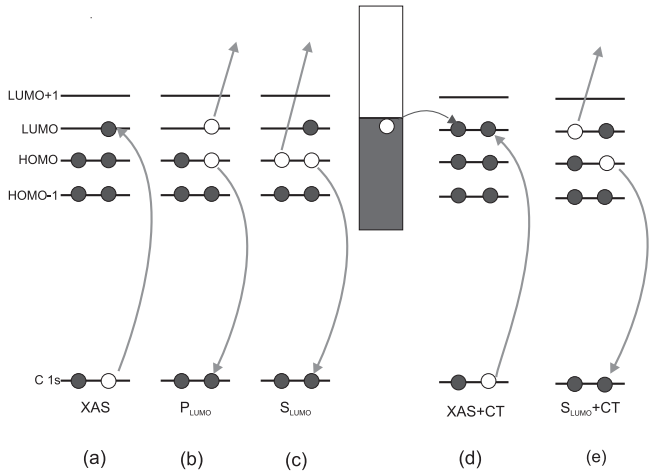

FIGURE 5.3: Electron excitation and de-excitation processes: (a) Resonant core level excitation into unoccupied bound states (x-ray absorption); (b) Participator decay following x-ray absorption induced core-hole creation; (c) Spectator core-hole decay ; (d) X-ray absorption in the presence of charge transfer from states near the Fermi level of the metal substrate and (e) Spectator core-hole decay in the presence of charge transfer.

of 404 eV. This is highlighted by a solid black line on top of it. The feature actually tracks back to the LUMO photon energy at a binding energy of 4 eV, but the lower binding energy is harder to observe because of the high intensity of the direct Au photoemission peaks.

The N3 monolayer spectrum, in figure 5.5b, looks very similar to the N3 multilayer spectrum, except that the gold photoemission peaks are much more pronounced and the molecule's LUMO resonance has a much lower intensity. What is most surprising is that the monolayer spectrum, even when the intensity has been rescaled as in figure 5.4c, lacks the diagonal Auger feature that was observed in the monolayer RPES spectra for other molecules adsorbed on the Au(111) surface. The lack of this feature is interesting, especially as it has been observed for the ligands of the N3 molecule, such as bi-isonicotinic acid.

Charge transfer between the molecule and the substrate, in either direction, depends on the energetics of the lowest unoccupied molecular orbitals with respect to the substrate density of states. For charge transfer to occur, the LUMO must lie beneath the Fermi level of the gold surface. In the core-excited state, the presence

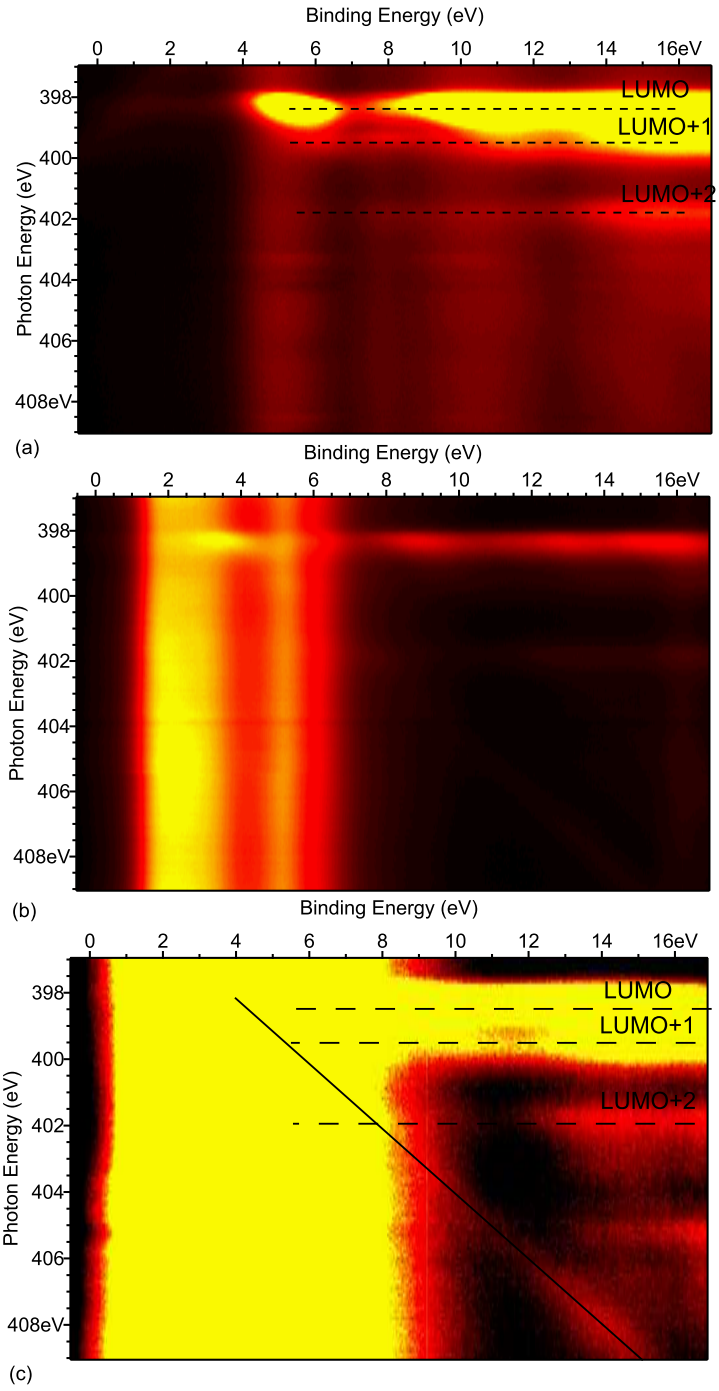

FIGURE 5.4: Resonant Photoemission spectra for (a) a multilayer of isonicotinic acid on gold, (b) a monolayer of isonicotinic acid on gold and (c) the same monolayer spectra as shown in (b) but with the intensity rescaled to more clearly show the diagonal auger features.

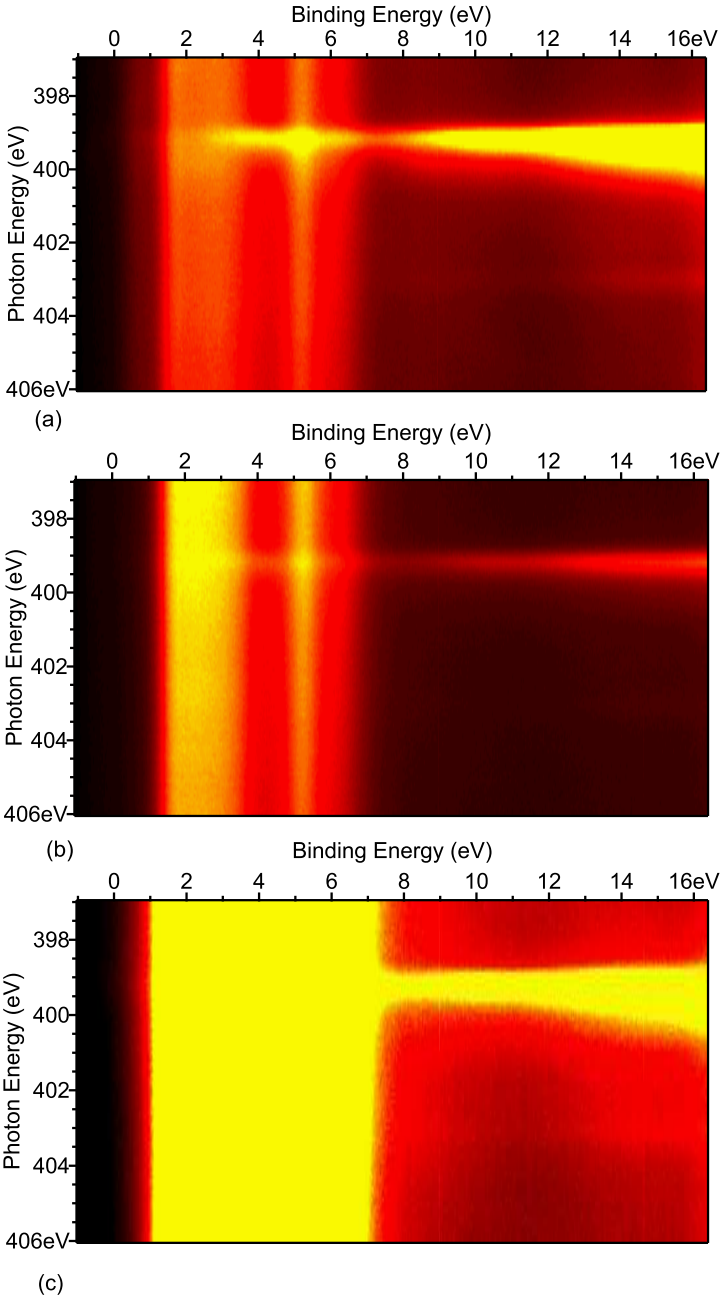

FIGURE 5.5: Resonant Photoemission spectra for (a) a multilayer of N3 on gold and (b) a monolayer of N3 on gold and (c) the same monolayer spectra as shown in (b) but with the intensity rescaled as in figure 5.2 and figure 5.4, showing a clear absence of any diagonal Auger features.

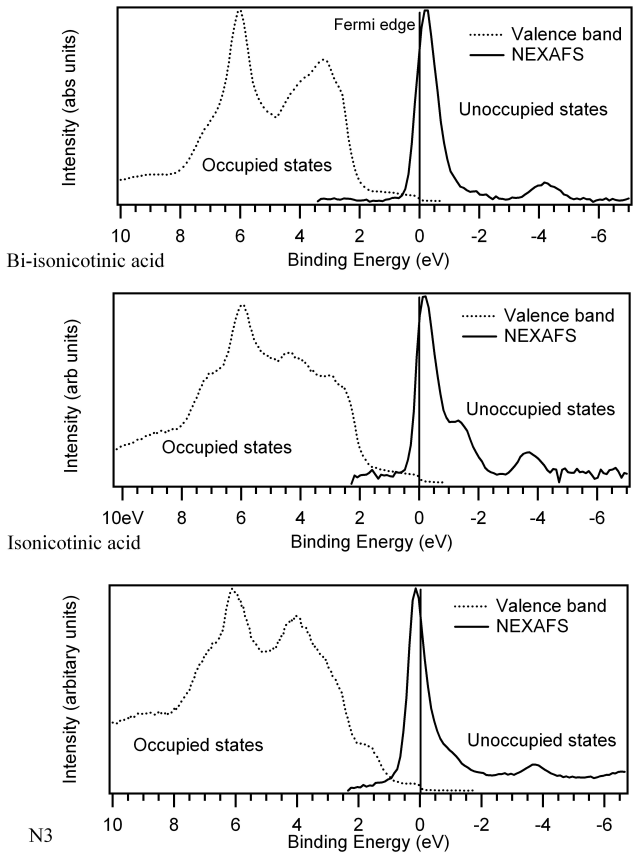

FIGURE 5.6: Energy level alignment of the substrate valence band and the unoccupied molecular orbitals of the molecule for bi-isonicotinic acid (top), isonicotinic acid (middle) and N3 (bottom).

of the core-hole can lead to the LUMO state being excitonically pulled down so that it crosses the Fermi level of the gold surface.[67] We can measure the position of the core-excited LUMO, with respect to the Fermi level, by placing the calibrated N 1s XAS and valence-band photoemission for each monolayer on a common binding energy scale,[79] as in figure 5.6. The data show that the LUMO of all the molecules lie mostly below the Fermi level of the Au(111) surface in the core-excited state. This would, theoretically, allow the transfer of electrons from the valence band of the metal to the majority of the vibrational states of the core-excited LUMO that now lie below the Fermi level of the gold surface.

The lack of the distinctive Auger feature in the N3 RPES monolayer suggests that

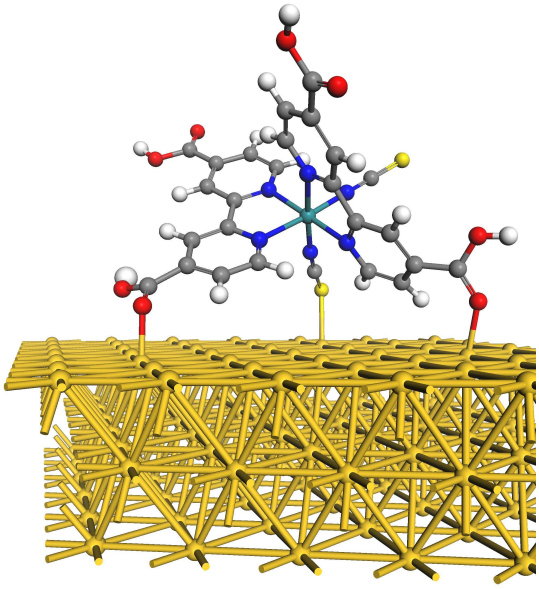

FIGURE 5.7: Molecular model of a possible configuration of the N3 molecule on the Au(111) surface. Even though in this case the bi-isonicotinic acid ligands are in contact with the surface, the octahedral geometry of the molecule prevents them from lying flat on the surface in any orientation.

there is no charge transfer from the surface to the molecule which seems, at first, to be a bit puzzling: bi-isonicotinic acid, which is one of the ligands of N3, and the related isonicotinic acid, as well as nicotinic and picolinic acid (see Chapter 6) have been shown to have charge transfer to the molecule from the gold surface. This is especially surprising as the LUMO of the molecule has been shown to energetically overlap with the Fermi edge of the gold metal (see figure 5.6) in the core-excited state. Nonetheless, the N3 molecule bonds to the gold surface mostly through the sulphur atoms,[24] but even with some potential bonding through the bi-isonicotinic acid ligands, the largely octahedral geometry of the molecule prevents the bi-isonicotinic acid ligands from lying flat on the surface, as illustrated in figure 5.7. This means that the π-orbitals of the pyridine rings of these ligands have little or no spatial overlap with the dangling $5d$ orbitals of the gold surface. This is important as density functional theory (DFT) calculations show that the LUMO is predominantly derived from the π-orbitals of the pyridine rings.[6] This means that electrons cannot tunnel easily from the surface

to the LUMO of the molecule. Charge transfer can occur for bi-isonicotinic acid on gold because the molecule lies flat on the surface allowing for the overlap between the orbitals and, therefore, there can be a high degree of spatial overlap between the π-orbitals and the dangling $5d$ orbitals of the gold surface. Consequently, charge transfer can take place from the surface to the molecule.

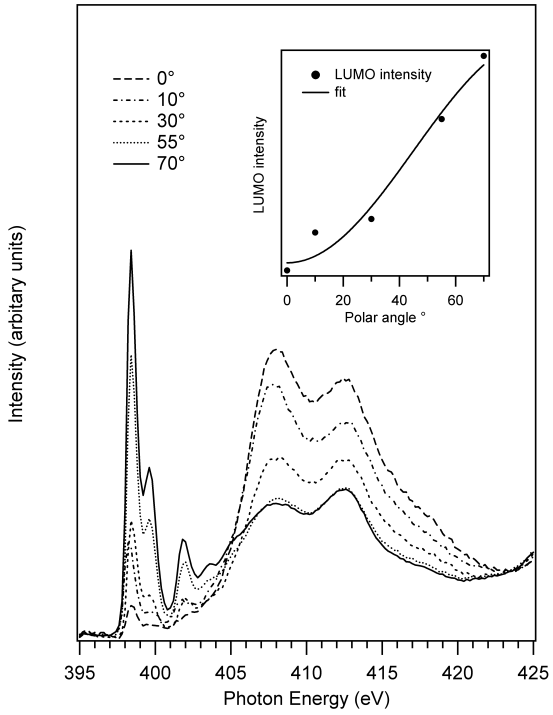

FIGURE 5.8: Angle-resolved XAS spectra for a monolayer of isonicotinic acid adsorbed on the Au(111) surface. The inset shows the variation of the LUMO intensity with the angle of the incident radiation to the surface normal. The fitted curve is the theoretical angular dependence for an aromatic ring with tilt angle of 89 ± 10^0 to the surface normal, assuming a random azimuthal orientation and linear light polarization (see refs [61] and [63]).

The adsorption geometry of the isonicotinic acid molecules on Au(111) surface have been studied using angle-resolved XAS. The data in figure 5.8 show the spectra over the N 1s edge for a range of angles. The spectra have been corrected for undulator intensity variations and normalized to the continuum of states above the vacuum level (425 eV).[8] The angles quoted are those between the surface normal and the electric

field vector of the incoming radiation. Due to the 6-fold rotational symmetry of the molecule, variations in the azimuthal intensity can be ignored, allowing us to focus on the polar angles.[61] The sharp low energy peaks below 406 eV are identified with the π^* unoccupied molecular orbitals, associated with the planar aromatic ring of the molecule.[85] The π^* intensity is highest when the electric field is perpendicular to the plane of the surface, with minimal intensity for the field oriented in the parallel direction. An analysis of the LUMO intensity variation, as a function of angle,[61, 63] reveals that the plane of the aromatic ring structure has an average tilt angle of 89 ± 10^0 to the surface normal. Isonicotinic acid, therefore, adsorbs parallel to the metal surface which maximizes the electronic coupling, allowing charge transfer from the surface to the molecule, as discussed in the case of biisonicotinic acid.

5.3.2 Charge transfer from the molecule to the gold

The absence of the charge-transfer Auger-decay features on the N3 monolayer RPES would imply that there is no charge transfer from the metal to the N3 molecule, unlike the bi-isonicotinic acid and isonicotinic acid molecules. We can get a measure of the charge transfer dynamics in the other direction, from the molecule to the gold surface, by using the *core-hole clock* implementation of RPES. An integration of the participator intensity over the HOMO and HOMO-1 of the bi-isonicotinic acid (1-7 eV) as a function of photon energy is shown for both the multilayer and monolayer in figure 5.9, and compared to the associated x-ray absorption spectrum (normalized to the intensity of the LUMO+1). This was also carried out for the isonicotinic acid and N3 dye molecules, as shown in figure 5.10 and figure 5.11 respectively. A large proportion of participator electrons are expected in the case of the multilayer because the molecules are effectively isolated from the substrate which means that no charge transfer can take place. Electrons excited to the LUMO, LUMO+1 and LUMO+2, therefore, remain on the molecule long enough to participate in the core-hole decay, leading to a final state identical to direct photoemission of the HOMO state involved (figure 5.3b). In fact, the multilayer is taken as the benchmark in the core-hole clock analysis to determine the anticipated participator intensity for each LUMO state in

the absence of charge transfer.[9, 6, 62]

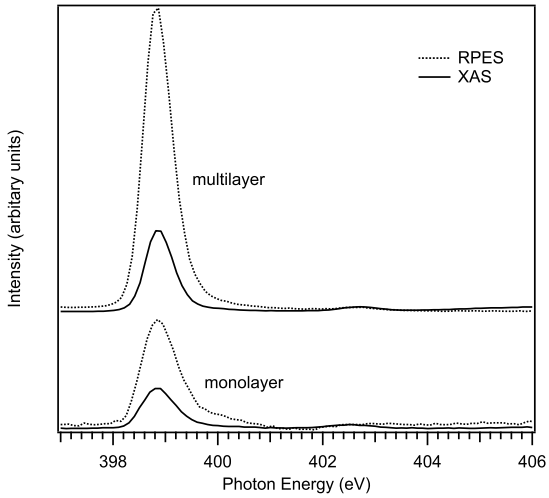

FIGURE 5.9: N 1s RPES and N 1s XAS spectra of the bi-isonicotinic acid multilayer and monolayer on Au(111). The RPES spectra shown here are binding energy integrations from 1 to 7 eV for the datasets shown in figure 5.2. The spectra have been normalised to the LUMO+1 at 402.5 eV.

Unfortunately, in this case, the core-hole clock analysis used for molecules adsorbed on semiconductor surfaces,[6, 9] such as TiO_2, is unsuited to give us an exact quantitative figure for the transfer time of either bi-isonicotinic acid, isonicotinic acid or the N3 dye molecule adsorbed onto a metal surface, such as gold. As is seen in Chapter 4 for C_{60}, the LUMO of all the molecules in the core-excited state, lies both above and below the Fermi level of the gold substrate. Charge transfer can occur from the LUMO states above the Fermi level to the substrate, rendering normalization to the LUMO quantitatively unreliable. Yet an upper limit for the charge transfer time, from the LUMO to the gold surface, can be obtained by assuming that there is no charge transfer from the LUMO+1 to the surface. This allows for normalization to the LUMO+1, as used in figures 5.9-5.11. It has already been shown that there is no charge transfer from the surface to the N3 molecule so the decrease in the LUMO intensity is purely due to charge transfer from the LUMO to the gold surface in the case of the N3 dye molecule. Denoting the intensity of the LUMO as I, the average electron injection time, τ_{El}, for electrons moving from the LUMO to unoccupied

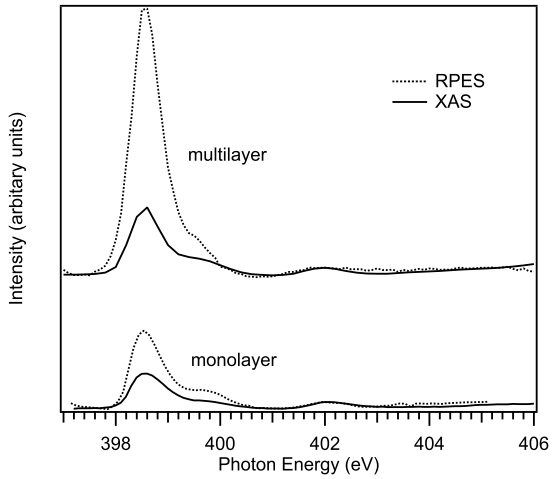

FIGURE 5.10: N 1s RPES and N 1s XAS spectra of the isonicotinic acid multilayer and monolayer on Au(111). The RPES spectra shown here are binding energy integrations from 1 to 7 eV for the datasets shown in figure 5.4. The spectra have been normalised to the LUMO+1 at 402.5 eV.

substrate states is determined from equation 7.2:

$$\tau_{El} = \tau_{CH} \frac{I^{mono}_{RPES}/I^{mono}_{XAS}}{I^{multi}_{RPES}/I^{multi}_{XAS} - I^{mono}_{RPES}/I^{mono}_{XAS}} \tag{5.1}$$

A more thorough discussion of the corehole clock implementation of RPES and a derivation of the equation is given in chapter 3. I^{mono}_{RPES} and I^{multi}_{RPES} represent the intensities of the LUMO peaks in the RPES monolayer and multilayer respectively. They are normalised by the XAS intensities, I^{mono}_{XAS} and I^{multi}_{XAS}. τ_{CH} is the average lifetime of an N 1s core-hole that has been measured to be 6 fs.[86] For the N3 on gold core-hole clock analysis, $I^{mono}_{RPES}/I^{mono}_{XAS} = 0.69$ and $I^{multi}_{RPES}/I^{multi}_{XAS} = 1.64$, giving an overall upper limit for the charge injection time of 4.4 fs from the LUMO to the conduction band of the surface. The LUMO for both the monolayers of bi-isonicotinic acid and isonicotinic acid on gold are not unoccupied due to charge transfer from the surface and, consequently, increase the size of the LUMO participator intensity in the RPES spectra. As normalization to the LUMO peak is no longer reliable, a quantitative analysis for either of these molecules is impossible, but the decrease of the LUMO peak in the integrated RPES spectra of the monolayer - with respect to

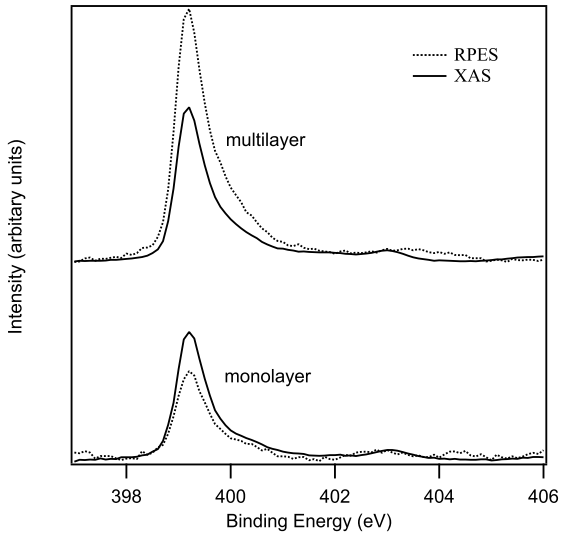

FIGURE 5.11: N 1*s* RPES and N 1*s* XAS spectra of the N3 multilayer and monolayer on Au(111). The RPES spectra shown here are binding energy integrations from 1 to 7 eV for the datasets shown in figure 5.5. The spectra have been normalised to the LUMO+1 at 402.5 eV.

the multilayer spectra - qualitatively suggests that there is significant charge transfer from the LUMO to the unoccupied surface states.

5.4 Conclusion

The RPES spectra of an N3 monolayer on gold do not exhibit the *superspectator* features observed for the monolayer RPES spectra of other molecules such as bi-isonicotinic acid, isonicotinic acid and C_{60}. This is surprising as bi-isonicotinic acid is a ligand of N3 and would, thus, be expected to share similar characteristics. These features are due to the Auger decay of an electron from the LUMO being spectated by an electron transferred from the surface to the molecule. The lack of such a decay channel in N3 suggests that there is almost no charge transfer from the gold surface into the N3 molecule. By combining the placing of XAS and the valence-band photoemission on a common binding energy scale, the LUMO of the N3 molecule is revealed to lie partially below the Fermi edge of the gold metal, showing that it is energetically possible for charge transfer to occur in the core-excited state. The

reason for the lack of charge transfer from the gold surface to the N3 molecules may be attributable to the geometry of the molecule on the surface as the π-orbitals of the aromatic rings on the bi-isonicotinic acid ligands (which have been shown to contain the LUMO orbitals) lack the required spatial overlap with the $5d$ orbitals of the gold surface. This significantly reduces the chances of an electron tunnelling from the surface to the molecule. On the other hand, charge transfer *from* the LUMO of the molecule does occur for all three molecules to the gold surface. In the case of N3 , the core-hole clock implementation of RPES provides an upper limit on charge transfer from the LUMO to the surface of 4.4 fs.

Chapter 6

Charge Transfer Processes of Nicotinic and Picolinic acid on Au(111)

6.1 Introduction

Nicotinic acid, picolinic acid and isonicotinic acid are all isomers of pyridine carboxylic acid, with the carboxyl side group being at different positions on the pyridine for each molecule. This can be seen in figure 6.1. Isonicotinic acid on gold was previously discussed in Chapter 5. In this chapter, we will turn our attention to picolinic and nicotinic acid. Both of these molecules are found commonly in the human body and are considered vital to certain bodily functions. Picolinic acid is believed to form a complex with zinc to allow the passage of zinc through the gastrointestinal wall to be circulated around the body.[87] Nicotinic acid is more commonly known as niacin or vitamin B3, and is an essential human nutrient. It has a variety of functions, such as acting as a precursor to NAD+/NADH and NADP+/NADPH, which play essential metabolic roles in living cells, as well as DNA repair and the production of steroid hormones.[88] A deficiency of nicotinic acid leads to the disease, pellagra.[88]

Nonetheless, we are studying these molecules due to their similarity to isonicotinic acid. N3, bi-isonicotinic acid and isonicotinic acid adsorbed onto a gold (111) surface are studied in Chapter 5. For the bi-isonicotinic acid and isonicotinic acid monolayers, we observed features on the RPES spectra, which we called *superspectator decay*. These were deduced to be due to *spectator decay* of a corehole in the presence of a

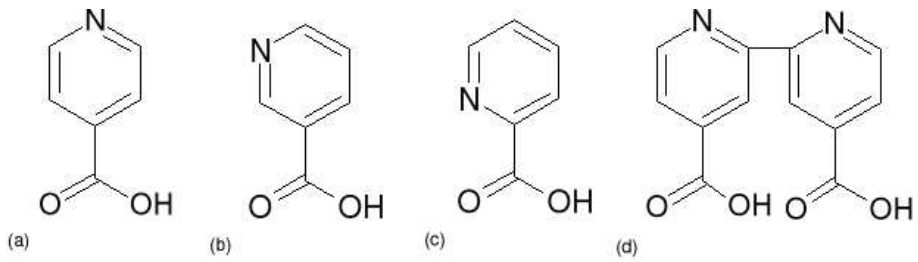

FIGURE 6.1: Schematic diagram of isonicotinic acid (a), nicotinic acid (b), picolinic acid (c) and bi-isonicotinic acid (d). Isonicotinic acid and bi-isonicotinic acid are discussed in Chapter 5 and are shown here for comparison of the molecular structure with nicotinic and picolinic acid.

charge transferred electron from the gold surface. These features were not observed for the N3 dye molecule, indicating a lack of charge transfer. The purpose of this experiment was to see whether the *superspectator* features, observed for bi-isonicotinic acid, can also be seen for nicotinic and picolinic acid.

6.2 Method

Experiments were carried out at beamline I311 of the Swedish synchrotron facility MAX-lab in Lund. The beamline has a photon energy range of 30-1500 eV and is equipped with a Scienta SES200 hemispherical electron analyzer.[64] The radiation has a high degree of elliptical polarization and may be considered as linearly polarized for the purposes of this study. The base pressure in the analysis chamber was in the mid 10^{-11} mbar range and, in the preparation chamber, it was in the low 10^{-10} mbar range.

The substrate was a single crystal of dimensions 10 mm diameter $\times$ 2.5 mm. It was mounted on a loop of tungsten wire (0.5 mm) that passed tightly through the body of the crystal, ensuring a good electrical and thermal contact. A thermocouple was attached within the body of the crystal in order to accurately monitor the temperature. The crystal was cleaned along the lines of Barth *et al.*[77] by cycles of sputtering using 1 kV Ar ions and then annealing at 900 K by passing a current through the tungsten wire mount. Surface contamination was checked by monitoring

the C 1s, K 2p and S 2p core-level photoemission peaks.

For the deposition of both nicotinic and picolinic acid, the molecules were evaporated from a Knudsen cell type evaporator at a temperature of $\sim$ 110 °C onto the sample held at room temperature at a distance of $\sim$ 20 cm. This was similar to the setup for isonicotinic acid on Au(111), as is described in Chapter 5. Coverage was measured using the intensities of the core-level photoemission peaks and the molecule contribution to the shape of the valence-band photoemission spectra.

The monochromator exit slits of the beamline were set to give a resolution $\sim$ 50 meV for photons of energy $h\nu = 340$ eV. The photon energy was calibrated from the separation between the Au 4f peaks measured with 1^{st} and 2^{nd} order radiation. For measuring x-ray absorption and resonant photoemission spectra, a taper was applied to the undulator to reduce the intensity variation of the radiation as the photon energy was scanned. For XAS and RPES measurements, the analyzer pass energy and entrance slits were set to give a resolution of $\sim$ 500 meV with respect to binding energy. The analyzer was also set to record spectra in fixed mode for these measurements to give the best compromise between energy resolution and the number of counts required for 2D RPES spectra. As both molecules suffer beam damage under irradiation by soft x-rays, RPES measurements were taken as the beam was scanned across the sample at a rate of $1.25 \mu m s^{-1}$. For core level spectra, the analyzer was set to record in swept mode with an electron resolution of $\sim$ 100 meV.

6.3 Results and Discussion

The resonant photoemission spectra for the nicotinic acid monolayer (both the autoscaled intensity and rescaled intensity versions) and multilayer on Au (111) are shown in figure 6.2. The RPES spectra for the picolinic acid monolayer (including autoscaled and rescaled intensity versions) and multilayer on Au (111) are shown in figure 6.3. The same type of spectra were also measured for the clean Au(111) surface. As before, the two dimensional RPES datasets were obtained by measuring the valence-band photoemission up to 16 eV binding energy for the range of photon energies covering the N 1s absorption edge in 0.1 eV steps.

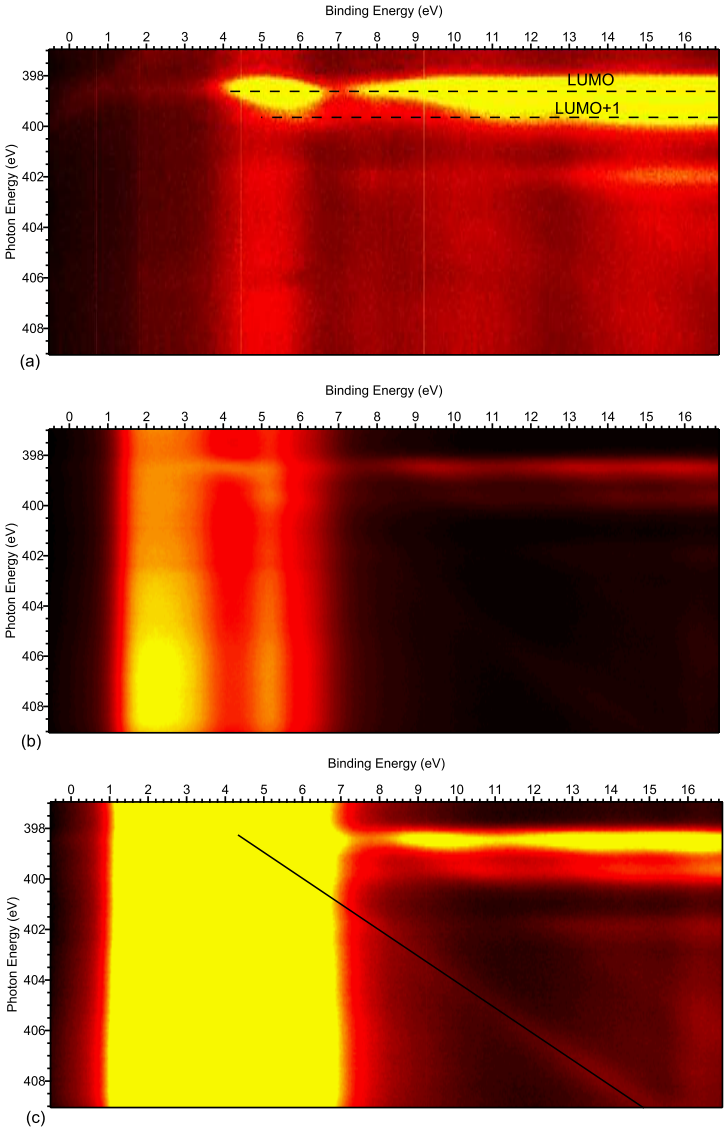

FIGURE 6.2: Resonant Photoemission for (a) a multilayer of nicotinic acid on gold, (b) a monolayer of nicotinic acid on gold and (c) the same monolayer spectra as shown in (b), but with the intensity rescaled to show the diagonal Auger features more clearly.

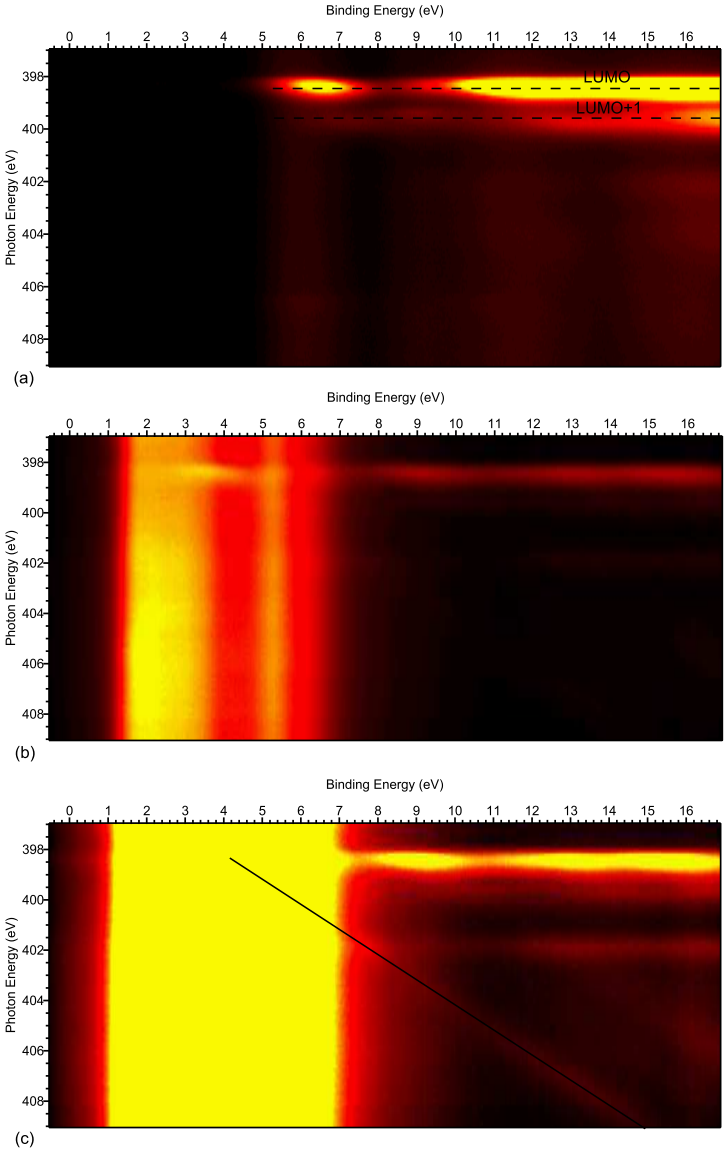

FIGURE 6.3: Resonant Photoemission for (a) a multilayer of picolinic acid on gold, (b) a monolayer of picolinic acid on gold and (c) the same monolayer spectra as shown in (b), but with the intensity rescaled to show the diagonal Auger features more clearly.

The RPES spectra for the picolinic and nicotinic acid multilayers are very similar to the RPES spectra for the isonicotinic and bi-isonicotinic acid multilayers from Chapter 5. We observe the same *participator decay* and *spectator decay* features from Chapter 5. For both the monolayer of nicotinic and picolinic acid, we observe an extra diagonal feature, highlighted by a solid black line, which tracks back to the LUMO participator peak, although it is hidden at low binding energy due to the gold photoemission peaks. This feature was not observed on the multilayer spectra for either molecule. Furthermore, it was also found in the RPES spectra for the isonicotinic and bi-isonicotinic acid monolayers, where we determined that its occurrence was due to charge transfer from the surface to the molecule. Hence, this implies that there is charge transfer from the gold to the molecule in the case of both picolinic and nicotinic acid.

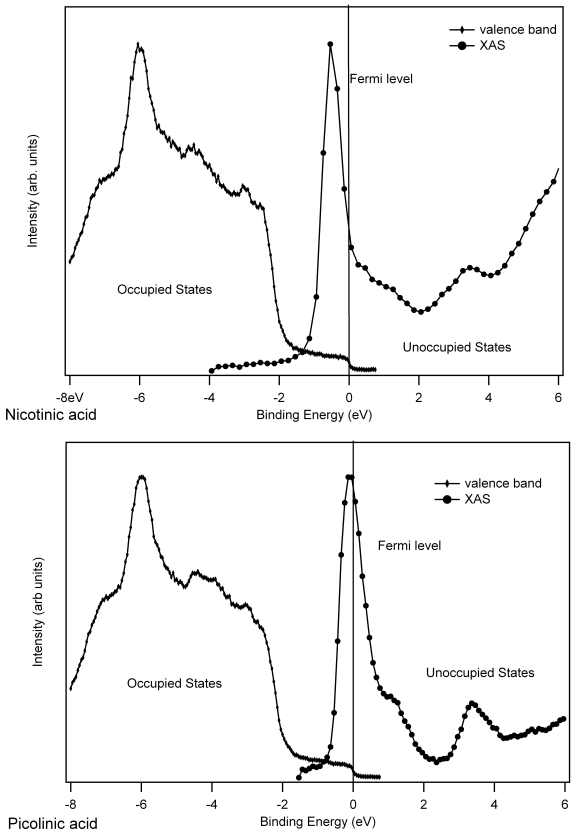

FIGURE 6.4: Energy level alignment of the substrate valence band and the unoccupied molecular orbitals for nicotinic acid (top) and picolinic acid (bottom).

We can determine whether it is energetically possible for charge transfer to occur by measuring the position of the core-excited LUMO with respect to the Fermi level. If there are unoccupied levels of the molecule below the Fermi level of the metal surface, then charge transfer can occur into those levels. By placing the valence-band spectra and the calibrated N 1s XAS spectra for the monolayer on a common binding energy scale,[79] we can determine the position of the LUMO with respect to the Fermi level, as shown in figure 6.4, for both picolinic acid and nicotinic acid. It is clear to see that the LUMO of both the picolinic and nicotinic acid lies partly below the Fermi level of the gold (111) surface, meaning that charge transfer is energetically possible. This energy alignment was similar to the result for bi-isonicotinic and isonicotinic acid which is in Chapter 5.

The energetics are, consequently, favorable for electron transition. The next question is whether there is any spatial overlap between the LUMO of the molecule and the gold surface orbitals. We can determine the likelihood of spatial overlap by measuring the adsorption geometry of the molecules on the Au(111) surface using angle-resolved XAS. The data in figure 6.5 shows the spectra over the N 1s edge for a variety of angles in the case of nicotinic acid. Similarly, figure 6.6 shows the spectra of picolinic acid for a variety of angles. The spectra have been corrected for undulator intensity variations and normalized to the continuum of states above the vacuum level (425 eV for picolinic acid and 422 eV for nicotinic acid).[8] For both these molecules, we assume an average random azimuthal orientation of the molecules adsorbed onto the surface. Therefore, we will only consider the contribution of the polar angles, i.e. the angle between the surface and the molecule. The sharp low energy peaks below 406 eV are identified with the π^* unoccupied molecular orbitals, associated with the planar aromatic ring of the molecule.[85] The intensity for the π^* intensity is highest when the electric field is perpendicular to the plane of the surface, with minimal intensity for the field oriented in the parallel direction. The variation of LUMO intensity with angle for the picolinic acid acid reveals a tilt of 89.5 ± 10^o. For the nicotinic acid, however, we can see from the graph on figure 6.5 that two of the results, the 80^o and 90^o angles, seem to lie away from the fit. The reason for this is unclear. If we fit a curve for this graph, we obtain an angle of tilt of 98 ± 10^o between the surface and

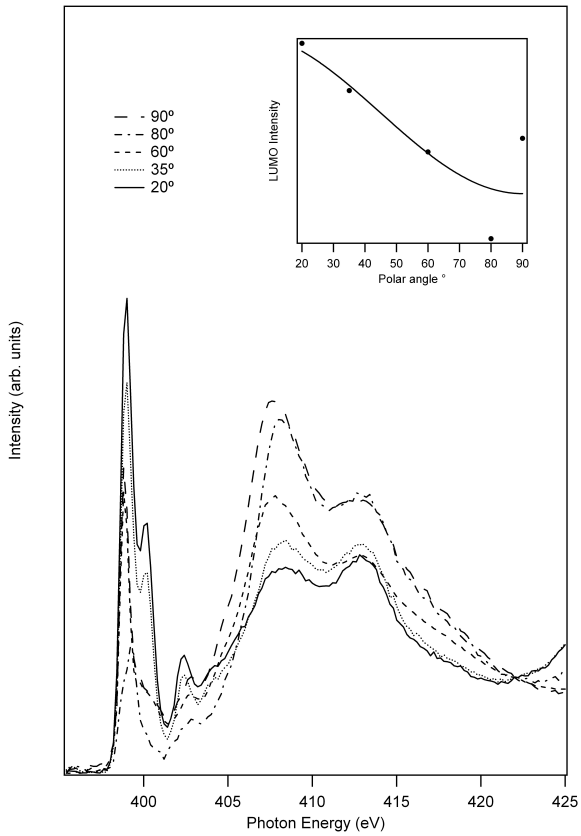

FIGURE 6.5: Angle-resolved XAS spectra for a monolayer of nicotinic acid adsorbed on the Au(111) surface. The inset shows the variation of the LUMO intensity with the angle of the incident radiation to the surface normal. The black line represents the fitted curve.[61]

the molecule. The anomalies lead us to some reservations about the result.

Both of the molecules seem to lie flat on the surface, which would allow for spatial overlap between the π^* orbitals, which make up the LUMO for both molecules, with the $5d$ orbitals of the Au (111) surface. This is similar to the result found for isonicotinic acid, as described in Chapter 5, and for bi-isonicotinic acid found in previous experiments.[24]

Combined with our knowledge of the adsorption geometry and energy level alignment for both nicotinic and picolinic acid on Au (111), it is reasonable to assume that the *superspectator* feature, found on the monolayer for both molecules, is due to charge transfer of an electron from the surface to the molecule. This was expected as

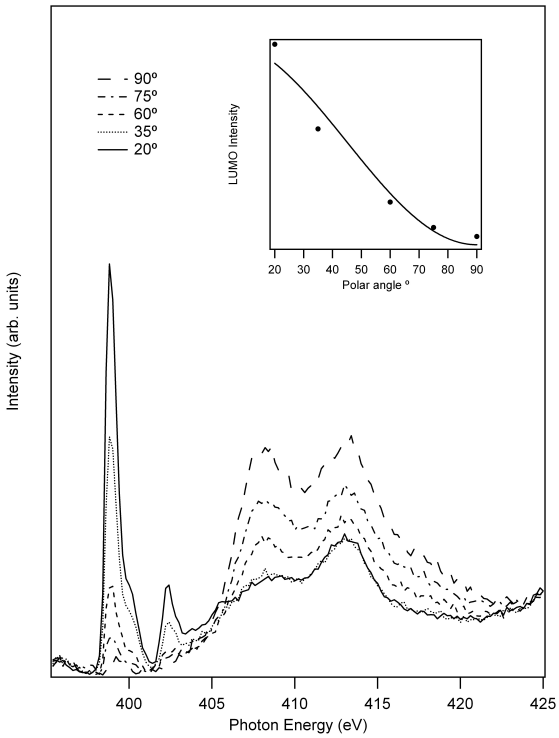

FIGURE 6.6: Angle-resolved XAS spectra for a monolayer of picolinic acid adsorbed on the Au(111) surface. The inset shows the variation of the LUMO intensity with the angle of the incident radiation to the surface normal. The black line represents the fitted curve.[61]

the molecules are very similar to isonicotinic and bi-isonicotinic acid. This still brings up the important question of whether the charge transfer occurred in the ground state or the excited state of the molecule.

An indication of the timescale of the charge transfer from the surface to the molecule can be gained from looking at charge transfer in the reverse direction: from the LUMO+1 of the molecule to the surface. As is shown in chapters 4 and 5 this can be done using core-hole clock analysis. Figure 6.7 and figure 6.8 show the integrated participator intensity and x-ray absorption spectra for the multilayer and monolayer of nicotinic and picolinic acid respectively. As was mentioned in previous chapters, as the LUMO lies above and below the Fermi level, charge transfer can occur from LUMO states above the Fermi level to the surface, meaning we cannot normalise to the LUMO. By assuming that there is no charge transfer from the LUMO+1 to the

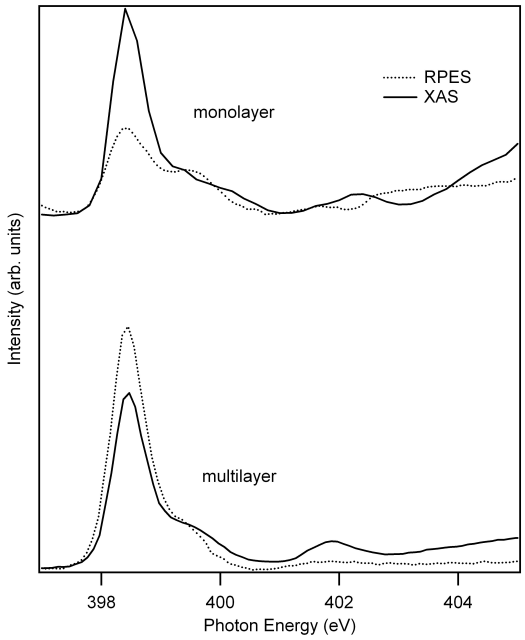

FIGURE 6.7: N 1*s* RPES and N 1*s* XAS spectra of the nicotinic acid multilayer and monolayer on Au(111). The RPES spectra shown here are binding energy integrations from 4 to7 eV for the datasets shown in figure 6.2. The spectra have been normalised to the LUMO+1 at 399.5 eV

surface, normalisation to the LUMO+1, as in figures 6.7 and 6.8, can give us an indication of charge transfer from the LUMO to the surface. As we already know, though, charge transfer does occur to the surface for these molecules, so no quantitative analysis is possible. We can note, however, that the decrease in the LUMO peak for the monolayer integrated RPES spectra, with respect to the multilayer spectra, for the picolinic acid and nicotinic acid, suggests qualitatively that there is significant charge transfer from the LUMO to the unoccupied surface states. We would expect charge transfer from the molecule to the surface to be easier than in the reverse direction, due to the large number of k-states of the surface into which the charge is transferred. Thus, we can conclude that it is most probable that the charge transfer occurs in the ground state before any excitation.

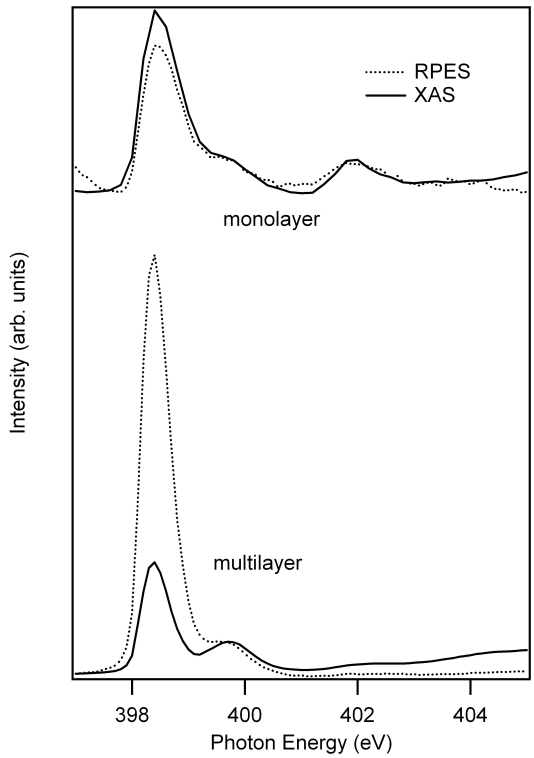

FIGURE 6.8: N 1*s* RPES and N 1*s* XAS spectra of the nicotinic acid multilayer and monolayer on Au(111). The RPES spectra shown here are binding energy integrations from 4 to7 eV for the datasets shown in figure 6.3 The spectra have been normalised to the LUMO+1 at 399.7 eV.

6.4 Conclusion

The RPES monolayer spectra for both the picolinic and nicotinic acid on Au(111) shows the distinctive *superspectator* feature previously observed for bi-isonicotinic acid, isonicotinic acid and C_{60} on Au(111), as is described in chapters 4 and 5. As was found for the previous molecules, it is reasonable to conclude that this feature occurs due to *spectator* decay in the presence of a charge-transferred electron from the Au(111) surface.

Using combined valence band and calibrated x-ray absorption spectra, we have been able to produce energy alignments for both molecules that prove that charge transfer is energetically favourable. Angle-resolved XAS has also shown that both molecules lie flat on the surface, which would allow for spatial overlap between the π^*

orbitals that LUMO of the molecule lies on with the $5d$ surface orbitals of the gold. All this lends extra weight to the conclusion that charge transfer from the surface to the molecule occurs. It is also highly probable that this occurs in the ground state rather than in the core-excited state.

Chapter 7

Studying Charge Transfer Processes using RIXS

7.1 Introduction

Studying charge transfer times is very important to understanding DSSCs. Advances in pump probe lasers have allowed us to study processes which occur on a similar timescale to ultrafast charge transfer;[89, 90] however, unlike in photoemission spectroscopy, the core-hole and excited electron are not initially localised on the same atom.[91] Photoemission spectroscopy provides a more accurate representation of the charge transfer processes that occur in DSSCs.[91] As is mentioned in Chapter 3, core-hole clock analysis has been used to determine electron transfer both from dye molecules and ligands[9, 6] to TiO_2 surfaces.

In figure 7.1b, we show the various core-hole decay channels that can occur for RPES, such as *participator decay* and *spectator decay*, which are described fully in previous chapters. The core-hole clock technique could theoretically be used in resonant inelastic x-ray scattering (RIXS), where it is the x-rays emitted due to core-hole decay that are studied. This is in contrast to resonant photoemission, where it is the electrons which are emitted from the sample due to decay caused by incident x-rays producing coreholes.

Resonant inelastic x-ray scattering is mainly used for studying bulk samples, but it has been used to study adsorbates on a variety of surfaces.[68, 92, 93] The reason

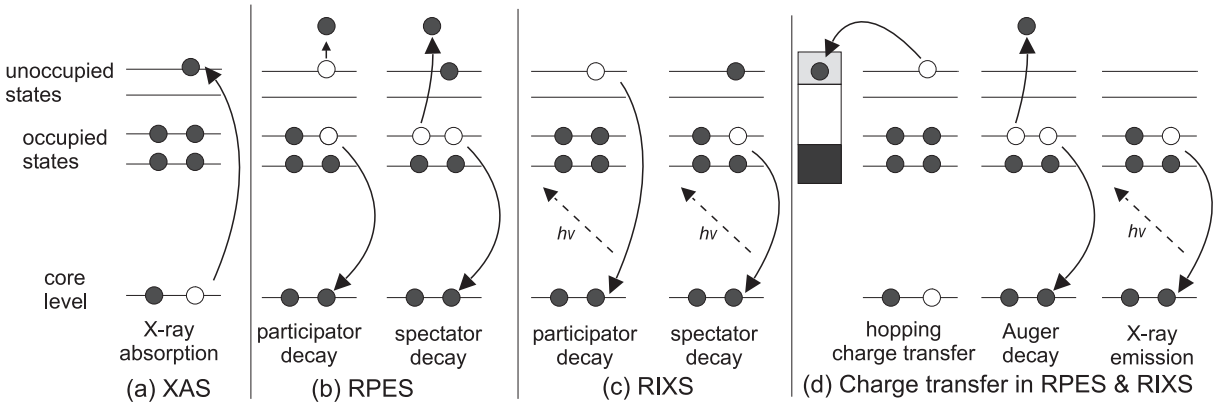

FIGURE 7.1: Schematic representation of the techniques used in this comparative study of charge transfer dynamics via RPES and RIXS core-hole decay channels: (a) the core-excitation of an N1s electron to an unoccupied molecular orbital, (centre) participator and spectator decay channels for both; (b) the non-radiative RPES and (c) radiative RIXS processes requiring the localisation of the core-excited electron on the timescale of the core-hole lifetime, and (d) the decay channels available in RPES and RIXS if the core-electron hops into the substrate conduction band on the timescale of the core-hole lifetime.

for using RIXS in these examples was to study the valence band of an adsorbate atom which otherwise could not have been separated from the substrate valence band had resonant photoemission been used.[70] Nevertheless, no previous studies have, to our knowledge, studied charge transfer between the adsorbates and the surfaces using a core-hole implementation for RIXS. We would suggest that it should be possible to adapt the core-hole clock method, used only previously in resonant photoemission, to RIXS so as to measure the charge transfer between an adsorbate and a semiconductor surface. The key to this is the elastic peaks of the RIXS spectra. The elastic peak is caused by the incoming x-rays promoting an electron and the electron dropping right back into the core-hole it made thus emitting an x-ray of the same energy as the incoming x-rays. Any removal of the promoted electrons via charge transfer, as seen in figure 7.1, would lead to a reduction in the size of the elastic peak. This can be measured and used, as we show later, to measure the charge transfer between the molecule and the surface.

In order to test this adaptation of the core-hole technique, we have studied bi-

isonicotinic acid adsorbed onto TiO_2 using RIXS. This has been previously studied by Schnadt *et al.* using resonant photoemission spectroscopy and this has also been analysed previously by them using the core-hole clock technique.[9] Other photoemission studies have shown that N3 bonds to TiO_2 surface via deprotonation of the carboxylic acid groups in the bi-isonicotinic acid ligands forming a 2-M bidentate bond.[6, 8] The chemical coupling allows for a charge transfer of excited electrons from the LUMO of the molecule to the conduction band of the TiO_2. The LUMO of the N3 molecule lies on the bi-isonicotinic acid ligand.[94] The previous photoemission spectroscopy experiment of bi-isonicotinic acid on TiO_2 showed ultrafast charge transfer from the molecule to the substrate with an upper limit of 3 femtoseconds. Obtaining a similar result with x-ray emission spectroscopy would provide extra validation of the technique and would give us confidence for using it in other systems.

7.2 Method

Experiments were carried out at beamline I511-3 of the Swedish synchrotron facility MAX-lab in Lund. The beamline has a photon energy range of 30-1500 eV and is equipped with a Scienta XES-350 x-ray emission spectrometer.[65] The radiation has a high degree of elliptical polarization and may be considered as being linearly polarized for the purposes of this study. The base pressure, in the analysis chamber, was in the mid 10^{-9} mbar range and, in the preparation chamber, it was in the low 10^{-8} mbar range.

The substrate was a single crystal of rutile $TiO_2(110)$ of dimensions 10 mm x 10 mm x 2 mm. The substrate was mounted onto a 25 mm diameter circular copper sample plate by soldering tantalum wire across the top and bottom of the sample. This ensured a good electrical and thermal contact with the sample holder. The crystal was cleaned by cycles of sputtering using 1 kV Ar^+ ions and then annealing at 800 K by passing a current through a tungsten filament behind the copper sample holder.

For the deposition of the bi-isonicotinic acid, the molecules were evaporated from a Knudsen cell type evaporator at a temperature of $\sim$ 230 °C onto the sample held

at room temperature sample and a distance of ~ 15 cm to obtain a multilayers with a thickness of 25 ± 5 monolayers. The coverage was estimated from the x-ray photon emission count rate (normalised to the incoming photon flux rate) compared to the monolayer. To obtain a monolayer, the sample was held at a temperature of 200°C for the duration of the deposition, allowing the physisorbed multilayers to desorb and leaving the chemisorbed monolayer.

The monochromator exit slits of the beamline were set to give a resolution ~ 100 meV for photons of energy $h\nu = 400$ eV. The photon energy was calibrated from the elastic peaks for the LUMO and LUMO+1 photon energies, which were determined by fluorescence yield x-ray absorption spectroscopy (XAS). The angle of the sample to the incoming radiation was 70^0 from normal incidence. This grazing incidence is more surface sensitive allowing for greater intensity of the RIXS for the monolayer and multilayer. The beam was scanned vertically across the sample, at a rate of 0.05 mm per minute, whilst the various RIXS spectra were taken. This minimised the amount of beam damage to the molecule on the surface by reducing the exposure time of each part of the sample to less than a minute. The rate was determined by measuring sequential x-ray absorption spectra at decreasing time intervals in fresh spots of the sample until no change in the spectra was observed.

7.3 Results and Discussion

XAS spectra for the multilayer and monolayer of bi-isonicotinic acid on TiO_2 can be seen in figure 7.2. The photon energy of the LUMO peak for the multilayer was found to be 399.2 eV and the energies for the LUMO+1 and LUMO+2 peaks for the multilayer were found to be 400.3 eV and 403.1 eV respectively. For the monolayer, the peak for the LUMO was found to be 399 eV; the LUMO+1 peak was found at 400.7 eV and the LUMO+2 peak was at 402.9 eV. The monolayer peaks were obviously not as well defined due to the lower number of molecules. The fluorescence XAS spectra were used to determine the photon energies to be used in the RIXS spectra. These spectra are very similar to previous studies.[9, 8]

The RIXS spectra for the LUMO photon energy of the multilayer of bi-isonicotinic

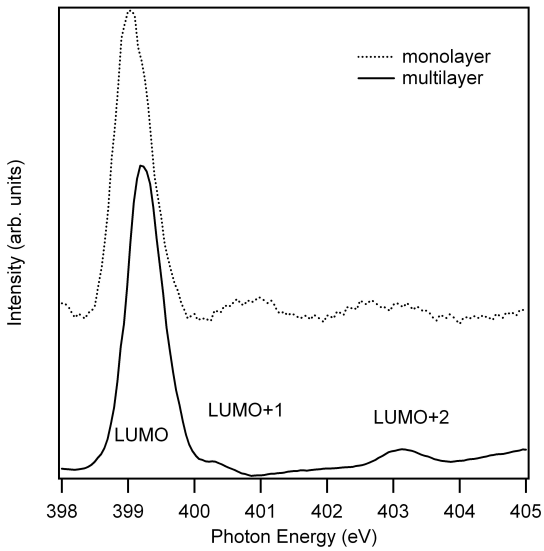

FIGURE 7.2: X-ray absorption spectrum for a multilayer of bi-isonicotinic acid on TiO_2 and a monolayer of bi-isonicotinic acid on TiO_2. The background spectra have been removed and the spectra were normalised to their respective LUMO peaks.

acid on TiO_2 at 399.2 eV and the monolayer of bi-isonicotinic acid at 399 eV are show in figure 7.4. The RIXS spectra for the LUMO+1 photon energy of the multilayer at 400.3 eV and LUMO+1 of the monolayer at 400.7 eV are shown in figure 7.5. The elastic peaks can be very clearly observed for the multilayer spectra at the LUMO and LUMO+1 energies. The elastic peaks are caused by participator decay as seen in figure 7.1c. Lower energy peaks are the result of inelastic x-ray scattering and represent spectator decay from each HOMO (highest occupied molecular orbitals), as seen in figure 7.1c. This gives us a picture of the HOMO levels similar to valence band spectra in photoemission spectroscopy but only showing those orbitals that spatially overlap with the nitrogen atom, representing the partial density of states for the nitrogen. The difference between the photoemission and RIXS spectra is illustrated in figure 7.3. The combination of these peaks produces a very good fit to the spectrum and the distinctiveness of each peak in the multilayer spectrum allows for a high degree of confidence in the resulting fit in both the LUMO and LUMO+1 multilayer spectra, especially for energies close to the elastic peak. Fitting the spectra to a series of Gaussian-Lorentzian peaks is done primarily to reduce the uncertainty

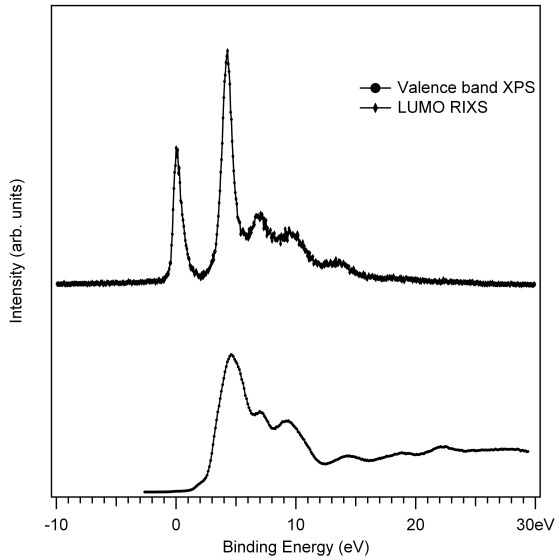

FIGURE 7.3: Comparison of valence band structure for a bi-isonicotinic acid multilayer studied by photoemission spectroscopy (bottom) and resonant inelastic x-ray scattering (top). The RIXS spectra was taken at the LUMO photon energy and was calibrated for a binding energy scale by defining the elastic peak as 0 eV binding energy. The valence band photoemission spectrum was taken at a photon energy of 110 eV.

in determining the relative intensities of the elastic peaks that are not only key to the subsequent analysis, but also essential to decompose the spectrum into the respective nitrogen-derived valence states for future studies.

Strict limitations are used for making the eventual fit for the monolayer spectra. The fitted peaks for both monolayer and multilayer spectra are Voigt functions which are a convolution of Gaussian and Lorentzian functions. The energies of the peaks in the monolayer spectra were kept very similar to the multilayer spectra, allowing only for a shift in energy of less than 0.5 eV. Also the Lorentzian function, the factor which corresponds well with the lifetime broadening of the peaks, was kept the same for all the peaks and between the monolayer and multilayer spectra. Determining the Gaussian width was slightly more complicated because it is to be expected that monolayer states are broader than multilayer states due to the interaction of the molecular states with surface states of the TiO_2, as has been observed in both photoemission studies[7, 9] and DFT calculations.[95] However, the amount of broadening should be

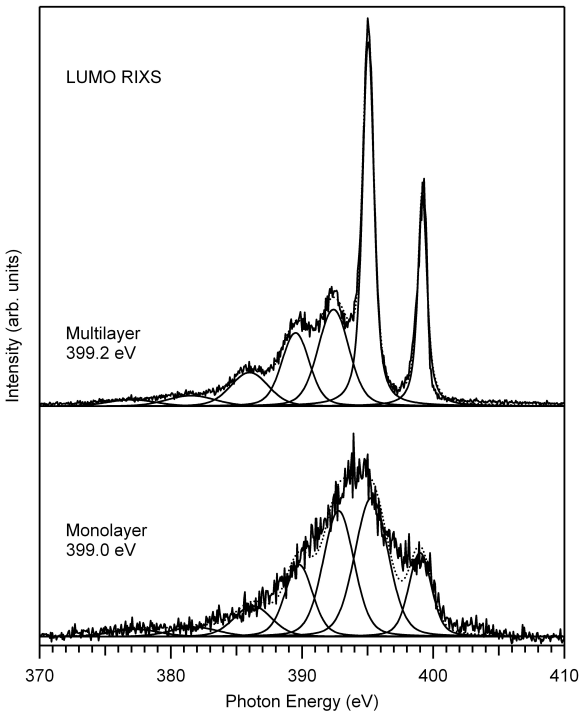

FIGURE 7.4: Resonant inelastic x-ray scattering spectra for both the multilayer (on top) and monolayer (on bottom) of bi-isonicotinic acid on TiO_2 taken for photon energies of 399.2 eV and 399 eV repectively corresponding to the LUMO resonance in each case. Peaks have been fitted to both spectra to correpond with individual orbitals. The area of the peaks were normalised to the total area of the entire spectra.

similar for each peak, so the ratios of the Gaussian widths between the peaks have been kept the same (this broadening is also assumed to have the same effect on the LUMO and LUMO+1 RIXS).

Using all these rules, we have been able to produce fitted peaks for the monolayer spectra that we can have a high confidence in. Nonetheless, we must point out that we assume that no new states have been produced due to interaction between the surface and the molecule which would affect the spectra. The main purpose of the curve fit is to obtain the intensity of the elastic peaks and, hence, the amount of participator decay as a function of the total number of photons emitted in the core-hole decay process. The ratio of the normalized elastic peaks area between the LUMO and LUMO+1 should be similar in the case of the multilayer or monolayer unless another

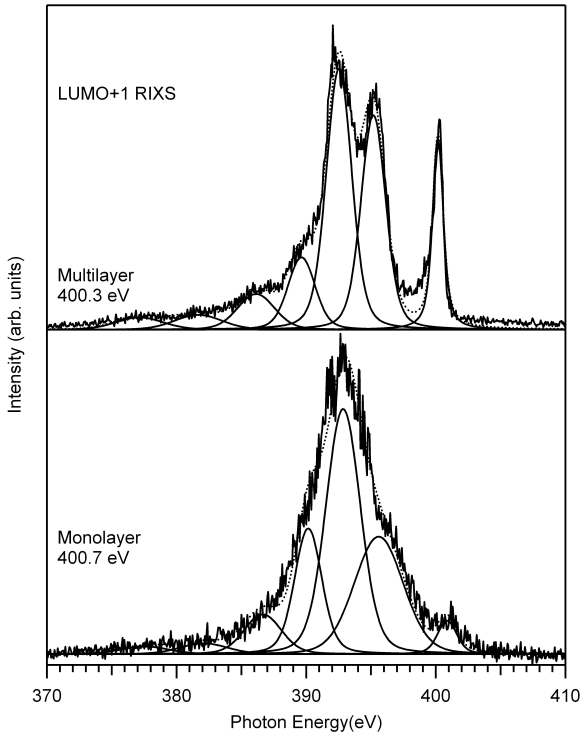

FIGURE 7.5: Resonant inelastic x-ray scattering spectra for both the multilayer (on top) and monolayer (on bottom) of bi-isonicotinic acid on TiO_2 taken for photon energies of 400.3 eV and 400.7 eV repectively corresponding to the LUMO+1 resonance in each case. Peaks have been fitted to both spectra to correpond with individual orbitals. The area of the peaks were normalised to the total area of the entire spectra.

process, such as charge transfer, as seen in figure 7.1d, occurs.

We can already observe a difference in the size of the elastic peaks. The elastic peaks in the multilayer are very clearly observed and, as can be seen, there is only a little difference between the LUMO+1 and LUMO multilayer elastic peaks. The elastic peak for the LUMO monolayer peak is observed clearly as a large shoulder on the side of the RIXS spectra. The elastic peak for the LUMO+1 monolayer is reduced severely. There is less participator decay occurring for the monolayer at the LUMO+1 resonance. From the energy alignment of valence-band photoemission, x-ray absorption and substrate density of states for this system, we already know that the LUMO state of the monolayer lies 0.6 eV below the conduction band edge of the titanium dioxide substrate in the core-excited state, so charge transfer from the

LUMO to the surface is not possible.[9] The LUMO+1, on the other hand, overlaps with the unoccupied density of states of the substrate. The situation is similar for the multilayer; however, these molecules are isolated from the surface in a thick film and, therefore, of the four states probed in this experiment, CT is only expected for the LUMO+1 state of the chemisorbed monolayer. The reduction in the elastic peak can only really be explained by a large amount of charge transfer from the LUMO+1 to the surface conduction band of the TiO_2 substrate.

The fitted peaks allow for a more quantitative analysis of the charge transfer time. In Chapter 3, we describe how we could obtain the charge transfer time if we found the relative amount of elastic decay for both the LUMO and LUMO+1 monolayer and multilayer spectra. By relating the fractional spectral intensity of the participator channel to the rates of charge transfer into the conduction band and the core-hole decay, we obtain Eq. 7.1 for the excited electron transfer time, τ_{El}, in terms of the intensities of the participator channel I_{iso} for the isolated molecule (multilayer) and for the coupled monolayer system I_{coup}.

$$\tau_{El} = \tau_{CH} \frac{I_{coup}}{I_{iso} - I_{coup}} \tag{7.1}$$

In the case of RIXS experiments, exploring charge transfer from the LUMO+1 state, I_{coup} is given by the relative intensity (from the normalized area underneath the peak) of the elastic peak in the LUMO+1 monolayer RIXS, normalized to the intensity of the elastic peak in the LUMO monolayer spectrum where CT is forbidden. Similarly, I_{iso} is derived from the intensity of the elastic peak in the LUMO+1 multilayer spectrum, normalized to the intensity of the LUMO elastic peak for the multilayer, resulting in equation 7.2.

$$\tau_{El} = \tau_{CH} \frac{A^{mono}_{LUMO+1}/A^{mono}_{LUMO}}{A^{multi}_{LUMO+1}/A^{multi}_{LUMO} - A^{mono}_{LUMO+1}/A^{mono}_{LUMO}} \tag{7.2}$$

The normalised area under the LUMO multilayer elastic peak, A^{multi}_{LUMO}, is 0.167, and the area under the LUMO+1 multilayer elastic peak, A^{multi}_{LUMO+1}, is 0.127. For the monolayer, the area under the LUMO elastic peak, A^{mono}_{LUMO}, is 0.136, and for the

LUMO+1 elastic peak, the area, A^{mono}_{LUMO+1} is 0.033. τ_{CH} is the average lifetime of an N 1s core-hole which we already know is 6 fs.[86] The equation above is similar to that derived by Brühwiler *et al.* for the core-hole clock implementation in photoemission studies.[62] Inputting the numbers into equation 7.2 gives an average charge transfer time of 2.8 fs ±1.5 fs. The high uncertainty comes from the small size of the LUMO+1 monolayer participator peak compared to the background noise. This corresponds well with charge transfer times given in photoemission studies[9] for an upper limit of 3 fs.

The fact that the same result was achieved using the new RIXS adaptation of the core-hole clock technique, as was obtained for the resonant photoemission studies, gives us a high confidence in the ability of this technique to determine the charge transfer from adsorbates to semiconductor surfaces. This allows us to be able to use RIXS to probe other adsorbates on similar semiconductor surfaces. The restrictions that apply to using the core-hole clock technique in resonant photoemission, also apply to RIXS. The main prerequisite is that the lowest unoccupied molecular orbitals need to be below the conduction band edge in the core excited state and that higher unoccupied orbitals need to be above it.

7.4 Conclusion

Through resonant inelastic x-ray scattering spectra for the monolayer and multilayer of bi-isonicotinic acid on TiO_2 taken at the LUMO and LUMO+1 resonant photon energies, we have found that there is significant charge transfer from the LUMO+1 of the bi-isonicotinic acid adsorbate to the conduction band of the TiO_2 substrate when an electron has been promoted to the LUMO+1 orbital. Using an adaptation of the core-hole technique for RIXS, we found that the charge transfer has an average time of 2.8 fs ±1.5 fs. This result lies within the limits given by previous resonant photoemission studies results. This provides us with a much higher confidence that the core-hole technique can be used accurately to determine charge transfer in RIXS. This allows us to determine the charge transfer in situations which do not allow for resonant photoemission. One such example would be in studying the charge transfer

processes in buried interfaces or in the liquid environments of real DSSCs.

Chapter 8

Summary and Conclusion

The aim of all the research in this thesis was to gain a better understanding of charge transfer between organic molecules and surfaces, especially relating to the situation observed in dye sensitized solar cells. This broad theme can be further subdivided into two main avenues of research. Firstly, there are the photoemission studies of a variety of different molecules adsorbed onto a Au(111) surface. The reason for studying this was because some solid state DSSCs used an ultrathin layer of gold to resupply electrons to the dye molecule, and we wanted to study this resupply mechanism. Secondly, we wanted to determine whether the core-hole clock technique, previously used in photoemission studies of various molecules adsorbed onto semiconductor surfaces, can be adapted for use in resonant inelastic x-ray scattering. This could be a very useful technique for studying molecules in embedded surfaces.

In Chapter 4, our resonant photoemission measurements of a C_{60} monolayer on a Au(111) surface showed three distinct constant kinetic energy features which were absent from the multilayer and clean gold spectra. This implies that these features result from the interaction between the molecule and the surface. The spacing in kinetic energy of the three features matched up with what was observed for the HOMO levels found in the C_{60} multilayer valence band spectra, suggesting that this was a core-hole decay involving those orbitals. Further investigation showed that the kinetic energy of these features was significantly higher than would be possible for a molecule with only its ground state complement of electrons. The highest kinetic energy feature tracked back to the binding energy of the HOMO for the LUMO

photon energy. This means that the final state for the feature, when an electron is excited to the LUMO, is the same as for participator decay involving the HOMO in the presence of a charge transferred electron. The evidence suggests that the charge transfer most probably occurs in the ground state rather than in the core-excited state. This spectator decay involving an electron transferred into the molecule was called *superspectator decay*, and had previously been found for bi-isonicotinic acid on Au(111) surface.[24] However, the exact nature of this feature was unclear and was believed to involve some sort of ultra-fast back donation onto the chemisorbed molecule within the core-hole lifetime. The clarity of the resonant photoemission spectra for C_{60} on Au(111), made possible by the large number of carbon atoms in a similar chemical environment, unambiguously showed the exact nature of the core-hole decay channel.

In chapter 5, we repeated the experiment for the dye molecule, N3, and isonicotinic acid on Au(111) and compared it with data obtained previously by our group for bi-isonicotinic acid on Au(111). The aim was to explore scenarios more similar to model DSSC surfaces. The RPES spectra for the isonicotinic acid was similar to that found for bi-isonicotinic acid and it also showed the superspectator decay features. This suggests that charge transfer occurs from the surface to the isonicotinic acid. Such outcome was expected due to the similarity of the molecule to bi-isonicotinic acid. Nevertheless, the RPES spectrum for the monolayer of the dye molecule, N3, did not show the distinctive superspectator decay features and means that there is a lack of charge transfer to the molecule from the surface. This was surprising, not only because the constituent ligand molecule which bound the molecule to the surface, bi-isonicotinic acid, did undergo charge transfer, but also because our measurements of the binding energies of the unoccupied and occupied states showed that it was energetically favourable. The reason for this lack of charge transfer is believed to be due to the adsorption geometry of the N3 molecule on Au(111). In order for charge transfer to occur between a molecular orbital and a surface orbital, there needs to be some spatial overlap between them. The LUMO of the dye molecule is known to lie on the π^* orbitals of the pyridine ring. The spherical geometry of the dye molecule prevents the π^* orbitals from getting close enough to the surface to have sufficient

spatial overlap and, consequently, this prevents any interaction between them. It is interesting to contrast this situation with the one for isonicotinic and bi-isonicotinic acid, which have both been shown to lie flat on the surface. Further evidence for this superspectator decay was found for picolinic and nicotinic acid, as is described in Chapter 6. They too were shown to lie flat on the surface.

As well as studying molecules adsorbed onto metal surfaces, we also studied charge transfer from adsorbed molecules into the conduction band of a semiconductor substrate. Previously, photoemission had been used to perform a core-hole clock analysis, which is described fully in Chapter 3. Theoretically, it was considered that the core-hole clock technique could be adapted for use with resonant inelastic x-ray scattering. This adaptation was done by measuring the change in the elastic peak for the monolayer, for the LUMO and LUMO+1, compared to the respective change for the multilayer. We used bi-isonicotinic acid adsorbed onto a TiO_2 substrate because we have already studied that setup using photoemission spectroscopy. Using our new adapted technique for the core-hole clock, which is described in detail in both Chapters 3 and 7, we found a charge transfer time of 2.8 ± 1.5 femtoseconds. This is the same as has been found in previous resonant photoemission studies.[9] As a result, we have confidence in using this core-hole clock adaptation for RIXS in scenarios where resonant photoemission is not possible such as in embedded surfaces or inside liquid environments, for example; as in dye sensitized solar cells.

Future research could build upon the work in this thesis. I would suggest studying C_{60} on other metal surfaces, especially Cu(111), to see whether the superspectator decay is found on other metals. Besides this, we could start using a more quantitative approach to determine the amount of charge transfer. This could be done by measuring the intensity of the superspectator decay feature relative to the intensity of other features, as this should be proportional to the amount of charge transferred. Using C_{60} would be an ideal way to test this approach out before turning to other molecules. The next step for our core-hole clock adaptation of RIXS is to study dye molecules, such as N3, adsorbed onto the TiO_2. Assuming that is successful, we would then turn to the more ambitious project of studying such systems embedded in a polymer, similar to those found in some solid state DSSCs, as is discussed in the

introduction chapter, and also inside a liquid electrolyte, modeling the conventional DSSC. Although studying organic monolayers with RIXS is not an easy task (due to the low sensitivity), this technique could be very useful, especially with some of the newer RIXS beamlines that are being introduced to many synchrotron facilities.

References

[1] T.M. Razykov, C.S. Ferekides, D. Morel, E. Stefanakos, H.S. Ullal, and H.M. Upadhyaya. Solar photovoltaic electricity: Current status and future prospects. *Solar Energy*, 85:1580, 2011.

[2] L. El Chaar, L. A. Lamont, and N. El Zein. Review of photovoltaic technologies. *Renewable and Sustainable Energy Reviews*, 15:2165, 2011.

[3] Yamaguchi, Masafumi, Nishimura, Ken-Ichi, Sasaki, Takuo, Suzuki, Hidetoshi, Arafune, Kouji, Kojima, Nobuaki, Ohsita, Yoshio, Okada, Yoshitaka, Yamamoto, Akio, Takamoto, Tatsuya, Araki, and Kenji. Novel materials for high-efficiency III/V multi-junction solar cells. *Solar Energy*, 82:173, 2008.

[4] M. Grätzel. Dye-sensitized solar cells. *Journal of Photochemistry and Photobiology C: Photochemistry Reviews*, 4:145, 2003.

[5] B. O'Regan and M. Grätzel. A low-cost, high-efficiency solar cell based on dye-sensitized colloidal TiO_2 films. *Nature*, 353:737, 1991.

[6] L. C. Mayor, J. B. Taylor, G. Magnano, A. Rienzo, C. J. Satterley, J N. OShea, and J. Schnadt. Photoemission, resonant photoemission, and x-ray absorption of a Ru(II) complex adsorbed on rutile TiO_2(110) prepared by in situ electrospray deposition. *J. Chem. Phys.*, 129:114701, 2008.

[7] J. B. Taylor, L. C. Mayor, J. C. Swarbrick, J. N. O'Shea, and J. Schnadt. Charge-transfer dynamics at model metal-organic solar cell surfaces. *Journal of Physical Chemistry*, 111:16646, 2007.

[8] L. Patthey, H. Rensmo, P. Persson, K. Westermark, L. Vayssieres, A. Stashans, Å. Petersson, P. A. Brühwiler, H. Siegbahn, S. Lunell, and N. Märtensson. Adsorption of bi-isonicotinic acid on rutile TiO_2(110). *Journal of Chemical Physics*, 110:5913, 1999.

[9] J. Schnadt, P. A. Brühwiler, L. Patthey, J. N. O'Shea, S. Södergren, M. Odelius, R. Ahuja, O. Karis, M. Bässler, P. Persson, H. Siegbahn, S. Lunell, and N. Mårtensson. Experimental evidence for sub-3-fs charge transfer from an aromatic adsorbate to a semiconductor. *Nature*, 418:620, 2002.

[10] B. Li, L. Wang, B. Kang, P. Wang, and Y. Qui. Review of recent progress in solid state dye sensitized solar cells. *Solar Energy Materials and Solar Energy*, 90:549, 2006.

[11] J-K. Lee and M. Yang. Progress in light harvesting and charge injection of dye-sensitized solar cells. *Materials Science and Engineering B*, 176:1142, 2011.

[12] K. Tennakone, G. R. R. A. Kumara, A. R. Kumarasinghe, K. G. U. Wijayantha, and P. M. Sirimanne. A dye-sensitized nano-porous solid-state photovoltaic cell. *Semiconductor Science and Technology*, 10:1689, 1995.

[13] G.R.R.A. Kumara, A. Konno, G.K.R. Senadeera, P.V.V. Jayaweera, D.B.R.A. De Silva, and K. Tennakone. Dye-sensitized solar cell with the hole collector p-CuSCN deposited from a solution in n-propyl sulphide. *Solar Energy Materials and Solar Cells*, 69:195, 2001.

[14] V. P. S Perara and K. Tennakone. Recombination processes in dye-sensitized solid-state solar cells with CuI as the hole collector. *Solar Energy Materials and Solar Cells*, 79:249, 2003.

[15] K. Tennakone, V. P. S. Perera, I. R. M. Kottegoda, and G. R. R. A. Kumara. Dye-sensitized solid state photovoltaic cell based on composite zinc oxide/tin (IV) oxide films. *Journal of Physics D: Applied Physics*, 32:374, 1999.

[16] J. Krüger, R. Plass, M. Grätzel, and H.-J. Matthieu. Improvement of the photovoltaic performance of solid-state dye-sensitized device by silver complexation of the sensitizer cis-bis(4,4-dicarboxy-2,2bipyridine)-bis(isothiocyanato) ruthenium(II). *Applied Physics Letters*, 81:367, 2002.

[17] K. Murakoshi, R. Kogure, Y. Wada, and S. Yanagida. Solid state dye-sensitized TiO_2 solar cell with polypyrrole as hole transport layer. *Chemistry Letters*, 26:471, 1997.

[18] P. Wang, S. M. Zakeeruddin, J.-E. Moser, and M. Grätzel. A new ionic liquid electrolyte enhances the conversion efficiency of dye-sensitized solar cells. *Journal of Physical Chemistry B*, 107:13280, 2003.

[19] P. Wang, S. M. Zakeeruddin, J.-E. Moser, R. Humphry-Baker, and M. Grätzel. A solvent-free, $SeCN^-/(SeCN)^{3-}$ based ionic liquid electrolyte for high-efficiency dye-sensitized nanocrystalline solar cells. *Journal of the American Chemical Society*, 126:7164, 2004.

[20] S. Muraia, S. Mikoshibaa, H. Suminoa, and S. Hayaseb. Quasi-solid dye-sensitized solar cells containing chemically cross-linked gel: How to make gels with a small amount of gelator. *Journal of Photochemistry and Photobiology A: Chemistry*, 148:33, 2002.

[21] R. Komiya, L. Han, R. Yamanaka, A. Islam, and T. Mitate. Highly efficient quasi-solid state dye-sensitized solar cell with ion conducting polymer electrolyte. *Journal of Photochemistry and Photobiology A: Chemistry*, 164:123, 2004.

[22] E. W. McFarland and J. Tang. A photovoltaic device structure based on internal electron emission. *Nature*, 421:616, 2003.

[23] M. Grätzel. Solar cells to dye for. *Nature*, 421:586, 2003.

[24] J. B. Taylor, L. C. Mayor, J. C. Swarbrick, and J. N. O'Shea. Adsorption and charge transfer dynamics of bi-isonicotinic acid on Au(111). *Journal of Chemical Physics*, 127:134707, 2007.

[25] S. Isoda. Photo-induced electron transfer processes in thin-film solarcells. *Journal of Enviromental Sciences*, 23:S18, 2011.

[26] T. Shiga and T. Motohiro. Photosensitization of nanoporous TiO_2 film with porphyrin-linked fullerene. *Thin Solid Films*, 516:1204, 2008.

[27] R. J. D. Miller, G. L. McLendon, A. J. Nozik, W. Schmickler, and F. Wilig. *Surface Electron Transfer Processes*. VCH Publishers, 1995.

[28] N. Sutin. Electron transfer reactions in solution: a historical perspective. *Advances in Chemical Physics*, 106, 1999.

[29] J. R. Hook and H. E. Hall. *Solid State Physics*. Wiley, 2001.

[30] C. B. Duke. *Tunneling in Biological Systems*. Academic Press, 1979.

[31] R. A. Marcus. Chemical and electrochemical electron transfer theory. *Annual Review of Physical Chemistry*, 15:155, 1964.

[32] R. A. Marcus. On the theory of oxidation-reduction reactions involving electron transfer. I. *Journal of Chemical Physics*, 24:966, 1956.

[33] R. A. Marcus. Electrostatic free energy and other properties of states having nonequilibrium polarization. I. *Journal of Chemical Physics*, 24:979, 1956.

[34] M. Bixon and J. Jortner. Electron transfer - from isolated molecules to biomolecules. *Advances in Chemical Physics*, 106:35, 1999.

[35] P. W. Atkins. *Physical Chemistry*. Oxford University Press, 1998.

[36] J. S. Bader and D. Chandler. Computer simulation of photochemically induced charge transfer. *Chemical Physics Letters*, 157:501, 1989.

[37] R. A. Marcus and N. Sutin. Electron transfers in chemistry and biology. *Biochim Biophys Acta*, 811:265, 1985.

[38] J. M. Lanzafame, S. Palese, D. Wang, and R. J. D. Miller. Ultrafast nonlinear optical studies of surface reaction dynamics: Mapping the electron trajectory. *Journal of Physical Chemistry*, 98:11020, 1994.

[39] A. J. Britton, A. Rienzo, K. Schulte, and J. N. O'Shea. Charge transfer between the Au(111) surface and adsorbed C_{60}: resonant photoemission and new core-hole decay channels. *Journal of Physical Chemistry*, 133:094705, 2010.

[40] M. Knudsen. Die gesetze der molekularströmung und der inneren reibungströmung der gase durch röhren. *Annalen der Physik*, 333:75, 1908.

[41] W. P. McCray. MBE deserves a place in the history books. *Nature Nanotechnology*, 2:259, 2007.

[42] A. J. Britton, J. N. O'Shea, and M. Weston. Charge transfer interactions of a Ru(II) dye complex and related ligand molecules adsorbed onto an Au (111) surface. *Journal of Physical Chemistry*, 135:164702, 2011.

[43] A. J. Britton, M. Weston, and J. N. O'Shea. Charge transfer from an aromatic adsorbate to a semiconductor TiO_2 surface probed on the femtosecond time scale with resonant inelastic x-ray scattering. *Physical Review Letters*, 109:017401, 2012.

[44] J. N. O'Shea, J. B. Taylor, J. C. Swarbrick, G. Magnano, L. C. Mayor, and K. Schulte. Electrospray deposition of carbon nanotubes in vacuum. *Nanotechnology*, 18:035707, 2007.

[45] C. J. Satterley, L. M. A. Perdigäo, A. Saywell, G. Magnamo, A. Rienzo, L. C. Mayor, V. R. Dhanak, P. H. Beton, and J. N. O'Shea. Electrospray deposition of fullerenes in ultra-high vacuum: in situ scanning tunneling microscopy and photoemission spectroscopy. *Nanotechnology*, 18:455304, 2007.

[46] A. Saywell, G. Magnano, C. J. Satterley, L. M. A. Perdig ao, N. R. Champness, P. H. Beton, and J. N. O'Shea. Electrospray deposition of C_{60} on a hydrogen-

bonded supramolecular network. *Journal of Physical Chemistry C*, 112:7706, 2008.

[47] A. Rienzo, L. C. Mayor, G. Magnano, C. J. Satterley, E. Ataman, J. Schnadt, K. Schulte, and J. N. O'Shea. X-ray absorption and photoemission spectroscopy of Zn-protoporphyrin adsorbed on rutile TiO_2(110)prepared by *in situ* electrospray deposition. *Journal of Chemical Physics*, 132:084703, 2010.

[48] A. Saywell, A. J. Britton, N. Taleb, M. del C. Giménez-López, N. R. Champness, P. H. Beton, and J. N. O'Shea. Single molecule magnets on a gold surface: in situ electrospray deposition, x-ray absorption and photoemission. *Nanotechnology*, 22:075704, 2011.

[49] M. C. OSullivan, J. K. Sprafke, D. V. Kondratuk, C. Rinfray, T. D. W. Claridge, A. Saywell, M. O. Blunt, J. N. OShea, P. H. Beton, M. Malfois, and H. L. Anderson. Vernier templating and synthesis of a 12-porphyrin nano-ring. *Nature*, 469:72, 2011.

[50] A. Saywell, J. K. Sprafke, L. J. Esdaile, A. J. Britton, A. Rienzo, H. L. Anderson, J. N. O'Shea, and P. H. Beton. Conformation and packing of porphyrin polymer chains deposited using electrospray on a gold surface. *Angewandte Chemie International Edition*, 49:9136, 2010.

[51] L. C. Mayor, A. Saywell, G. Magnano, C. J. Satterley, J N. O'Shea, and J. Schnadt. Adsorption of a Ru(II) dye complex on the Au (111) surface: Photoemission and scanning tunnelling microscopy. *Journal of Chemical Physics*, 130:164704, 2009.

[52] M. Weston, A. J. Britton, and J. N. O'Shea. Charge transfer dynamics of model charge transfer centers of a multicenter water splitting dye complex on rutile TiO_2(110). *Journal of Chemical Physics*, 134:054705, 2011.

[53] M. Weston, T. J. Reade, A. J. Britton, K. Handrup, N. R. Champness, and J. N. O'Shea. A single centre water splitting dye complex adsorbed on rutile

TiO_2(110): Photoemission, x-ray absorption, and optical spectroscopy. *Journal of Chemical Physics*, 135:114703, 2011.

[54] L. C. Mayor. *The adsorption and charge-transfer dynamics of model dye sensitized solar cells*. PhD thesis, University of Nottingham, 2009.

[55] G. Taylor. Disintegration of water droplets in an electric field. *Proceedings of the Royal Society A*, 280:383, 1964.

[56] P. Willmott. *Introduction to Synchrotron Radiation : Techniques and Applications*. Wiley, 2011.

[57] G. Zimmerer. Luminescence spectroscopy with synchrotron radiation: History, highlights, future. *Journal of Luminescence*, 119:1, 2006.

[58] M. P. Seah and W. A. Dench. Quantitative electron spectroscopy of surfaces: A standard data base for electron inelastic mean free paths in solids. *Surface and interface analysis*, 1:2, 1979.

[59] C. Westphal. The study of the local atomic structure by means of x-ray photoelectron diffraction. *Surface Science Reports*, 50:1, 2003.

[60] D. P. Woodruff and T. A. Delchar. *Modern Techniques of Surface Science*. Cambridge University Press, 2nd edition edition, 1994.

[61] J. Stöhr. *NEXAFS Spectroscopy*. Springer-Verlag, 1992.

[62] P. A. Brühwiler, O. Karis, and N. Mårtensson. Charge-transfer dynamics studied using resonant core spectroscopies. *Reviews of Modern Physics*, 74:703, 2002.

[63] J. Stöhr and D. A. Outka. Determination of molecular orientations on surfaces from the angular dependence of near-edge x-ray-absorption fine-structure spectra. *Physics Review B*, 36:7891, 1987.

[64] R. Nyholm, J. N. Andersen, U. Johansson, B. N. Jensen, and I. Lindau. Beamline I311 at max-lab: A vuv/soft x-ray undulator beamline for high resolution

electron spectroscopy. *Nuclear Instruments and Methods in Physics Research B*, 467-468:520, 2001.

[65] R. Denecke, P. Väterlein, M. Bässler, N. Wassdahl, S. Butorin, A. Nilsson, J.-E. Rubensson, J. Nordgren, N. Mårtensson, and R. Nyholm. Beamline I511 at max II, capabilities and performance. *Journal of Electron Spectroscopy and Related Phenomena*, 101:971, 1999.

[66] A. Föhlisch, P. Feulner, F. Hennies, A. Fink, D. Menzel, D. Sanchez-Portal, P.M. Echenique, and W. Wurth. Direct observation of electron dynamics in the attosecond domain. *Nature*, 436:373, 2005.

[67] J. Schnadt, J. Schiessling, and P. A. Brühwiler. Comparison of the size of excitonicnext term effects in molecular π systems as measured by core and valence spectroscopies. *Chemical Physics*, 312:39, 2005.

[68] A. Nilsson. Applications of core level spectroscopy to adsorbates. *Journal of Electron Spectroscopy and Related Phenomena*, 126:3, 2002.

[69] J.-E. Rubensson. Rixs dynamics for beginners. *Journal of Electron Spectroscopy*, 110:135, 2000.

[70] L. G. M. Pettersson, A. Nilsson, S. Myneni, Y. Luo, M. Nyberg, M. Cavalleri, L. Ojamäe, L.-Å. Näslund, H. Ogasawara, M. Odelius, and A. Pelmenschikova. *Journal of Synchrotron Radiation*, 8:136, 2001.

[71] R. C. Haddon, A. F. Hebard, M. J. Rosseinsky, and D. W. MURPHY et al. Conducting films of C_{60} and C_{70} by alkali-metal doping. *Nature*, 350(6316):320–322, 1991.

[72] A. F. Hebard, M. J. Rosseinsky, R. C. Haddon, and D. W. Murphy et al. Superconductivity at 18-K in potassium-doped C_{60}. *Nature*, 350:600–601, 1991.

[73] H. Imahori, Y. Kashiwagi, T. Hasobe, M. Kimura, T. Hanada, Y. Nishimura, I. Yamazaki, Y. Araki, O. Ito, and S. Fukuzumi. Porphyrin and fullerenenext

term-based artificial photosynthetic materials for previous term photovoltaics. *Thin Solid Films*, 451:580, 2004.

[74] E. I. Altman and R. J. Colton. The interaction of C_{60} with noble-metal surfaces. *Surf. Sci.*, 295:13–33, 1993.

[75] C.-T. Tzeng, W.-S. Lo, J.-Y. Yuh, R.-Y. Chu, and K.-D. Tsuei. Photoemission, near-edge x-ray-absorption spectroscopy, and low-energy electron-diffraction study of C_{60} on Au (111) surfaces. *Physical Review B*, 61:2263, 2000.

[76] A. J. Maxwell, P. A. Brühwiler, A. Nilsson, N. Mårtensson, and P. Rudolf. Photoemission, autoionization, and x-ray-absorption spectroscopy of ultrathin-film C_{60} on Au (110). *Phys. Rev. B*, 49:10717–10725, 1994.

[77] J. V. Barth, H. Brune, G. Ertl, and R. J. Behm. Scanning tunneling microscopy observations on the reconstructed Au (111) surface: Atomic structure, long-range superstructure, rotational domains, and surface defects. *Physical Review B*, 42:9307, 1990.

[78] X.-X. Wang, Y.-B. Xu, H.-N. Li, W.-H. Zhang, and F.-Q. Xu. Photoemission intensity oscillations in the HOMO-2 band of C_{60} film. *Journal of Electron Spectroscopy and Related Phenomena*, 165:20, 2008.

[79] J. Schnadt, J. N. O'Shea, L. Patthey, J. Krempasky, N. Mårtensson, and P. A. Bruhwiler. Alignment of valence photoemission, x-ray absorption, and substrate density of states for an adsorbate on a semiconductor surface. *Physical Review B*, 67:235420, 2003.

[80] J. M. Lanzafame, R. J. D. Miller, A. A. Muenter, and B. A. Parkinson. Ultrafast charge-transfer dynamics at tin disulfide surfaces. *J. Phys. Chem.*, 96:2820–2826, 1992.

[81] J. M. Lanzafame, S. Palese, D. Wang, R. J. D. Miller, and A. A Muenter. Ultrafast nonlinear optical studies of surface reaction dynamics: Mapping the electron trajectory. *J. Phys. Chem.*, 98:11020–11033, 1994.

[82] L. Kjeldgaard, T. Käämbre, J. Schiessling, I. Marenne, J. N. O'Shea, J. Schnadt, C. J. Glover, M. Nagasono, D. Nordlund, M. G. Garnier, L. Qian, J.-E. Rubensson, P. Rudolf, N. Mårtensson, J. Nordgren, and P. A. Brühwiler. Intramolecular vibronic dynamics in molecular solids: C_{60}. *Physics Review B*, 72:205414, 2005.

[83] S. J. Chase, W. S. Bacsa, M. G. Mitch, L. J. Pilione, and J. S. Lannin. Surface-enhanced raman scattering and photoemission of C_{60} on noble-metal surfaces. *Physics Review B*, 46:7873, 1992.

[84] S. C. Veenstra, A. Heeres, G. Hadzhoannou, G. A. Sawatazky, and H. T. Jonkman. On interface dipole layers between C_{60} and Ag or Au. *Applied Physics A*, 75:661, 2002.

[85] J. Schnadt, J. N. O'Shea, L. Patthey, J. Krempaský, N. Mårtensson, and P. A. Brühwiler. Alignment of valence photoemission, x-ray absorption, and substrate density of states for an adsorbate on a semiconductor surface. *Physical Review B*, 67:235420, 2003.

[86] B. Kempgens, A. Kivimäki, M. Neeb, H. M. Köppe, A. M. Bradshaw, and J. Feldhaus. A high-resolution N 1s photoionization study of the N_2 molecule in the near-threshold region. *Journal of Physics B-Atomic Molecular and Optical Physics*, 29:5389, 1996.

[87] G. W. Evans and E. C. Johnson. Effect of iron, vitamin B-6 and picolinic acid on zinc adsorption in rats. *Journal of Nutrition*, 111:68, 1981.

[88] A. Gille, E. T. Bodor, K. Ahmed, and S. Offermanns. Nicotinic acid: Pharmacological effects and mechanisms of action. *Annual Review of Pharmacology and Toxicology*, 48:79, 2008.

[89] E. Goulielmakis, V. S. Yakovlev, A. L. Cavalieri, M. Uiberacker, V. Pervak, A. Apolonski, R. Kienberger, U. Kleineberg, and F. Krausz. Attosecond control and measurement: Lightwave electronics. *Science*, 317:769, 2007.

[90] L. Gundlach, R. Ernstorfer, and F. Willig. Dynamics of photoinduced electron transfer from adsorbed molecules into solids. *Applied Physics A*, 88:481, 2007.

[91] D. Menzel. Ultrafast charge transfer at surfaces accessed by core electron spectroscopy. *Chemical Society Review*, 37:2212, 2008.

[92] M. Stichler, C. Keller, C. Heske, M. Staufer, U. Birkenheuer, N. Rösch, W. Wurth, and D. Menze. X-ray emission spectroscopy of NO adsorbates on Ru(001). *Surface Science*, 448:164, 2000.

[93] F. J. Himpsel. Photon-in photon-out soft x-ray spectroscopy for materials science. *Physica Status Solida B*, 248:292, 2010.

[94] Andres Hagfeldt and Michael Grätzel. Molecular photovoltaics. *Accounts of Chemical Research*, 33:269, 2000.

[95] M. Odelius, P. Perrson, and S. Lunell. Bi-isonicotinic acid on rutile (1 1 0): calculated molecular and electronic structure. *Surface Science*, 529:47, 2003.